

UC San Diego

UC San Diego Electronic Theses and Dissertations

Title

Nanoscale Microspectroscopic Analysis of Environmental Surfaces: Aerosol and Window Glass

Permalink

<https://escholarship.org/uc/item/5sr6r2dt>

Author

Or, Victor Wingtai

Publication Date

2021

Peer reviewed|Thesis/dissertation

UNIVERSITY OF CALIFORNIA SAN DIEGO

**Nanoscale Microspectroscopic Analysis of Environmental Surfaces: Aerosol
and Window Glass**

A dissertation submitted in partial satisfaction of the
requirements for the degree
Doctor of Philosophy

in

Chemistry

by

Victor Wingtai Or

Committee in charge:

Professor Vicki H. Grassian, Chair
Professor Donald Sirbuly
Professor Andrea Tao
Professor Emmanuel Theodorakis
Professor Mark Thiemens
Professor Wei Xiong

2021

Copyright
Victor Wingtai Or, 2021
All rights reserved.

The dissertation of Victor Wingtai Or is approved, and it is acceptable in quality and form for publication on microfilm and electronically:

University of California San Diego

2021

DEDICATION

This thesis is dedicated to my loving and supportive mom, dad, brother,
and all of my family and friends.

EPIGRAPH

Inspirational quote from an uninspired person

TABLE OF CONTENTS

Dissertation Approval Page	iii
Dedication	iv
Epigraph	v
Table of Contents	vi
List of Figures	x
List of Tables	xvii
Acknowledgements	xviii
Vita	xxi
Abstract of the Dissertation	xxiii
Chapter 1 Environmental Surfaces and Nanoscale Analyses	1
1.1 Roles of Aerosols and Surfaces in Environmental Chemistry	1
1.2 Sea Spray Aerosols Particles	3
1.3 Indoor Surfaces	8
1.4 Thesis Objective	11
Chapter 2 Experimental Methods	13
2.1 Sample Preparation	13
2.1.1 Substrate Preparation for Aerosol Particles	13
2.1.2 Aerosol Particle Model System Generation for Indoor and Outdoor Chemistry Studies	14
2.1.3 Field Sampling of Aerosol Particles and Indoor Surface Depositions	14
2.2 AFM	15
2.2.1 Components	15
2.2.2 Cantilever Motions and Mechanics	16
2.2.3 Standard Operating Procedures for Use of AFM and AFM- IR Spectroscopy	18
2.2.4 Image Processing	20
2.3 AFM-IR Spectroscopy	21
2.3.1 Components	21
2.3.2 Theoretical Basis of AFM-IR spectroscopy	22
2.3.3 Operation	25
2.3.4 Environmental Cell	26

Chapter 3	Application of Nanoscale Infrared Spectromicroscopy for Model System Aerosol Studies	29
	3.1 Abstract	29
	3.2 Introduction	30
	3.3 Experimental Methods	33
	3.3.1 Materials	33
	3.3.2 Atomic Force Microscopy - Photothermal Infrared Spectroscopy	34
	3.3.3 FTIR Measurements: Multi-Analysis Aerosol Reactor. . .	36
	3.3.4 Volume Equivalent Diameters for Substrate Deposited Particles and Three-Dimensional Growth Factors	36
	3.4 Results and Discussion	37
	3.4.1 Single-Component Aerosols	37
	3.4.2 Two-Component Aerosols: Mixed Inorganic Salts and Organic Compounds	41
	3.4.3 Hygroscopic Studies: Growth Factors and Spectroscopic Signatures for Water Uptake	45
	3.4.4 Sample Interactions with an IR Active Substrate	48
	3.4.5 Tapping and Resonance Enhanced AFM-PTIR	49
	3.5 Conclusions	52
	3.6 Acknowledgements	53
	3.7 Supporting Information	54
Chapter 4	Influence of Size, Biological Activity, and Heterogeneous Aging on Morphology and Composition of Marine Sea Spray Aerosols	55
	4.1 Abstract	55
	4.2 Introduction	56
	4.3 Methods	58
	4.3.1 Sea Spray Aerosol Generation and MOUDI Sampling . .	58
	4.3.2 Model System Preparation	59
	4.3.3 AFM	60
	4.3.4 AFM-IR Spectroscopy	60
	4.4 Results and Discussion	61
	4.4.1 Nascent Sea Spray Aerosols	61
	4.4.2 Influence of Aging	68
	4.5 Conclusion	72
	4.6 Acknowledgements	73
	4.7 Supporting Information	74
Chapter 5	Microspectroscopic imaging and physicochemical characterization of long term indoor depositions on window glass surfaces	77
	5.1 Abstract	77
	5.2 Introduction	78

5.3	Materials and Methods	79
5.4	Results and Discussion	80
	5.4.1 Glass Surface Morphology	80
	5.4.2 Glass Surface Composition	84
5.5	Painted Surfaces	87
5.6	Painted Surfaces	88
5.7	Painted Surfaces	89
5.8	Conclusion	90
5.9	Acknowledgements	91
5.10	Supporting Information	92
	5.10.1 Glass and Paint preparation	92
	5.10.2 Materials for Reference PTIR Spectra	93
	5.10.3 Analysis of Glass	94
Chapter 6	Short Term Glass Surface Evolution: Cooking and Cleaning Emissions	98
6.1	Abstract	98
6.2	Introduction	99
6.3	Methods	102
	6.3.1 HOMEChem	102
	6.3.2 Online SMPS particle measurements	102
	6.3.3 Window glass sampling	103
	6.3.4 AFM-IR method	104
	6.3.5 ATR-FTIR method	105
	6.3.6 Teflon chamber and laboratory sample preparation	105
	6.3.7 Particle and surface characterization	106
	6.3.8 Modeling methods and parameters	108
6.4	Results and discussion	109
	6.4.1 AFM surface measurements	109
	6.4.2 Particle viscosity	114
	6.4.3 Spectroscopic characterization of deposited particles	115
	6.4.4 Impact of deposition on surface properties	119
	6.4.5 Cleaning events: Influences on surfaces	121
6.5	Conclusion	123
6.6	Acknowledgements	124
6.7	Supporting Information	125
Chapter 7	Water uptake on glass surfaces exposure to indoor cooking activities: Comparison to model systems	129
7.1	Abstract	129
7.2	Introduction	130
7.3	Methods	133
	7.3.1 Model Systems	133
	7.3.2 Field Samples	134

7.3.3	GC-MS Analyses	134
7.3.4	AFM and AFM-IR Analyses	135
7.3.5	Surface and Particle Properties	136
7.4	Results	137
7.4.1	Hygroscopicity of Kitchen and Cooking Particles Deposited on Glass	137
7.4.2	Spectral Comparisons with Laboratory Generated Model Systems	139
7.4.3	Hygroscopicity of Model Systems	141
7.4.4	Comparison of Hygroscopic Growth on Glass Surfaces: Kitchen Exposed Samples and Model Systems	143
7.4.5	Hygroscopic Behavior of Indoor Organic Films	146
7.4.6	Implications for Water Content of Indoor Surfaces	147
7.5	Acknowledgements	149
7.6	Supporting Information	150
Chapter 8	Conclusions and Future Perspectives	153
Bibliography	157

LIST OF FIGURES

Figure 1.1:	Cartoon representation of two atmospherically relevant surfaces - sea spray aerosol (left) and window glass (right), and their interactions with environmental conditions such as light, humidity, and gaseous compounds	2
Figure 1.2:	Schematic showing bubble bursting mechanisms for film and jet drops at the ocean surface. Figure adapted from Wang <i>et al.</i> 2015[1]	4
Figure 1.3:	Cartoon representation of various mixing states of aerosol particles, externally mixed (top), internally mixed (middle), and morphologically diverse particles (bottom).	6
Figure 1.4:	Diagram showing surface processes of interest to indoor surfaces, including transport of material onto the surface and transformative processes.	8
Figure 1.5:	Examples of various sources of emissions indoors	10
Figure 2.1:	Diagram showing the main components of an atomic force microscope with an optical lever detection system to investigate substrate deposited particles from indoor and outdoor samples as well as model systems	16
Figure 2.2:	A) force-distance plot demonstrating the tip-sample force experienced by the probe across a range of tip-sample separations, ranging from attractive to repulsive regimes, with labeled regions of operation for contact and tapping AFM. B) Examples of tip motion as the probe	18
Figure 2.3:	Example plot demonstrating phase and amplitude differences between the applied piezo signal (red) and the cantilever response (cyan), with a change in amplitude ($A_1 \rightarrow A_2$) and phase(ϕ)	20
Figure 2.4:	A) Raw output height image from AFM B) Height image after plane subtraction and masked polynomial fits C) AFM image with masks identifying particles using a lower limit height threshold D) Histogram plot of masked data converted into volume equivalent diameters	21
Figure 2.5:	Image (left) and diagram (right) showing the main components of an atomic force microscopy-infrared spectrometer	21
Figure 2.6:	Main steps driving the photothermal induced resonance effect that enables cantilever motion and subsequent detection of infrared absorbance in the sample	23
Figure 2.7:	Cantilever response in ring-down decay from an OPO (left) and sustained resonance (right) from a QCL with pulse repetition rate matching cantilever oscillations	24
Figure 2.8:	A) AFM height image of a particle on an Si wafer substrate B) Chemical map taken at 1170 cm^{-1} , C) IR Spectra taken at corresponding labeled regions of the particle	25
Figure 2.9:	A) AFM height image of an organic particle on an Si wafer substrate B) Representative schematic of the hyperspectral data structure C) Integrated hyperspectral maps from $800 - 900\text{ cm}^{-1}$ and $1600 - 1700\text{ cm}^{-1}$ in upper and lower panels respectively	26

Figure 2.10:	Images of the environmental cell A) in the AFM hood B) connected while detached from the AFM head, with a schematic of the primary components of the environmental cell attachment for the AFM-IR from C) overhead and D) side-on views	26
Figure 2.11:	A) AFM height image of a calibration grating with $1.2 \times 1.2 \text{ cm}^2$ rectangular gratings imaged in the environmental cell B) optical images of NaCl at 5 (upper), 73 (middle), and 75% (lower) RH, particle growth is observed increasing the chamber to RH = DRH _{NaCl} 75% C) AFM	27
Figure 3.1:	a) 3D height image of an ammonium sulfate particle on ZnS substrate with a volume equivalent diameter of 50 nm b) Comparison of the spectra obtained by FTIR (black) to PTIR for particles with volume equivalent diameters of varying sizes and the ZnS substrate. The peak	37
Figure 3.2:	a) 3D height image of a cluster of NaCl/glucose (1:1 mass ratio) particles on ZnS substrate, with a volume equivalent diameter of 480 nm b) Phase image c) PTIR spectra taken at NaCl-rich (red) and glucose-rich (blue) regions with the corresponding locations marked in panel a).	40
Figure 3.3:	a) 3D Height image of a NaCl/PA (1:1 mass ratio) particle with a volume equivalent diameter of 510 nm b) Chemical map of the glucose rich regions of the particle taken at 1090 cm^{-1}	41
Figure 3.4:	a) 3D height image of a NaCl/PA (1:1 mass ratio) particle with a volume equivalent diameter of 280 nm on ZnS substrate with markers identifying PTIR spectra locations b) Phase image c) PTIR spectra obtained for PA rich (blue), NaCl rich (red) and ZnS (black)	43
Figure 3.5:	a) PTIR spectra obtained on a AS/PA particle for PA rich (blue) AS rich (red) and ZnS (black) regions at the corresponding locations marked in panel d. b) Chemical image of the particle at 1136 cm^{-1} c) Chemical image of the particle at 1698 cm^{-1} d) RGB overlay	44
Figure 3.6:	a) 3D height image of a NaCl particle with a volume equivalent diameter of $1.3 \mu\text{m}$ at 2% RH and b) the same particle now with the diameter of $6.6 \mu\text{m}$ at 90% RH c) Contact resonance frequency (red) and growth factor (green) for the $1.3 \mu\text{m}$ NaCl particle as a function of	46
Figure 3.7:	a) 3D height image a dry NaCl particle with a volume equivalent diameter of 140 nm on hydrophobic Si wafer substrate at 5%RH. b) The deliquesced particle with diameter of 390 nm at 85% RH c) PTIR spectra obtained on the particle marked in panel a) and b)	47
Figure 3.8:	a) PTIR spectra obtained on a NaNO ₃ particle (red) and silicon substrate (black), b) PTIR spectra taken for NaNO ₃ particles of varying height from 500 to 50 nm	49
Figure 3.9:	AFM height images of 1:1 mixed NaCl:Glucose particles collected in a) tapping mode with a QCL source and b) contact mode with an OPO source with corresponding maps collected at 1090 cm^{-1} are shown in panels c) and d) respectively. Distinct artifacts from the probe	50

Figure 3.10:	PTIR spectra collected from ammonium sulfate (AS) particles using a) standard contact AFM-PTIR with an OPO laser source and b) resonance enhanced AFM-PTIR with a QCL laser source at varying laser powers. Spectral artifacts are observed with the QCL laser at 5.38 mW.	51
Figure S3.1:	PTIR spectra taken on a sucrose particle with increasing laser power from 0.06 to 0.16 mW. Particle damage is spectrally apparent at 0.16 mW, as seen by the growth of irregular shaped peaks between 980 to 1100 cm^{-1} .	54
Figure 4.1:	Selected illustrative AFM 3D-height images of five main morphological categories (prism-like, core-shell, rounded, rod, and aggregate) identified for nascent SSA. Images provided from Chathuri Kaluarachchi from Professor Alexei Tivanski's group.	61
Figure 4.2:	Stacked bar plots of morphology distribution for nascent SSA produced during different dates of the bloom: pre-(left), peak-(middle) and post-bloom(right). Particles are separated into size bins according to their volume equivalent diameter. Data is provided from Chathuri.	62
Figure 4.3:	PTIR spectra taken for (A) prism and (B) rod SSA measured using AFM-IR. Spectra are divided into at three selected volume-equivalent diameter ranges of 0.1 - 0.18, 0.18 - 0.32 and 0.32 - 0.60 μm . Due to lower abundance and IR activity for these morphologies, no	64
Figure 4.4:	PTIR spectra and representative AFM height images for core-shell and rounded SSA measured using AFM-IR for (A), (C) pre-bloom and (B), (D) peak-bloom days. SSA spectra are divided into three selected volume-equivalent diameter ranges of 0.1 - 0.18 μm , 0.18 - 0.32 μm .	65
Figure 4.5:	A) PTIR spectra for rounded SSA particles, each with 180 nm equivalent diameter, and their average spectrum (black). AFM height images, PTIR spectra, and chemical maps taken at 1450 and 1640 cm^{-1} for rounded SSA that showed (B) two different spectrally homogeneous	67
Figure 4.6:	Stacked bar plots of morphology distribution for heterogeneously aged SSA produced during the peak-bloom. Particles are separated into size bins according to their volume equivalent diameter. Data is provided from Chathuri Kaluarachchi from Professor Alexei Tivanski's group.	68
Figure 4.7:	PTIR spectra and representative 3D AFM height images for core-shell heterogeneously aged SSA measured using AFM-IR for peak-bloom days. SSA spectra are divided into three selected volume-equivalent diameter ranges of 0.1 - 0.18 μm , 0.18 - 0.32 μm and 0.32 - 0.60 μm .	69
Figure 4.8:	A) 3D AFM height image of a core-shell particle with a rod core B) zoomed in region of the rod and shell C) PTIR spectra of the rod and shell in black and cyan respectively D) hyperspectral maps of 100 cm^{-1} windows for the zoomed-in region shown in panel B.	70

Figure 4.9:	PTIR spectra taken for core-shell (left) and rounded (right) hSSA smaller than $0.1 \mu\text{m}$ measured using AFM-IR. Solid lines show the average spectra for a given class, with shaded lines representing the 95% confidence interval.	71
Figure S4.1:	Schematic showing sampling lines for preparing substrate deposited SSA from the waveflume. Particles are impacted onto hydrophobic Si wafer substrates in the MOUDI. RH and temperature are measured at right before the MOUDI inlet. For the heterogeneously aged SSA line	74
Figure S4.2:	AFM-PTIR spectra for substrate deposited reference compounds . . .	75
Figure 5.1:	(A) AFM amplitude images of the glass surfaces placed in different indoor environments with scale bars set to $10 \mu\text{m}$. Box-and-whisker plots (close-up) of AFM-measured changes in (B) surface area and (C) R_q roughness following exposure in each location for 6 months using .	81
Figure 5.2:	(A) Organic film (thickness $> 10 \text{ nm}$) coverage on glass surfaces after exposure in each local environment for 6 months taken from the 10 AFM images ($50 \mu\text{m} \times 50 \mu\text{m}$). (B) AFM amplitude image of the organic film coating on kitchen glass after exposure for 6 months. (C) Height .	82
Figure 5.3:	Box-and-whisker plot of the number of particles (thickness $> 30 \text{ nm}$) deposited per square micrometer on glass surfaces from 10 AFM images ($50 \mu\text{m} \times 50 \mu\text{m}$) for each indoor location. Lines show 20 and 80th percentiles. Particles are categorized by volume equivalent diameter . .	83
Figure 5.4:	A) Three-dimensional (3D) AFM height image (left) and PTIR spectrum (right) for a deposited particle on the copier glass. The inset shows a comparison with carbon black (black) and CaCO_3 (gray) PTIR spectra. (B) 3D AFM height image (left) and PTIR spectrum (right) . . .	85
Figure 5.5:	ICP-MS analysis of an $1.27 \text{ cm} \times 1.27 \text{ cm}$ piece of window glass exposed to various indoor locations showing the nine most abundant elements found. Selected elements for detection include chromium, nickel, iron, aluminum, phosphorus, zinc, magnesium, potassium, calcium,	86
Figure 5.6:	Cartoon depiction of the two different types of painted materials: painted paper-on-gypsum wallboard (upper) and painted glass (lower)	87
Figure 5.7:	AFM height images and profiles for lab (left) and 3-month kitchen exposed (middle) surfaces, with PTIR spectra and difference spectra (right) for: A) LVOC-WB, B) LVOC-G, and C) ZVOC-G	88
Figure 5.8:	A) Root mean squared roughness (R_q) for painted wallboard and painted glass samples B) PTIR difference spectra from the painted surfaces and a reference PTIR spectra from a film on kitchen glass.	90
Figure S5.1:	Full box and whisker plots showing outlier measurements of A) change in surface area and B) Change in root mean squared roughness. Zoomed in view for the most common values are shown in Figure 5.1 of the main text. Lines show the 20 and 80th percentiles respectively.	96

Figure S5.2:	A) AFM amplitude images of particles on garage versus kitchen exposed glass, with lines indicating regions where B) height profiles are taken. Also provided are some values for root mean square roughness, change in surface area and kurtosis. For the height versus position plot,	96
Figure S5.3:	A) PTIR Spectra taken on the control glass sample. PTIR spectra taken on particles from the B) office and C) garage exposed glass respectively, showing organic content. Deposition from each indoor location show differing spectral features, suggesting that the location of the	97
Figure S5.4:	Less abundant metals found from ICP-MS analysis of a $1.27 \times 1.27 \text{ cm}^2$ piece of window glass exposed to various indoor locations. Elements detected below 0.1 ppb ($0.9 \mu\text{g}/\text{m}^2$) are not shown, and include Be, Ga, As, Se, Rb, Ag, Cs, La, Ce, Pr, Nd, Sm, Eu, Gd, Dy, Er, Tm, Yb .	97
Figure 6.1:	3D AFM height images of the glass surfaces exposed to different activities with scale bars set to $5 \mu\text{m}$. Note height scales increase from 70 to 260 nm across the images of the different activities.	109
Figure 6.2:	Surface deposition densities as a function of cumulative airborne PM number concentrations for (A) thanksgiving (blue) and (B) stir fry (red) events for four particle size bins: 10–50 nm, 50–100 nm, 100–300 nm, and 300–500 nm diameters (D_p and $D_{equiv,V}$ for airborne and surface .	110
Figure 6.3:	(A) Cumulative airborne size distributions from stir fry (red) and thanksgiving (blue) events. (B) Surface deposited number and cumulative volume size distributions from stir fry and thanksgiving events, with a zoom in of the larger submicron sized particles in panel (C).	110
Figure 6.4:	Comparison between the size dependent deposition (square markers) measured by AFM and predicted by the Lai–Nazaroff model with surface friction velocity of 1 (dashed line) and 3 (solid line) cm s^{-1} for the (A) thanksgiving and (B) stir fry events. Insets show a zoom in	112
Figure 6.5:	Box plots of particle aspect ratio as a function spherical equivalent diameter for all deposited particles taken from the AFM images ($30 \times 30 \mu\text{m}^2$) per event (thanksgiving – blue and stir fry – red). Boxes show the 25th and 75th percentiles, and lines show 10 and 90th percentile .	114
Figure 6.6:	Comparison of PTIR spectra taken from a film coating on kitchen glass from 1 month old kitchen glass outside of the HOMEChem campaign (blue), ATR-FTIR spectrum of acetonitrile-extracted material from 3 week exposed glass during HOMEChem (black), and PTIR spectra . .	116
Figure 6.7:	PTIR spectra and the corresponding AFM images (with color marked locations) of deposited particles from (A) thanksgiving, and (B) stir fry events. Spectral features of these particles show deprotonated organics, as indicated by the $\nu_{as}(\text{COO}^-)$ and $\nu_s(\text{COO}^-)$ modes around 1580 . . .	117

Figure 6.8:	Spectral comparison between PTIR spectra taken on depositions from the stir fry event and laboratory mimetics generated in a Teflon chamber: oleic acid particles in purple and oleic acid particles oxidized with ozone in green.	118
Figure 6.9:	3D AFM height images (upper) of the glass surfaces exposed to different activities with scale bars set to 5 μm . Note height scales increase from 90 to 140 nm across the images of the different activities. Corresponding box plots of particle aspect ratio as a function spherical	122
Figure S6.1:	Surface deposited number distributions from laboratory blank (left) and unoccupied background (right) event, with insets showing the larger submicron sized particles.	125
Figure S6.2:	Cumulative airborne size distributions from the unoccupied background event measured by the SMPS. The start of the sampling overlapped with the decay phase of an oven run which resulted in an elevated concentration of UFP.	125
Figure S6.3:	3D AFM height images of the laboratory blank and unoccupied background glass slides in left and right panels respectively. The upper image is a typical image of the corresponding sample while the lower shows the images where a large supermicron particle remained deposited.	126
Figure S6.4:	AFM-IR spectra and the corresponding AFM images (with color marked locations) of deposited particles from the stir fry event. In each panel shown, the upper image is the AFM image, with corresponding color spectra and the same AFM image with corresponding color markers . .	127
Figure S6.5:	AFM-IR spectra and the corresponding AFM images (with color marked locations) of deposited particles from the Thanksgiving event. In each panel shown, the upper image is the AFM image, with corresponding color spectra and the same AFM image with corresponding color . . .	127
Figure 7.1:	AFM height images of organic films and organic particles on window glass after 3 months exposure in a residential kitchen (left) and a single day of simulated stir fry cooking (right). Images were collected at dry (5% RH, upper) and humid (80% RH, middle) conditions, and difference	137
Figure 7.2:	AFM images of two particles from the kitchen glass in panel A) at dry and humid conditions, with difference images masked to highlight regions where water was prevalent. (i) and regions that did not grow (ii). PTIR spectra collected at 10% RH taken in the corresponding . .	138
Figure 7.3:	PTIR spectra of the particles coating A) kitchen and stir fry glass surfaces and various model systems for comparison: B) nonanoic acid (NA) and sodium nonanoate (NaNA) C) oleic acid (OA) and sodium oleate (NaOA) and D) oleic acid oxidized under dry and humid conditions . .	139

Figure 7.4:	AFM height images of model system particles on window glass from left to right: sodium nonanoate (NaNA), sodium oleate (NaOA), oleic acid (OA), oleic acid oxidized under dry conditions (OA + O ₃ dry), and oleic acid oxidized under humid conditions (OA + O ₃ wet). Images were . . .	141
Figure 7.5:	A) 3D AFM height images of sodium oleate particles on kitchen glass before, during, and after exposure to elevated RH levels, with corresponding height profiles at the indicated lines in panel B). Slight changes in morphology are present after 15 minutes of exposure, followed by . . .	142
Figure 7.6:	Scatter box plots of the hygroscopic growth factors (upper) and corresponding κ values (lower) for single particles from AFM measurements. Scatter points are roughly scaled according to particle diameters and box plot lines are set to the 5th and 95th percentiles. The total number	144
Figure 7.7:	Relative abundance histograms of the aspect ratios (AR) for the particles deposited on each of the coated window glass samples. Smaller aspect ratios (closer to zero) correspond with a higher degree of spreading and flatter particles.	146
Figure 7.8:	AFM height images of the A) middle of a film and B) edge of a film at dry (upper) and humid (middle) conditions respectively, with height profiles (lower) collected along the marked lines. The middle of the film (Area 1) demonstrates more uniform water uptake throughout	147
Figure S7.1:	AFM height images of a thin film region of the kitchen window glass under dry and humid conditions	150
Figure S7.2:	3D AFM height images at 80% (left) and 6% (right) RH of oleic acid particles reacted with ozone under dry conditions. Three representative particles with liquid bridges are outlined in red, with the substrate and other particles set at a higher transparency for visualization. Changes	150
Figure S7.3:	Size distributions (shaded bars) of deposited particles ($D_{eq,V} \leq 1\mu m$) for each of the glass surfaces with corresponding cumulative mean (filled) and total (dashed) contributions to changes in volume ($V_w^* = V_{80\%RH} - V_{5\%RH}$) at elevated RH. B) Zoomed in plot focusing on particles under 500 nm.	152

LIST OF TABLES

Table 3.1:	Aerosol particle properties that can be measured using AFM compared to AFM-PTIR spectroscopy	31
Table 3.2:	PTIR and FTIR of Ammonium Sulfate particles and peak intensity ratios between $\nu_4(\text{NH}_4^+)$ and $\nu_3(\text{SO}_4^{2-})$	38
Table 3.3:	Peak assignments for glucose vibrational modes observed in AFM-PTIR spectroscopy	41
Table S4.1:	Numerical values for abundances and counts of nascent SSA particles produced throughout the bloom.	75
Table S4.2:	Numerical values for abundances and counts of heterogeneously aged SSA particles produced at the peak of the bloom	76
Table S5.1:	Summary of mean field conditions. Data presented as mean (standard deviation). a Connected to a 106 m^3 kitchen and living room. b Connected to a 57.6 m^3 living room	93
Table S5.2:	Calculated limit of detection (LOD) and limit of quantification (LOQ) values for elements plotted from ICP-MS analysis of glass samples. A LOD or LOQ value of 0.0 indicates a corresponding limit of less than 10 pptv (less than 0.09 $\mu\text{g}/m^2$).	95
Table 6.1:	Surface properties of window glass exposed to various indoor events throughout HOMEChem measured by AFM, with standard deviations shown in parentheses	120
Table S6.1:	Sampling Times (CDT) and Dates for each exposure period.	126
Table S6.2:	A comparison of the surface properties of the laboratory blank and unoccupied background with the image containing the supermicron particle shown in Figure S6.3 excluded from analyses. The uncorrected surface properties from Table 6.1 are included in the lower half of the table . . .	128
Table 7.1:	Numerical values for the AFM measured hygroscopic growth factors and κ values in roughly 500 nm size bins, with values listed as average (standard deviation). Size bins with no particles detected are indicated with a dash (-).	145
Table S7.1:	Most abundant compounds (25) as detected by GC-MS from material extracted from window glass exposed to the kitchen for 3 months. Compounds are listed in order of relative abundance, with retention times (RT) included.	151

ACKNOWLEDGEMENTS

I would like to thank my academic advisor, Professor Vicki Grassian, for giving me the opportunity to work in her research group. She has provided invaluable guidance, assistance, and opportunities to learn and grow, and none of the research presented in this dissertation would be possible without her. She has always pushed me to grow, while still remaining confident in myself, and I have learned so much through her insights and expertise.

I would also like to thank all of my committee members, Prof. Mark Thiemens, Prof. Wei Xiong, Prof. Emamnuhal Theodorakis, and Prof. Andrea Tao for the helpful comments, suggestions, and questions they provided during my PhD career. I would also like to thank Prof. Donald Sirbully for his flexibility and willingness to serve as a committee member late in my career.

I would like to thank the NSF Center for Aerosol Impacts on the Chemistry of the Environment (CAICE) and the Alfred P. Sloan Foundation's indoor air program for funding my research and providing me with the opportunity to collaborate with many different groups and researchers. The work presented in this dissertation could not be accomplished without the efforts of collaborators in both of these organizations. I want to thank Chathuri Kaluarachchi and Hansol Lee from Prof. Aexei Tivanski's group for their assistance in sampling and helpful discussions throughout my work in CAICE, Michael Wade from Prof. Richard Corsi's group for preparing and collecting indoor samples, which was vital for much of the work presented in this publication. Thank you to Prof. Marina Vance and Prof. Delphine Farmer for their successful execution of the HOMEChem campaign, from which I want also want to thank my direct collaborators who provided data or results - Dr. Sameer Patel from Prof. Vance's group, Hannah Przelomski and Prof. Rachel O'Brien, and Prof. Donghyun Rim.

I also want to thank everyone from the Grassian research group for all of the times

we had in my years as a graduate student. I have made many wonderful memories with the group and friendships that I will forever cherish. Among all the Grassian group members, I especially would like to thank Dr. Armando Estillore and Sarah Schwab. Dr. Armando Estillore was my first mentor and friend when I joined the Grassian group, and is still a great mentor for me to this day. He has provided invaluable mentorship not only for my research career, but also has helped me with guidance and emotional support in my personal life. I would not have been able to get through a PhD career without his presence. Sarah was the first undergraduate I mentored, and has been working with me for the past four years. She is an amazing and talented person, and I have grown so much from our interactions and time together. I am glad to have been blessed with the friendship and chance to work with these two amazingly gifted and kindhearted individuals.

I would also like to thank Jon Trueblood, Izaac Sit, and Mike Alves for their maturity, professional advice, and all of our game nights; Deborah Kim and Stephanie Mora-Garcia for their similar shared appreciation of Ch*p*tle. Thank you also to Man Luo and Mona Shrestha for their all of their advice and discussions, especially when experiments ran late in the day.

Most importantly, I would like to thank my family, especially my parents, Peter Or and Cat Tse, and my younger brother, Andy Or, are always my biggest supporters of my life. I am forever grateful for them, and nothing I accomplish would be possible without them in my life.

Chapter 3, in part, is a reprint of the material published by The Royal Society of Chemistry in: **Victor W Or**, Armando D Estillore, Alexei V Tivanski, Vicki H Grassian. Lab on a Tip: Atomic Force Microscopy - Photothermal Infrared Spectroscopy of Atmospherically Relevant Organic/Inorganic Aerosol Particles in the Nanometer to Micrometer Size Range. *Analyst*, 143(12), 2018. The dissertation author was the co-first author of this paper.

Chapter 4 in part is currently prepared for submission for publication of the material. Chathuri Kaluarachchi, **Victor W. Or**, Vicki H. Grassian, Alexei V. Tivanski. The dissertation author was one of the primary investigators and author of this material

Chapter 5, in full, is a reprint of the material published by American Chemical Society in: **Victor W Or**, Michael R Alves, Michael Wade, Sarah Schwab, Richard L Corsi, Vicki H Grassian Crystal Clear? Microspectroscopic Imaging and Physicochemical Characterization of Indoor Depositions on Window Glass. *Environmental Science & Technology Letters*, 5(8), 2018. The dissertation author was the co-first author of this paper.

Chapter 6, in full, is a reprint of the material published by The Royal Society of Chemistry in: **Victor W Or**, Michael Wade, Sameer Patel, Michael R Alves, Deborah Kim, Sarah Schwab, Hannah Przelomski, Rachel O'Brien, Donghyun Rim, Richard L Corsi, Marina E Vance, Delphine K Farmer, Vicki H Grassian Glass surface evolution following gas adsorption and particle deposition from indoor cooking events as probed by microspectroscopic analysis, *Environmental Science: Processes & Impacts*, 22(8), 2020. The dissertation author was the co-first author of this paper.

Chapter 7 in part is currently prepared for submission for publication of the material. **Victor W. Or**, Michael R. Alves; Michael Wade, Sarah Schwab, Richard L. Corsi, Vicki H. Grassian. The dissertation author is the primary investigator and author of this material

VITA

2016	B. S. in Pharmaceutical Chemistry, University of California San Diego
2018	M. S. in Chemistry, University of California San Diego
2021	Ph. D. in Chemistry, University of California San Diego

PUBLICATIONS

Dissertation Related

Victor W Or, Michael Wade, Sameer Patel, Michael R Alves, Deborah Kim, Sarah Schwab, Hannah Przelomski, Rachel O'Brien, Donghyun Rim, Richard L Corsi, Marina E Vance, Delphine K Farmer, Vicki H Grassian Glass surface evolution following gas adsorption and particle deposition from indoor cooking events as probed by microspectroscopic analysis, *Environmental Science: Processes & Impacts*, 22(8), 2020.

Victor W Or, Michael R Alves, Michael Wade, Sarah Schwab, Richard L Corsi, Vicki H Grassian Crystal Clear? Microspectroscopic Imaging and Physicochemical Characterization of Indoor Depositions on Window Glass. *Environmental Science & Technology Letters*, 5(8), 2018.

Victor W Or, Armando D Estilloro, Alexei V Tivanski, Vicki H Grassian. Lab on a Tip: Atomic Force Microscopy - Photothermal Infrared Spectroscopy of Atmospherically Relevant Organic/Inorganic Aerosol Particles in the Nanometer to Micrometer Size Range. *Analyst*, 143(12), 2018.

Other Publications

Kyle J Angle, Daniel R Crocker, Rebecca MC Simpson, Kathryn J Mayer, Lauren A Garofalo, Alexia N Moore, Stephanie L Mora Garcia, **Victor W Or**, Sudarshan Srinivasan, Mahum Farhan, Jon S Sauer, Christopher Lee, Matson A Pothier, Delphine K Farmer, Todd R Martz, Timothy H Bertram, Christopher D Cappa, Kimberly A Prather, Vicki H Grassian, Acidity across the interface from the ocean surface to sea spray aerosol. *Proceedings of the National Academy of Sciences*, 118(20), 2020.

Rachel E O'Brien, Ying Li, Kristian J Kiland, Erin F Katz, **Victor W Or**, Emily Legaard, Emma Q Walkout, Corey Thrasher, Vicki H Grassian, Peter F DeCarlo, Allan K Bertram, Manabu Shiraiwa Emerging investigator series: chemical and physical properties of organic mixtures on indoor surfaces during HOMEChem. *Environmental Science: Processes and Impacts* 2021

Yangdongling Liu, Ariana Gray Be, **Victor W Or**, Michael R Alves, Vicki H Grassian, Franz M Geiger Challenges and opportunities in molecular-level indoor surface chemistry and physics. *Cell Reports Physical Science*, 1(11), 2020

Hansol D Lee, Samantha Wigley, Christopher Lee, **Victor W Or**, Elias S Hasenecz, Elizabeth A Stone, Vicki H Grassian, Kimberly A Prather, Alexei V Tivanski, Physicochemical Mixing State of Sea Spray Aerosols: Morphologies Exhibit Size Dependence. *ACS Earth and Space Chemistry*, 4(9), 2020

Haibin Wu, **Victor W Or**, Sabrina Gonzalez-Calzada, Vicki H Grassian, CuS nanoparticles in humid environments: adsorbed water enhances the transformation of CuS to CuSO₄. *Nanoscale*, 12(37), 2020

Delphine K Farmer, Marina E Vance, Jon PD Abbatt, Andrew Abeleira, Michael R Alves, C Arata, E Boedicker, S Bourne, F Cardoso-Saldaña, R Corsi, PF DeCarlo, AH Goldstein, VH Grassian, L Hildebrandt Ruiz, JL Jimenez, TF Kahan, EF Katz, JM Mattila, WW Nazaroff, A Novoselac, RE O'Brien, **VW Or**, S Patel, S Sankhyan, Philip S Stevens, Y Tian, M Wade, C Wang, S Zhou, Y Zhou "Overview of the House Observations of Microbial and Environmental Chemistry (HOMEChem) study." *Environmental Science: Processes & Impacts*, 21(8), 2019.

Jonathan V Trueblood, Xiaofei Wang, **Victor W Or**, Michael R Alves, Mitchell V Santander, Kimberly A Prather, Vicki H Grassian. Aging of Sea Spray Aerosols and Formation of Secondary Marine Aerosol Through OH Oxidation Reactions. *ACS Earth and Space Chemistry*, 3(10), 2019

Deokhyeon Kwon, **Victor W Or**, Matthew J Sovers, Mingjin Tang, Paul D Kleiber, Vicki H Grassian, Mark A Young. Optical Property Measurements and Single Particle Analysis of Secondary Organic Aerosol Produced from the Aqueous Phase Reaction of Ammonium Sulfate with Methylglyoxal. *ACS Earth and Space Chemistry*, 2(4), 2018.

Armando D Estillore, Holly S Morris, **Victor W Or**, Hansol D Lee, Michael R Alves, Meagan A Marciano, Olga Laskina, Zhen Qin, Alexei V Tivanski, Vicki H Grassian Linking hygroscopicity and the surface microstructure of model inorganic salts, simple and complex carbohydrates, and authentic sea spray aerosol particles. *Physical Chemistry Chemical Physics*, 19(31), 2017.

ABSTRACT OF THE DISSERTATION

**Nanoscale Microspectroscopic Analysis of Environmental Surfaces: Aerosol
and Window Glass**

by

Victor Wingtai Or

Doctor of Philosophy in Chemistry

University of California San Diego, 2021

Professor Vicki H. Grassian, Chair

Surfaces are ubiquitous in indoor and atmospheric environments. In the atmosphere, surfaces are present in the form of aerosols, which can impact climate by scattering or absorbing solar radiation and influencing cloud formation and precipitation processes. Sea spray aerosols are a major biogenic aerosol, whose physiochemical properties and composition are reflective of the marine environment. In indoor environments, surfaces are extremely diverse, ranging from walls to skin to window glass. Due to the higher prevalence of surfaces indoors, developing a molecular level understanding of surface processes is necessary for accurately understanding the role surfaces play in regulating indoor air

quality and consequently the health of the occupants.

In this dissertation, the surface properties and composition of window glass and sea spray aerosols are investigated. These surfaces are probed upon their nascent production and subsequent physical and chemical transformations under environmentally relevant conditions. In both environments, indoors and outdoors, due to the messy nature of authentic surfaces, comparisons are made back to simple model systems to provide molecular mimetics that can be used for future studies. Due to the small size scales of surface processes, higher resolution chemical analyses and imaging techniques reveal the chemical and morphological heterogeneities across the sample surface. Overall, these studies provide insights into how high resolution spectromicroscopic techniques can be utilized to elucidate nanoscale heterogeneous evolution of atmospherically and indoor relevant surfaces, and their subsequent reactions with trace gases.

Chapter 1

Environmental Surfaces and Nanoscale Analyses

1.1 Roles of Aerosols and Surfaces in Environmental Chemistry

Surface influences are pervasive across across many chemical and physical environmentally relevant processes.[2, 3, 4] The presence and interactions of surfaces can alter chemical processes, serving as reaction mediators or facilitators[5], or even catalyzing reaction processes.[6, 7] Physically, surfaces act as sinks and sources for mass transfer, as material is accumulated or released from the surface.[8, 9] As a result, surfaces play a dynamic role in interacting with and altering concentrations and fates of species. The capability and degree that surfaces influence these processes depends on the morphology, structure, and composition of the surface.[10, 11, 12] Additionally, the porosity, structure, viscosity, and phase of the underlying bulk material can influence the rates and degrees of material accumulation at the surface or diffusion into the underlying substructure.[13, 14] Modern advances in environmental surface chemistry involves the development of molecu-

lar level understanding of surface chemical reactions and physical processes.

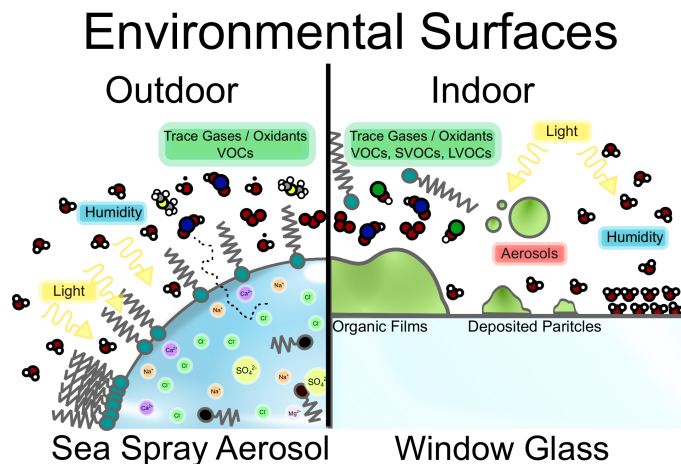


Figure 1.1: Cartoon representation of two atmospherically relevant surfaces - sea spray aerosol (left) and window glass (right), and their interactions with environmental conditions such as light, humidity, and gaseous compounds

Within atmospheric chemistry, aerosol particles have surfaces of interest due to the uncertainty that aerosols play in climate.[15] Aerosols are small liquid or solid particles suspended in air, and their surfaces that behave as reaction sites for uptake and transformation of gaseous species.[16, 17] Aerosols have a direct influence on the radiative budget via scattering and absorbing radiation, and indirectly effects in which aerosols alter larger scale processes such as cloud formation and even precipitation by acting as cloud condensation nuclei (CCN) or ice nuclei (IN).[18] However, the ability for a given particle to act as a CCN or IN, depends on numerous factors, each with their own corresponding complexities such as size, composition, morphology, phase state, viscosity, and the chemical distribution of species throughout a given particle.[19, 20, 21, 22, 23, 24]

The past decade has seen a resurgence in indoor chemistry, bringing in studies, techniques and expertise from atmospheric chemistry, contextualizing and integrating techniques and understandings into the indoor environment.[25, 26, 27] When discussing the indoor environment, not only are the indoor surfaces of aerosols important but surfaces more broadly are prevalent. Surfaces form the basis of indoor spaces, and span an extremely

wide range of materials and structures, including aerosol particles as already noted, but are also extended to include materials like vinyl, glass, paint, and humans. These surfaces similarly act as reaction sites and control concentrations of airborne constituents, influencing indoor air quality and the health of occupants. [2, 28, 29]

In both of these facets of outdoor and indoor environmental chemistry, surfaces, due to their pervasiveness, represent difficult but crucial subset of processes to both study and comprehend on a molecular level. It is necessary to probe not only the initial state of the nascent surface, but also subsequent transformations of the surface as it ages in its respective environment, and how many of these physiochemical properties of interest change over time. Interfacial interactions and reactions with gaseous species and mass transfer of particulate matter are often on nanoscale dimensions in size, but drive the macroscopic evolution of surfaces. Thus accurately depicting these surface processes requires physical and chemical probes that can capture these fundamental processes on relevant size regimes. Surfaces represent a dynamic and complex interactive site for environmental processes and transformations to occur. The integration of these molecular level studies with modeling and theoretical simulations provides a foundation for understanding and predicting surface processes spanning multiple magnitudes of spatial and temporal scales.

1.2 Sea Spray Aerosols Particles

Ocean covers 70% of the planet and is the largest source of biogenic aerosol particles. [30, 15] Sea spray aerosol (SSA) particles are produced from wave breaking and wind sheering and bubble bursting at the ocean surface. [31, 32, 33] Consequently, the composition of the SSA produced is dependent on the environmental condition and state of the marine ecosystem.

Production and Formation of Sea Spray Aerosol

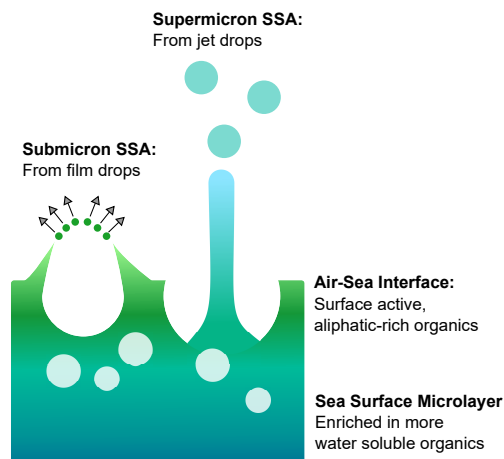


Figure 1.2: Schematic showing bubble bursting mechanisms for film and jet drops at the ocean surface. Figure adapted from Wang *et al.* 2015[1]

Wind stress at the ocean surface produces shear forces that gives rise to wave breaking and entrains air bubbles into the ocean. Droplets formed from bubble rising and bursting are the primary source of SSA formation.[34] The exact mechanism determines the depth of the ocean surface droplets are produced from, ultimately determining the aerosol particle composition, while the process mechanism and energy determines the size distribution.[33, 1] Jet droplets are formed from the disruption of a water jet formed by the collapse of a bubble cavity. As a result, jet droplets are from from the entrained air pulling material from the underlying near-surface water and transferring them across the interface and into the air. These jet droplets have been found to be largely supermicronic in size and enriched in inorganic salts of elements such as Na, Cl, Ca, and water soluble organic species. In contrast, film droplets are generated from bubble bursting at the air-sea surface interface. The upper-most film of the sea surface, the sea surface microlayer, is compositionally distinct from the underlying bulk seawater, as it is enriched in surface active organic mater. [] Subsequently, film droplets formed from bubble bursting in this region are enriched in aliphatic-rich organics, enzymes, and other surface active species

and largely submicronic in size.

The exact composition of SSA particles is also highly dependent on the state of the marine environment at the time of production. Past research has found that biological activity and phytoplankton blooms are responsible for dictating the chemical makeup of the seawater and SSA.[35, 1] Increased bloom activity enhances the abundance of aliphatic species in SSA. [1] However, low correlation and predictability based of aerosol properties solely off of chlorophyll-a (Chl-a), a biomarker for bloom activity, suggests that additional processes and parameters complicate the chemistry occurring in the marine environment. [36]

Mesocosm studies have demonstrated that bacterial metabolic processes during a phytoplankton bloom alters the size-dependent concentrations of organic species. During a phytoplankton bloom with high bacterial counts resulted in a loss of organic enhancement in submicronic SSA particles.[1] This phenomena has been attributed to bacterial grazing and metabolism of the byproducts, resulting on an enhancement of less surface active, more water-soluble species. Thus, bacterial processing reduces the relative concentrations of these organics at the air-surface interface, consequently reducing the transfer of these organic species into the submicron SSA.

Aerosol Mixing State

Adding to this complexity, there is a wide range of particle-to-particle chemical variability within a given distribution of particles from the same source.[37] This distribution of chemical species across an aerosol distribution is referred to as the mixing state, and has important implications for the properties of the individual particles such as light scattering, water uptake, gaseous species partitioning, and reactivity.[38, 3] There are two main classifications of mixing state: an externally mixed population where each particle is purely comprised of a single compound, and internally mixed where each particle

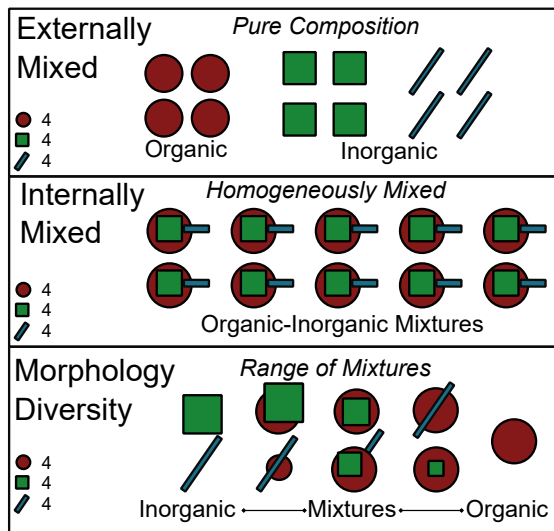


Figure 1.3: Cartoon representation of various mixing states of aerosol particles, externally mixed (top), internally mixed (middle), and morphologically diverse particles (bottom).

is comprised of equal proportion of all the chemical species present. However, the actual distribution of chemical species is much more complex when looking at them on a single particle basis, particles can adopt varying morphologies, such as rods prisms and rounded shaped particles.[37, 39] Mixtures of different species can result in heterogeneous morphologies with distinct phase separations that arise from non-mixing of species within a single particle, such as core-shell particles which are comprised of an inorganic core encased in an organic rich shell. Thus, SSA span a range of compositions, across pure inorganic salts to salt-organic mixtures to pure organics. Even within a single purely-organic particle, the non-mixing of different organic species can give rise to liquid-liquid phase separations.[40, 41] Phase separations and chemical heterogeneities within a single particle have been shown to have impacts on their hygroscopicity and ability to act CCN.[20] However, because individual aerosols can be as small as hundreds of nanometers, and many of these heterogeneities require sub-particle level analyses, the development and application of nanoscale resolution techniques and methodologies are necessary for accurate characterization and measurement of these aerosol properties.

Aerosol Hygroscopicity

Hygroscopicity refers to the affinity to take up water vapor from the surrounding environment.[42] Depending on the relative humidity (RH) and temperature, water vapor can partition into the aerosol phase, subsequently altering the concentrations of components within an aerosol.[43, 19] Aerosol liquid content has been shown to alter physiochemical properties of an aerosol such as phase state, morphology, size, and viscosity.[44, 45, 46, 47, 48] Aerosols with more water-soluble compounds that uptake more water are more hygroscopic than those that are more insoluble. However, because aerosols can adopt a wide span of morphologies and mixing states, the hygroscopicity of the subsequent mixed particle is not only dependent on concentration dependent properties, but also the morphology and any phase separations within.[49, 40] Thus, understanding both aerosol morphology and spatially distributions of chemical compounds is needed for understanding their hygroscopic behavior.

Oxidation

Recent efforts and advancements have been made developing a more comprehensive understanding of how the environmental state of the marine ecosystem are reflected in the composition and physical properties of nascent produced SSA. However, aerosols are not static systems, but rather transform and evolve dynamically in response to stimuli such as light[50], and are responsive to concentrations gaseous species. In the presence of reactive gases such as HOCl, OH radical and N_2O_5 , aerosols can readily undergo heterogeneous and multi-phase chemistry.[3] Aerosols surfaces can either facilitate reaction processes by catalyzing reaction mechanisms that are energetically unfavorable or partake in reaction processes directly, subsequently altering the chemical composition and physiochemical properties of the reacted aerosol particle. These multi-phase processes are reflected by changes in the morphology and chemical composition of the SSA, and subse-

quently alter the particle physiochemical properties such as hygroscopicity, viscosity, phase state, and light scattering.[51, 52, 53]

1.3 Indoor Surfaces

Understanding the chemical processes occurring in indoor spaces have garnered increased attention in the past decade. In developed societies, humans spend over 90% of their time in indoor spaces.[54] When examining relative contributions and processes indoors, surfaces significantly more widespread indoors relative to outdoors.[2, 25, 55] Surfaces are the fundamental basis for indoor spaces and objects, and influence the concentration and fates of the constituents of indoor air. The behavior of surfaces and surface accumulated material is thermodynamically driven by equilibrium of various semi-volatile and volatile species that can readily partition between different media, such as air, organic films, and surfaces. [9, 56, 8, 57]

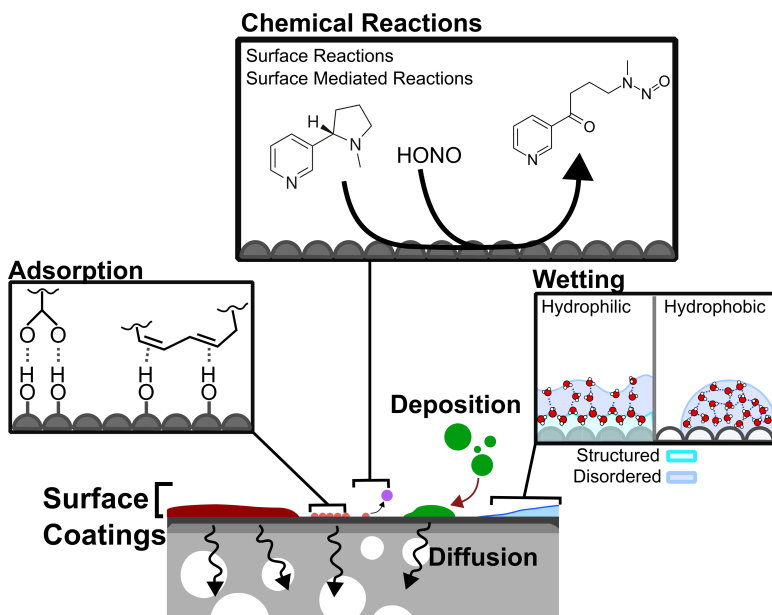


Figure 1.4: Diagram showing surface processes of interest to indoor surfaces, including transport of material onto the surface and transformative processes.

Indoor surfaces also play a role in transformation of indoor compounds by altering reaction mechanisms and or directly reacting with airborne species. If left unperturbed, materials accumulated on the indoor surface, or diffused within the bulk material, can remain entrained in indoor spaces for months or years.[8, 56] This means that when considering reactions and chemistry indoors, accommodating surfaces processes require consideration of slower reaction pathways that are longer than the air exchange rates- the typical rate limiting factor of indoor spaces[58]- or accumulation of indoor components that might otherwise be scrubbed via ventilation.[59, 60] However, surfaces are extremely messy and complex, as the interactions of a surface with airborne fraction is largely dependent upon the physical and chemical composition of the surface. Due to the large variety of materials found indoors, and the slew of different micro-environments, there is not a single surface that can be used to represent all indoor surfaces, nor is there a single reaction mechanism that represents all aging processes.

Diversity in Surface Materials and Indoor Emissions

Window glass is one of the simplest relevant indoor surface structurally and chemically, found across nearly all indoor spaces. Window glass is predominantly comprised of amorphous SiO_2 mixed with various amounts of sodium and calcium oxides. The surface is smooth and low in surface area, and typically thought of an inert surface. However, processes including surface wetting[61], transmissivity of attenuated sunlight[62], and the accumulation of material on surface[63, 64] makes the window glass surface suitable for numerous chemical and physical processes to occur. Indoor surfaces are extremely diverse, spanning from of natural and man-made materials, including but not nearly limited to glass, paint, human skin and clothing. Across the wide range of surfaces and surface materials, there is a reflective diversity in their corresponding composition and physiochemical properties such as roughness, wettability, and permeability or porosity. Further compli-

cating this, the evolution of a given surface is highly dependent on the relative surface location, and any activities and emissions carried out there within.



Figure 1.5: Examples of various sources of emissions indoors

Emissions indoors are similarly extremely diverse, being produced from a myriad activities and sources such as cooking and cleaning[65, 66, 67], electronic devices such as printers[68, 69, 70], or even passive emissions such as degassing from materials such as vinyl flooring.[71, 72, 73, 74] Some of these emissions are localized to specific regions or sites within indoor spaces, for example, printing is common in office spaces and cooking occurs primarily in the kitchen, while others can be more common spread such as off-gassing of phthalates flooring materials and plasticizers or formaldehyde and other volatile organic compounds from paint. While these emissions are more concentrated proximal to the emission source, their transport through indoor spaces, either via diffusion or through airflow such as centralized ventilation systems[75], adds to the challenge of understanding the chemistry and evolution of indoor surfaces. The ever increasing number of indoor products and materials produces exponentially scaling distinct permutations of potential surfaces and emissions that would have to be considered.

The complexity and diversity of these indoor surface systems and environments highlights the need to approach the surface science from a more fundamental molecular level aspect, and extend commonalities to new or additional surfaces and emissions. Integrating these studies with theory and modeling across multiple magnitudes of temporal and spatial scale builds the foundation for a more generalized understanding of indoor processes and their consequential influence on indoor air quality and occupant health. Because many interactions involve transport or transformations of gaseous compounds or submicronic sized particulate matter, the evolution of surfaces involves studying surfaces with vertical and lateral resolutions on the nanoscale.

1.4 Thesis Objective

The research presented herein focuses on the development and application of nanoscale microspectroscopic techniques for analyses of relevant surface for both indoor and outdoor environments. Experimental techniques used to analyze these surfaces were primarily atomic force microscopy (AFM) and atomic force microscopy based infrared spectroscopy (AFM-IR). Samples analyzed were generated using molecular mimetics in a laboratory environment or authentic surface samples collected from the field under environmentally realistic conditions.

Chapter 2 overviews the details of the instrumentation and experimental methods used in this study. A brief and basic theoretical description of the AFM and AFM-IR are included, as well as general methods and materials used for preparing both laboratory and field samples.

Chapter 3 describes the method development and validation for AFM-IR analyses in model system aerosol studies. Various systems comprised of pure- and mixtures of inorganic and organic species commonly identified in SSA are included, including ammonium

sulfate, sodium chloride, and various sugars and fatty acids.

Chapter 4 extends the analyses of substrate deposited aerosol particles to authentic SSA collected from a mesocosm experiment in a wave flume channel facility. Size dependent morphological distributions and corresponding spectra were collected and compared with known model systems to provide chemical context to the morphologies observed across a phytoplankton bloom. The influence of aging on the morphology and composition are also investigated.

Chapter 5 describes the evolution of window glass placed in different indoor locations. Surfaces are imaged with AFM and physical properties such as roughness, changes in surface area, and film coverage are examined, demonstrating the role that surface locality plays in its evolution across multiple months of exposure.

Chapter 6 involves probing glass surface evolution in response to a single day of cooking or cleaning activities in the kitchen. Comparisons of surface deposited materials with mass transport deposition models and airborne aerosol size distributions were conducted. Spectral analyses reveal the chemical speciation of these shorter term deposited materials, and is compared with spectra from bulk extracted material and long term exposed glass. Model surface systems generated in a Teflon chamber using oleic acid and window glass are compared to provide further insight.

Chapter 7 details the hygroscopic response of various coated window glass surfaces. Field samples involve the deposited particles on window glass from single day of stir fry cooking and a multi-month exposed window glass placed in the kitchen. The spectra and hygroscopic growth is compared to various laboratory mimetics based off of oleic acid, studying the influence of speciation, oxidation, and aliphatic chain length.

Chapter 2

Experimental Methods

The research presented in this dissertation focuses on the chemical and morphological evolution of different environmental surfaces. In this chapter, experimental methods and instruments are introduced, including substrate-deposited aerosol sampling and preparation and the theoretical basis, components, and operation of atomic force microscopy (AFM) and atomic force microscopy based infrared spectroscopy (AFM-IR) also referred to as atomic force microscopy based photothermal infrared spectroscopy (AFM-PTIR). Mathematical and physical descriptions are briefly discussed, but largely follow more detailed derivations available elsewhere.

2.1 Sample Preparation

2.1.1 Substrate Preparation for Aerosol Particles

Aerosol samples were collected by impacting particles onto silicon wafer chips (16008, TedPella) or 100-nm thick gold-coated wafers (AU1000SLC, Platypus Tech). All substrates were cleaned with ethanol and water, followed UV-Ozone cleaning. For hydrophobic treatment, Si wafers were coated by submerging in commercial polydimethyl-

siloxane solution followed by an ethanol rinse.

2.1.2 Aerosol Particle Model System Generation for Indoor and Outdoor Chemistry Studies

Solutions were prepared using 1% weight solutions in milli-Q water (Barnsted EasyPure-II; ≥ 18.2 M Ω cm resistivity, Thermo) or corresponding miscible solvent. From the solution, a polydisperse distribution of aerosols was generated using an atomizer (Aerosol Generator 3076, Mikromasch). Briefly, liquid is drawn through a vertical passage into an atomizing section, wherein the solution is atomized by a high-velocity stream of air, producing a polydisperse distribution of submicrometer aerosols, with a mean diameter of approximately 200 - 300 nm. Prior to collection, the resulting stream was reduced to a relative humidity (RH) of approximately 10% after passing through two diffusion dryers. For size selection, the particles were impacted onto substrates using a micro-orifice uniform deposition impactor (MOUDI, nanoMOUDI-II 125R, TSI). In the absence of size selection, the polydisperse distribution was impacted onto substrates by using an impactor (0.0508 cm, TSI) from an electrostatic classifier (3080, TSI) at a flow rate of approximately 0.3 LPM.

2.1.3 Field Sampling of Aerosol Particles and Indoor Surface Depositions

Aerosol Collection

Nascent SSA was collected by directly sampling flume headspace and impacting onto substrates in a MOUDI (MOUDI-110, TSI). Samples were collected under ambient temperature (25 - 30 °C) and 70-90% RH. Heterogeneously aged SSA (hSSA) was collected by flowing flume head space through an oxidation flow reactor (OFR) and mixed with a

bypass of liquid nitrogen before impacting onto substrates using a MOUDI (nanoMOUDI-II 125R, TSI) at ambient temperature (25 - 30 °C). Due to the liquid nitrogen bypass, samples were collected under drier conditions, at 15-20% RH. Substrates were immediately placed in sealed petri dishes and stored in the dark.

Indoor Surface Sampling

Window glass was purchased from commercial distributors and cleaved into approximately $1.3 \times 1.3 \text{ cm}^2$ pieces. Surfaces were then cleaned in subsequent alcohol and water rinses, and dried in an oven. Painted surfaces were prepared by applying a coating of paint onto of support material (wallboard, glass) and allowing to dry. All surfaces were mounted vertically and exposed to authentic indoor environments and conditions for variable amounts of time, ranging from a single day up to multiple months. Samples were sealed in air-tight containers and shipped to San Diego for analyses. Samples were stored in the dark under ambient conditions.

2.2 AFM

2.2.1 Components

While many potential configurations exist for atomic force microscopes, with numerous of auxiliary components that provide additional functionality, this section will only focus on the base components of the particular AFM used, shown in Figure 2.1, that provide the functionality needed for operation. All samples were analyzed using a commercial atomic force microscope system (nanoIR2, Bruker). Typically, reflective rectangular Si-N cantilevers with uncoated tips are used, with radius of $\sim 10 \text{ nm}$. For contact mode imaging low frequency flexible cantilevers (HQ:CSC17/Cr-Au, Mikromasch), with a nominal frequency and spring constant of 13 kHz and 0.18 N/m respectively. In tapping mode,

slightly more rigid cantilevers are used (HQ:NSC19/Al-BS, Mikromasch), with a nominal frequency and spring constant of 65 kHz and 0.5 N/m respectively, and for sticky samples such as oil and water droplets, rigid cantilevers are used (HQ:NSC15/Al-BS, Mikromasch) with a nominal frequency and spring constant of 325 kHz and 40 N/m respectively.

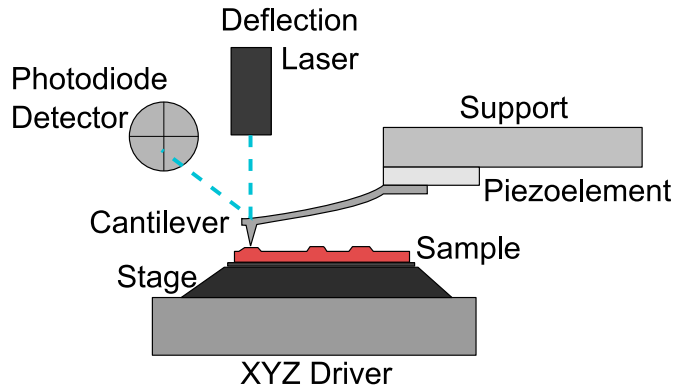


Figure 2.1: Diagram showing the main components of an atomic force microscope with an optical lever detection system to investigate substrate deposited particles from indoor and outdoor samples as well as model systems

The primary sensor for AFM is a cantilever with a sharp tip acting as the probe. The cantilever is held on a support with a piezoelectric element which upon applying a sinusoidal voltage, drives cantilever oscillation. Samples, often non-magnetic substrates such as silicon and glass, are adhered to steel discs and magnetically attached to a stage. Stage motion and position is controlled by a XY driver and Z driver to move the sample laterally and vertically relative to the probe. Cantilever motions are monitored using the optical lever configuration, in which a laser spot is reflected off the edge of the cantilever and onto a four quadrant photodiode detector. Changes in the bending of the cantilever are cast as lateral or vertical displacements of the laser spot on the photodiode detector.

2.2.2 Cantilever Motions and Mechanics

By measuring changes in the position or motion of the cantilever induced by tip-sample force interactions, AFM is able to provide insight into physical and morphological

properties of the sample. Cantilever mechanics follow equation of motion for flexural vibrations of a beam, approximated by the Euler-Bernoulli equation:

$$EI \frac{\partial^4 z(x,t)}{\partial x^4} + m \frac{\partial^2 z(x,t)}{\partial t^2} = W(x,t) \quad (2.1)$$

where z is the beam vertical displacement and $W(x,t)$ is the excitation force, dependent on position x and time t . EI is the flexural stiffness of the beam with mass m . Accounting for damping of the harmonic motion of the cantilever and including driving and tip-sample interaction forces gives:

$$EI \frac{\partial^4 z(x,t)}{\partial x^4} + \eta_{air} m \frac{\partial z(x,t)}{\partial t} + m \frac{\partial^2 z(x,t)}{\partial t^2} = F_d + F_{ts} \quad (2.2)$$

where η_{air} is the damping constant in air. The equation is solved by separation of variables and applying boundary conditions of zero deflection (z) and slope ($\frac{\partial z}{\partial x}$) at the fixed end and zero torsional moment ($\frac{\partial^2 z}{\partial x^2}$) and corresponding terms for forces ($\frac{\partial^3 z}{\partial x^3}$) acting at the free end of the beam. In time domain, the harmonic solutions of angular frequency ω can be expressed as:

$$\begin{aligned} z(x,t) &= (A_1 \sin \alpha x + A_2 \cos \alpha x + A_3 \sinh \alpha x + A_4 \cosh \alpha x) e^{i\omega t} \\ &= \sum_n \phi_n(x) q_n(t) \end{aligned} \quad (2.3)$$

where A_1 , A_2 , A_3 and A_4 are coefficients determined by the boundary conditions, $\alpha = \left(\frac{m}{EI} \omega^2\right)^{\frac{1}{4}}$, $q_n(t)$ is the temporal behavior and $\phi_n(x)$ is the spatial shape of mode n for the fundamental $n = 1$ and higher harmonic $n = 2, 3, \dots$ flexural eigenmodes. Eqn 2.2 can be rewritten recognizing that $\frac{d^4 \phi}{dx^4} = \frac{m}{EI} \omega^2 \phi(x)$:

$$\sum_{n=1}^{\infty} \omega_n^2 \phi_n(x) q_n(t) + \sum_{n=1}^{\infty} \frac{dq_n}{dt} + \sum_{n=1}^{\infty} \frac{d^2 q_n}{dt^2} = \frac{1}{m} (F_d(t) + F_{ts}(t)) \quad (2.4)$$

Through modal shape orthogonality, Eqn 2.4 can be decoupled to give ordinary differential equations describing the dynamics of each mode:

$$\frac{d^2q_n}{dt^2} + \eta_{air} \frac{dq_n}{dt} + \omega_n^2 q_n(t) = \frac{1}{m} (F_d(t) + F_{ts}(t)) \quad (2.5)$$

Additional complexities including but not limited to tip location along the cantilever, lateral forces, and beam tilt, are necessary for accurate numerical solutions to cantilever dynamics. However, the fundamental principal remains: interaction forces between the cantilever tip and sample surface alter the cantilever motion, detection and quantification of these dynamics provide access to the physical and topographical properties of the sample.

2.2.3 Standard Operating Procedures for Use of AFM and AFM-IR Spectroscopy

General AFM Modes

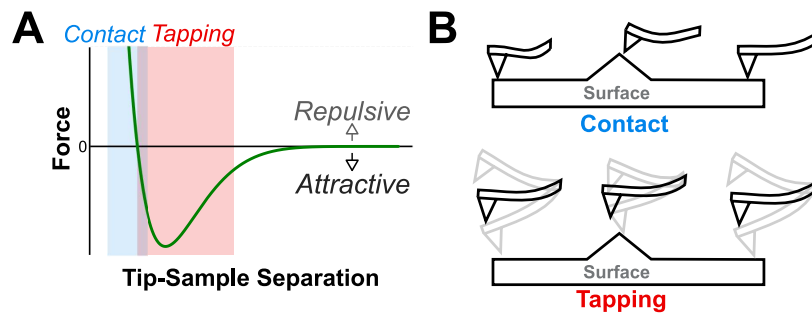


Figure 2.2: A) force-distance plot demonstrating the tip-sample force experienced by the probe across a range of tip-sample separations, ranging from attractive to repulsive regimes, with labeled regions of operation for contact and tapping AFM. B) Examples of tip motion as the probe sweeps across the surface in contact (upper) and tapping (lower) imaging modes

One of the simplest models for AFM tip-sample interactions is the Leonard-Jones Potential, Figure 2.2, describing the interaction potential $V(z)$ as a function of tip-sample

separation which varies depending on the imaging mode and conditions:

$$V(z) = \left[\left(\frac{A}{z} \right)^{12} - \left(\frac{B}{z} \right)^6 \right] \quad (2.6)$$

Where the tip-sample repulsive and attractive forces are described by the first and second terms respectively. Two main modes are employed and discussed in this thesis, contact (static) mode, and tapping (intermittent contact/vibrating) mode, shown in Figure 2.2B.

Contact Mode

In contact mode, the cantilever tip held in constant contact with the sample and drags across surface, operating in the repulsive force regime to prevent artifacts from attractive forces such as capillary or electrostatic/van der Waals forces. As sample is moved, changes in deflection of cantilever result from different topographies, reflected in vertical or lateral deflections. Operation in contact mode requires more flexible cantilevers with low spring constants so that sufficient deflection is achieved while keeping the interaction force between the tip and sample low. However, because the cantilever is in static contact with the sample, softer or weakly adhered regions of the sample are prone to disruption or dragging by the shear lateral forces.

Tapping Mode

In tapping or intermittent contact mode, the cantilever oscillated by the piezoelectric element at or near one of its resonant frequency eigenmodes, most commonly the fundamental mode. Oscillatory motion means tapping mode AFM operates across a wider range of tip-sample distances, involving both repulsive and attractive interaction forces. Because the cantilever is in constant harmonic motion, the amplitude of the laser on the photodiode is measured, as shown in Figure 2.3, where changes in sample topography are reflected in changes in the amplitude of cantilever oscillation. Phase shift between exci-

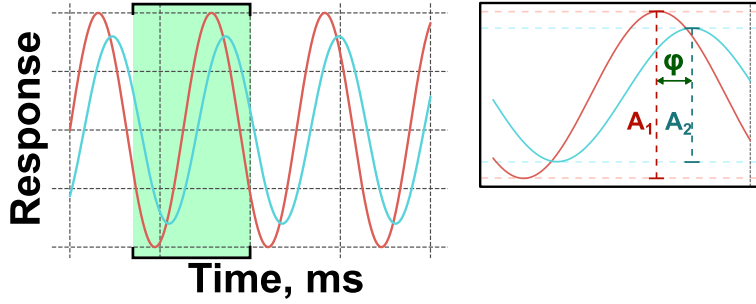


Figure 2.3: Example plot demonstrating phase and amplitude differences between the applied piezo signal (red) and the cantilever response (cyan), with a change in amplitude ($A_1 \rightarrow A_2$) and phase(ϕ)

tation and response of the cantilever, tied back to both topography of the sample and mechanical properties:

$$E_{diss} = \frac{k\omega}{2Q} [AA_0 \sin \phi - A^2] \quad (2.7)$$

For "stickier" samples such as liquids including oils and deliquesced salts, liquid capillaries are prone to forming as the tip approaches and retracts from the sample surface. Operating the AFM at a higher set-point and using higher frequency probes used to reduce influence of capillary forces, subsequently reducing the presence of these imaging artifacts.

2.2.4 Image Processing

All images were prepared and processed in Gwyddion. An example of image processing is shown in Figure 2.4. A majority of the samples imaged involve particles deposited on a flat substrate base, and corrections for height images only require plane subtraction or line fits, followed by iterative masked polynomial fits to level the underlying substrate. The substrate is zeroed as base height, and lower limit height mask is applied to the image, identifying particles relative to the zero height, and a minimum pixel area filter is applied to remove poorly resolved masked features. Properties such as surface area, volume, or roughness can be extracted from 1) the entire image 2) masked regions 3) unmasked regions

or 4) individual masked particles, and exported for analyses in Python, Igor, or Excel.

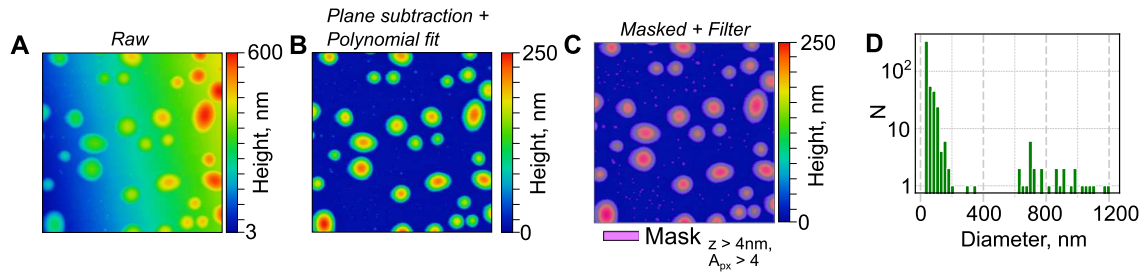


Figure 2.4: A) Raw output height image from AFM B) Height image after plane subtraction and masked polynomial fits% C) AFM image with masks identifying particles using a lower limit height threshold D) Histogram plot of masked data converted into volume equivalent diameters ($D_{equiv,V} = (6V/\pi)^{1/3}$)

2.3 AFM-IR Spectroscopy

2.3.1 Components

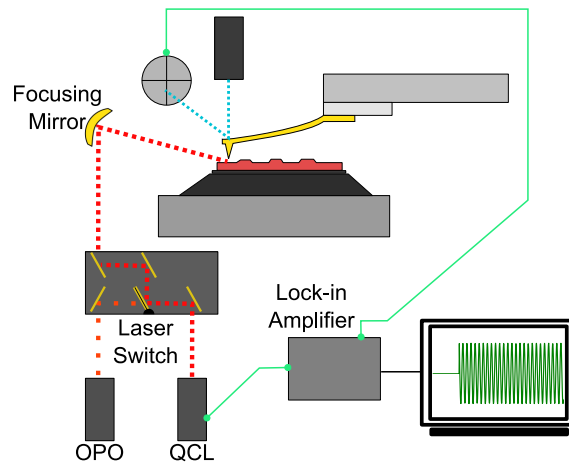


Figure 2.5: Image (left) and diagram (right) showing the main components of an atomic force microscopy-infrared spectrometer

Base components remain the same as AFM, with the addition of a pulsed tunable infrared laser source that is focused onto the sample beneath the cantilever tip, as demonstrated in Figure 2.5. Two separate laser sources are used, an optical parametric oscillator,

OPO, (NT-277-XIR, EKSPLA), with 1kHz repetition rate, 800 - 4000 cm^{-1} spectral range, 20 ns pulse width, and $\leq 12 \text{ cm}^{-1}$ resolution. A quantum cascade laser, QCL (MIRcat, Daylight), with 0.1 kHz to 3 MHz tunable repetition rate, 850 - 1800 cm^{-1} spectral range, 20 ns - 1 μs pulse width, and $\leq 1 \text{ cm}^{-1}$ resolution, both operated at p-polarization.

Gold-coated rectangular Si-N cantilevers are used with a tip radius of 10-35 nm. For contact mode imaging low frequency flexible cantilevers (HQ:CSC17/Cr-Au, Mikromasch), with a nominal frequency and spring constant of 13 kHz and 0.18 N/m respectively. In tapping mode, slightly more rigid cantilevers are used (HQ:NSC19/Cr-Au, Mikromasch), with a nominal frequency and spring constant of 65 kHz and 0.5 N/m respectively.

2.3.2 Theoretical Basis of AFM-IR spectroscopy

Full description and derivation treatment available in Dazzi *et al.* . Herein is an abbreviated version that closely follows, providing enough to give an intuitive understanding of the basis for chemical detection using AFM-IR. The overall phenomena driving AFM-IR's chemical sensitivity is photothermal induced resonance (PTIR), where sample absorbance of infrared light drives cantilever motion, demonstrated in Figure 2.6. Initially, the sample is irradiated with a pulsed, tunable infrared source. Power absorbed P_{abs} by the sample is dependent on the light absorbed A , which is governed by the traditional IR selection rule, requiring a nonzero induced change in the dipole moment ($\frac{d\mu}{dx} \neq 0$), commonly described by the Beer Lambert absorption law

$$P_{abs} \propto A(\sigma) = \frac{4\pi d}{\ln(10)} \sigma \kappa(\sigma) \quad (2.8)$$

where σ is the wavenumber of the incident light, κ is the imaginary part of the refractive index, and d is the thickness or cross-section. Absorbance results in a temperature increase

in the sample, described by the Fourier heat equation:

$$\rho C_p \frac{\partial T}{\partial t} = \frac{\Pi(t_p) P_{abs}}{V} + k_{th} \Delta T \quad (2.9)$$

where ρ is the density of sample with heat capacity C_p , T is the temperature, V is the volume, k_{th} is the thermal conductivity and Π is a rectangular function representing a laser pulse of length t_p . The temperature increase produces internal stress and subsequent thermal expansion of the region:

$$u(t) = aG\alpha_T \Delta T(t) \quad (2.10)$$

Photothermal expansion produces a source for tip-sample interactions F_{ts} . This expansion force induces displacement of cantilever, resulting in cantilever motion that is proportional to the optical absorption properties of the sample. Plotting changes in cantilever

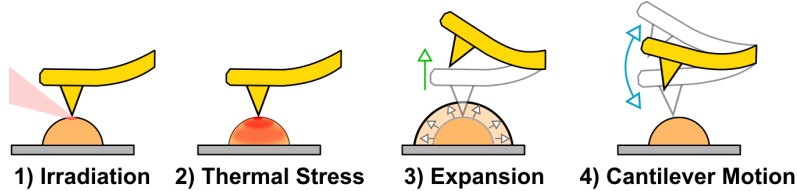


Figure 2.6: Main steps driving the photothermal induced resonance effect that enables cantilever motion and subsequent detection of infrared absorbance in the sample

behavior as a function of wavenumber reproduces an infrared spectrum where detected IR absorbance is local to the cantilever tip, resulting a lateral spatial resolution on the scale of tens of nanometers.

Contact AFM-IR Spectroscopy

In contact mode, AFM-IR spectroscopy operates by holding the tip in direct contact with sample, localized sample expansion deflects the cantilever, resulting in displacement

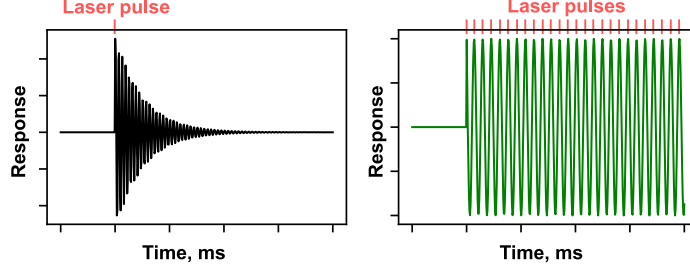


Figure 2.7: Cantilever response in ring-down decay from an OPO (left) and sustained resonance (right) from a QCL with pulse repetition rate matching cantilever oscillations

followed by ring-down decay oscillatory motion. Fixed repetition laser sources such as OPO's operate at a frequency too slow to match the expansion cycle of the sample, and thus the resulting tip-sample interaction can be treated as an impulse, approximated as a delta function $F_{ts} \approx \delta(x)$. With higher modular frequency laser sources such as QCL's, the frequency of the laser pulse repetitions can be set to match the contact frequency resonance enhancement results in sustained cantilever motion as shown in Figure 2.7. This results in enhanced signal to noise compared to conventional AFM-IR.[76]

Tapping-AFM-IR Spectroscopy

In contrast to standard AFM-IR where the probe is held in contact with the sample surface, tapping-AFM-IR involves measuring the tip-localized infrared absorbance while the tip is still held in oscillating motion. The overall basis for signal detection depends upon heterodyne mixing between frequencies of piezo oscillation force F_d and photothermal tip-sample force F_{ts} . The full derivation is available in Dazzi *et al.* 2018. Briefly, after a Taylor expansion of the overall response force, preserving second order terms, the approximate response force is:

$$F = \chi_s \left[\frac{a_t^2}{2} - a_s a_t \cos((\omega_t \pm \omega_s)t - \omega_s \tau) + \frac{a_s^2}{2} \right] \quad (2.11)$$

where the double product term describes heterodyne mixing of the two terms. By oscillating the frequency at its fundamental frequency $\omega_t = \omega_1$ and setting the laser pulse

frequency to match the difference between the second and fundamental modes of the cantilever $\omega_s = \omega_2 - \omega_1$, any sample absorption will result in maximum excitation amplitude of the second mode.

2.3.3 Operation

Laser calibrations are carried out prior to analyses, which involve using a background power spectrum to normalize for variations in power, in addition to running a polystyrene internal standard to account for shifts in frequency. Typical operation involves imaging samples (Figure 2.8A) identical to standard AFM operation, followed by some form of chemical analyses. Three main types of chemical data are provided by the AFM-IR: point spectra, chemical mapping, and hyperspectral imaging. For point spectra (Figure 2.8C), the tip is held at a fixed point and the laser sweeps across the spectral range. Measuring cantilever response as a function of wavenumber produce a single IR spectrum.

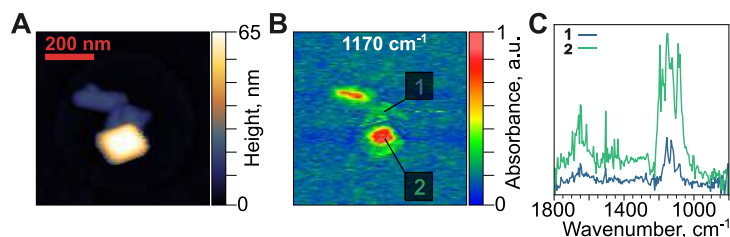


Figure 2.8: A) AFM height image of a particle on an Si wafer substrate B) Chemical map taken at 1170 cm^{-1} , C) IR Spectra taken at corresponding labeled regions of the particle

For single wavenumber chemical maps (Figure 2.8B), the IR source is held at a fixed frequency while sweeping cantilever across image, collecting simultaneously with height and other standard AFM images. For lasers like the OPO with a relatively slower, fixed repetition rate, scan speeds and co averages per pixel have to be reduced to prevent co averaging between pixels. For faster variable repetition rates such as QCL's, the laser repetition rate can be increased to match normal scan speeds.

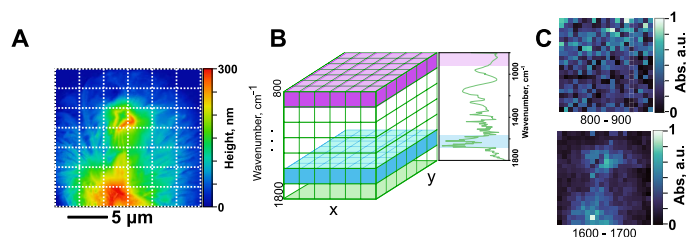


Figure 2.9: A) AFM height image of an organic particle on an Si wafer substrate B) Representative schematic of the hyperspectral data structure C) Integrated hyperspectral maps from 800 - 900 cm^{-1} and 1600 - 1700 cm^{-1} in upper and lower panels respectively

In hyperspectral imaging, a depiction of the data structure is shown in Figure 2.9. Spectra are collected at each point in an evenly-spaced grid across an image, wherein each X-Y data point contains an entire IR spectrum. Splicing a single frequency or integrating across a range of frequencies enables simultaneous mapping of functional groups across the same image.

2.3.4 Environmental Cell

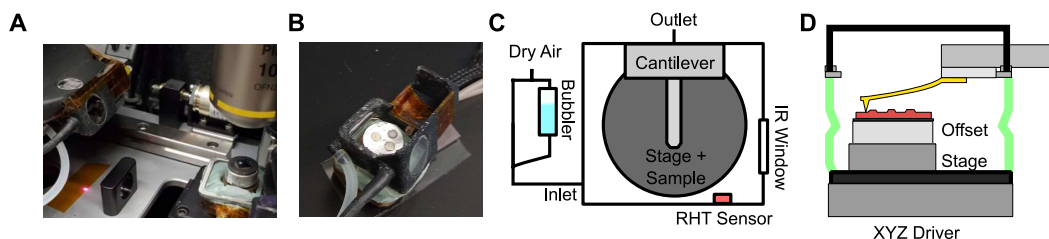


Figure 2.10: Images of the environmental cell A) in the AFM hood B) connected while detached from the AFM head, with a schematic of the primary components of the environmental cell attachment for the AFM-IR from C) overhead and D) side-on views

To facilitate *in situ* studies on chemical and physical surface transformations under variable temperature and humidity conditions, the AFM-IR was equipped with a closed environmental cell (Bruker), shown in Figure 2.10, that was attached to a liquid flow line. The cell walls are a heat-sealed low density polyethylene fabric. Cell lining material has to be flexible enough to permit stage motion and compression/extension for variable

thickness samples. Heat sealed low density polyethylene (LPDE) properly encloses the sample while remains flexible enough to not interfere with stage motion, with moderate ozone resistance. The chamber is equipped with a relative humidity and temperature sensor (SHT3x, Sensirion) near the AFM probe. The environmental cell is supplied controlled humidity airline which generated the desired humidity air by altering the mixing ratio between a dry and humid air line.

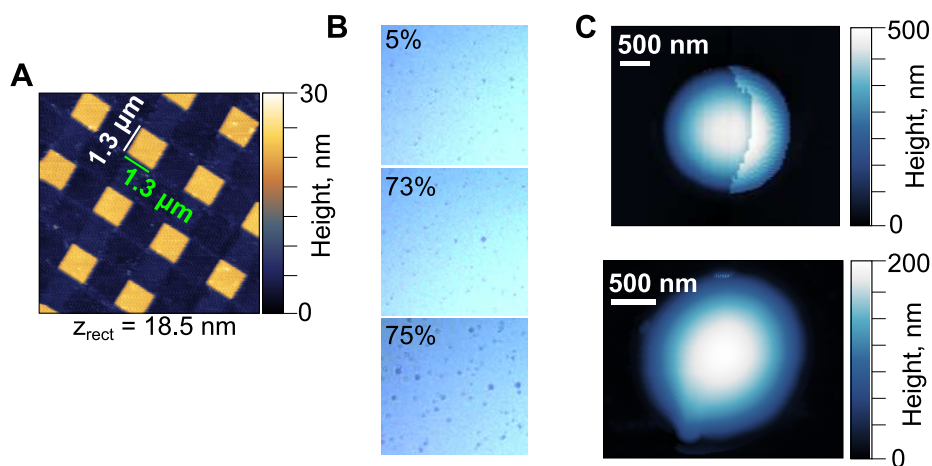


Figure 2.11: A) AFM height image of a calibration grating with $1.2 \times 1.2 \text{ cm}^2$ rectangular gratings imaged in the environmental cell B) optical images of NaCl at 5 (upper), 73 (middle), and 75% (lower) RH, particle growth is observed increasing the chamber to $\text{RH} = \text{DRH}_{\text{NaCl}} 75\%$ C) AFM height images of deliquesced NaCl at 80% RH with liquid capillary artifacts present (upper) and absent (lower) with inset scale bars are set to 500 nm; note the change in height scale.

After each assembly, the environmental chamber is calibrated prior to sample analyses to check for errors in stage movement, humidity sensor readout, or imaging artifacts. Examples of calibrations are shown in Figure 2.11. Stage movement with the cell is tested using 3-dimensional array rectangular gratings (TGQ1, NT-MDT) with nominal rectangle sides of $1.5 \pm 0.35 \mu\text{m}$ and heights of $20 \pm 1.5 \text{ nm}$. The humidity readout is validated by measuring the optical deliquescence of substrate deposited NaCl particles at its deliquescence relative humidity (DRH) of 75. Because the quality of the seal for the different parts of the chamber may vary between each assembly, adjustments in the seals made until

variances in the optically measured DRH do not exceeded $\pm 0.5\%$. Cantilevers are tested using deliquesced sodium chloride at 80% RH to ensure tip-sample liquid capillaries do not influence image quality. For higher humidity studies, where liquid phase state samples are expected, stiffer higher frequency cantilevers are used. Samples are typically imaged at slower scan speeds and higher set points to minimize interaction forces. Upon changing RH, the chamber is given at least 10 minutes to fully stabilize and equilibrate. After this amount of time, no further changes are observed in the images.

Chapter 3

Application of Nanoscale Infrared Spectromicroscopy for Model System Aerosol Studies

3.1 Abstract

New developments in nanoscale analytical techniques have paved the way for detailed spectroscopic and microscopic measurements of substrate-deposited aerosol particles on a single particle basis. Atomic force microscopy based photothermal infrared (AFM-PTIR) spectroscopy is a technique that combines the nanometer spatial resolution of AFM with the chemical analysis capabilities of vibrational IR spectroscopy. Herein we demonstrate the capability of AFM-PTIR to investigate single and multi-component systems comprised of inorganic salts and organic compounds relevant to the atmosphere. Chemical and microscopic characterization of individual particles as small as 50 nm in diameter is shown. Moreover, single particle spectro-microscopic characterization as a function of relative humidity using this technique is shown for the first time. These new measurements

as a function of relative humidity allow for the simultaneous and independent acquisition of photothermal IR spectra, contact resonance frequency shifts, and water uptake growth factors, providing insight on changes in the composition, stiffness, and size of the particles, respectively. These results lay the foundation for more detailed AFM-PTIR studies of multicomponent aerosol particles under a range of environmental conditions.

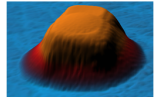
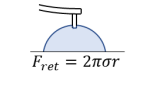
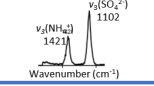
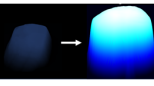
3.2 Introduction

Earth's atmosphere contains suspended liquid and solid particles called aerosols, which are directly emitted from a variety of sources (primary aerosols) or formed in the atmosphere through gas-to-particle conversion processes (secondary aerosols).[17, 16, 77] The interaction of atmospheric aerosols with solar radiation is complex, and the quantitative impacts of aerosols on climate and environment have many uncertainties due to different physicochemical properties such as their size, reactivity, and affinity to interact with water vapor to form clouds. [78, 79, 80, 30] In addition, human exposure to aerosol particles have been linked to a variety of health effects. [81, 82, 83, 84, 85]

Several recent field campaigns report variation in the chemical composition and morphology of individual particles, which reflects diversity in the particle emission sources. [39, 86, 87, 88, 89] A single aerosol particle typically consists of a mixture of components; with many aerosols containing both organic compounds and inorganic salts. The presence of organic compounds within inorganic salt aerosols in a mixed state can strongly alter the chemical reactivity and physical properties of the aerosol.[90] Thus, increasing interest has been placed on studying the composition, morphology, and phase state of aerosol particles comprised of both organic compounds and inorganic salts. Adding to this complexity, the components within the particle can vary in mixing states, resulting in different internal and external morphologies and corresponding phase states. [91, 92, 93] Morphology, phase, and

chemical composition are the vital links to understanding the impacts of aerosol particles in the atmosphere, and there is a need for detailed studies of individual particles under realistic atmospheric conditions.

Table 3.1: Aerosol particle properties that can be measured using AFM compared to AFM-PTIR spectroscopy

Property	Parameter	AFM	AFM-PTIR
Morphology 	<i>Particle size:</i> high resolution of a single particle's height, deposited diameter, and volume equivalent diameter.	✓	✓
	<i>Particle shape:</i> measure the relative geometric shape of the deposited particles (asphericity, aggregates, etc.)	✓	✓
	<i>Mixing state:</i> examines phase separations within particles (core-shell, partially engulfed, etc.) and the relative organic coating (organic volume fraction)	✓	✓
	<i>Aspect ratio:</i> measures the relative degree of particle deformation after being impacted on the substrate by taking the ratio of the deposited height vs diameter.	✓	✓
	<i>Reaction rates:</i> measure time dependent morphological and physical changes of particles exposed to reactive gases	✓	✓
Mechanical Properties 	<i>Adhesion interactions:</i> interaction forces between a functionalized cantilever and a surface of interest as a function of sample-tip separation	✓	✓
	<i>Dissolution:</i> imaging of aerosol particles in various solvents as a function of time	✓	✓
	<i>Surface tension:</i> measures the retention force between a constant diameter nanoneedle and a liquid particle	✓	✓
	<i>Frequency mapping:</i> spatial distribution of the contact resonance frequencies between the tip and sample, which shift as a function of sample stiffness	✓	✓
Chemical characterization 	<i>Reaction rates:</i> measure time dependent spectral changes in particles exposed to reactive gases	✗	✓
	<i>Chemical mapping:</i> spatial distribution of the photothermal induced resonance between the tip and sample	✗	✓
	<i>PTIR Spectroscopy:</i> cantilever localized detection of particle absorption of infrared radiation, via temperature increase and subsequent expansion	✗	✓
Hygroscopicity 	<i>Hygroscopic Growth Factor:</i> compares volume equivalent diameters for substrate deposited particles as a function of relative humidity.	✓	✓
	<i>Phase State:</i> examines viscoelastic response distance and relative indentation depth of the nanoneedle with the particle to determine phase state and transitions.	✓	✓
	<i>Resonance frequency shifts:</i> measures shifts in the contact resonance frequency as the particle softens or hardens due to water intake or release.	✓	✓
	<i>Spectroscopic changes:</i> localized PTIR spectroscopy observes the chemical signature changes within the particle due to water uptake or loss.	✗	✓

Atomic force microscopy (AFM) is an attractive and non-destructive method that permits visualization of the microscopic details of a particle with nanoscale spatial resolution at ambient conditions.[94, 95] Table 3.1 summarizes some of the important recent advances by Tivanski, Grassian and co-workers in using AFM to investigate atmospherically relevant particles including accurate measurements of particle size, three-dimensional (3D) structure, morphology, phase, 3D growth factors, organic to salt volume fraction ratio for mixed particles, and surface tension force measurements as a function of relative humidity. [1, 96, 19, 22] While AFM can probe the structural detail and physicochemical properties of individual atmospheric particles, it cannot directly provide chemical information about the particle. What remains a grand challenge in aerosol research is the simultaneous measurements of the chemical composition, morphology, and properties of

individual aerosol particle especially in the nanometer size range, a size regime important for atmospheric chemistry,[97] health and climate.[98, 99]

Atomic force microscopy based photothermal infrared (AFM-PTIR) spectroscopy is a photothermal induced resonance (PTIR) technique that combines the high spatial resolution of AFM with the chemical analysis capabilities of vibrational spectroscopy.[100, 76, 101] Briefly, the technique converts thermal expansion which originates from the absorption of infrared radiation, into cantilever displacement, generating a signal proportional to the amount of IR light absorbed. Because the displacement measured is localized to the cantilever tip, AFM-PTIR allows chemical analysis with spatial resolution well below the diffraction limit. AFM-PTIR has been successfully employed in various fields, including polymers, life, medical, and material sciences.[100] More recently, Bondy *et al.* have demonstrated AFM-PTIR spectroscopy to investigate atmospherically relevant aerosol particles, but noted issues such as low deflection signal from photothermal particle expansion, especially for small particles below 200 nm, and differing peak-to-peak ratios compared to Fourier Transform Infrared (FTIR) spectroscopy. [102]

Thus, there remains a need to further develop AFM-PTIR spectroscopy as a quantitative tool for analysing substrate-deposited aerosol particles. Herein, we use AFM-PTIR to measure the particle morphology and the associated chemical information of several model aerosol particles on a single particle basis. We present results for the infrared spectroscopic characterization of single component aerosol particles, including ammonium sulfate (AS) particles as small as 50 nm in diameter. Such small size range is important due to relatively high abundance of particles below 100 nm in the troposphere and their importance as cloud condensation nuclei and ice nucleators.[98, 23, 103] In addition, we provide similar characterization of particles as large as 2.6 microns in diameter. Previous studies have shown supermicron sized particles contribute to a significant fraction of total ice nucleators (IN).[23] To further demonstrate AFM-PTIR as a technique for studying

particles comprised of components that vary in both chemical and physical properties, we present results for two component model aerosols comprised of an organic compound, (pimelic acid (PA) and glucose) and an inorganic salt, (sodium chloride and ammonium sulfate). These were selected as important model systems of tropospheric aerosol particles which are majorly comprised of sea salt, inorganic sulfates, dicarboxylic acids, and saccharides. We also show results for collecting AFM-PTIR images and spectra of a single particle as a function of relative humidity for the first time. A summary table of the advancement in capabilities for aerosol studies using the AFM-PTIR method is provided in Table 3.1. When compared to a stand-alone AFM, AFM-PTIR spectroscopy gives information on the samples mechanical and spectroscopic changes that can be coupled with the imaging and tip-probe measurements from AFM to give a more complete picture of the behaviour of aerosol particles in the submicron size regime.

3.3 Experimental Methods

3.3.1 Materials

All chemicals used were purchased directly from the manufacturers, utilized without further purification, and included ammonium sulfate ($(\text{NH}_4)_2\text{SO}_4$, $\geq 99\%$, Fischer Scientific), sodium chloride (NaCl , $\geq 99\%$, Fischer Scientific), glucose ($\text{C}_6\text{H}_{12}\text{O}_6$, $\geq 99.0\%$, Sigma-Aldrich), sodium nitrate (NaNO_3 , $\geq 99\%$, Sigma-Aldrich), pimelic acid ($\text{C}_7\text{H}_{12}\text{O}_4$, $\geq 99.0\%$, Sigma-Aldrich). Single component aerosol particles were generated from a 0.5 or 1% wt/v aqueous solution using ultrapure water prepared on site (Barnsted EasyPure- II; $\geq 18.2 \text{ M}\Omega \text{ cm}$ resistivity, Thermo). Aqueous solutions of compounds (and 1:1 %wt mixtures) listed above were atomized (TSI Inc., model 3076) to generate the aerosol particles. The aerosol particles were then sent through two diffusion dryers (model 3062, TSI) at a flow rate of 1.5 lpm to reduce the RH to ca. 5% RH. Zinc sulfide (ZnS) and Si wafer

sampling substrates (16008, Ted Pella) were used to collect the aerosol particles by mounting the substrate in front of an electrostatic classifier (TSI Inc., model 3080) for 1-10 min. Due to the thickness of the ZnS substrate, samples could not fit in a MOUDI or CASCADE size selector. For relative humidity studies, hydrophobic substrates were prepared by cleaning Si wafer sampling substrates with isopropanol and coating in commercially available Rain-X. [104, 105]

3.3.2 Atomic Force Microscopy - Photothermal Infrared Spectroscopy

Samples were analyzed using a commercial microscopy system (nanoIR2, Bruker). The instrument consists of an atomic force microscope integrated with a pulsed, tunable infrared optical parametric oscillator (OPO, NT-277-XIR,EKSPLA) laser source with repetition rate of 1 kHz, tuning range of 850 to 2000 cm^{-1} and 2235 to 3600 cm^{-1} , and an average spectral resolution of 4 cm^{-1} . The sample is irradiated with a pulsed IR laser radiation in a top-down fashion, with a spot size of $\sim 30 \mu\text{m}$. The pulsed radiation is selectively absorbed by the sample, causing rapid and transient thermal expansion, which is locally detected by the resulting mechanical deflection change of the AFM probe. The deflection signal is divided by the background level of the IR source at each wavenumber to remove effects of power variation, and PTIR spectra are produced by plotting the resulting signal as a function of wavenumber. Under these typical conditions, acquiring a single PTIR spectrum over an individual particle takes approximately 10 minutes. For this study, to minimize damage to the particle, the OPO laser was operated at the lowest power that provided resolvable spectra, up to a maximum of 0.08 mW (0.9 - 3.0% power). Particle damage in a pure organic particle was not spectrally observable until the laser power reached 0.16 mW, as shown in Figure S3.1 (See the ESI[†]).

AFM imaging of the laboratory generated aerosol particles were conducted at T

= 298 K, and relative humidity (RH) of ~10-20% at ambient pressure. AFM images at a scan rate of 0.5 Hz using gold-coated silicon nitride probes (tip radius \approx 30 nm) with 0.07-0.4 and 1-7 N m⁻¹ spring constants, and 13 ± 4 and 75 ± 15 kHz resonant frequencies, in contact mode or tapping mode, respectively. Both probes have a lateral resolution of greater than 30 nm and allow for PTIR spectra acquisition, but vary in their imaging potential. In contact mode, the probe is left in contact with the sample and moved to a user-defined region, whereas in tapping mode, the probe is moved to a user defined location and then brought into contact with the sample. The probe is held in contact with the sample throughout the PTIR spectrum acquisition (loading force \approx 0.3 - 6.0 nN.) The contact mode probe allows for chemical and contact frequency mapping, whereas the tapping mode probe generates phase images. Photo-thermal IR spectra were collected with a spectral resolution of at least 8 cm⁻¹, averaging 128 laser pulses per wavenumber. All spectra shown were taken on a single point on the particle, without any averaging of spectra or smoothing filters applied. Unless denoted otherwise, spectra were collected at the highest point of the particle. Single wavenumber chemical maps are obtained by fixing the IR source to a single wavelength and irradiating the sample as the AFM raster scans. Chemical maps were collected at a scan rate of 0.05 Hz, averaging 16 times per pixel. For the water uptake measurements, the AFM head and the aerosol sample were contained within an environmental chamber system (Bruker) equipped with humidity and temperature sensor. The RH was adjusted by varying the ratio of wet and dry air controlled by a commercial dry air generator(model NDC-600, Nano Purification Solutions), across the range from 0 to 90% RH. RH sensor (SHT3x, Sensirion) inside the sample chamber was used to monitor the RH to within $\pm 1\%$.

3.3.3 FTIR Measurements: Multi-Analysis Aerosol Reactor.

The FTIR extinction measurements of aerosol particles were performed on a Multi-Analysis Aerosol Reactor System (MAARS). Details of this apparatus have been described previously. [106, 107] Briefly, the instrument is equipped with an aerosol generator, RH sensors, an IR extinction chamber with a pathlength of 78 cm which is positioned along the path of the IR beam (Nexus Model 670, Thermo-Nicolet spectrometer) equipped with a nitrogen liquid cooled MCT-A detector.

3.3.4 Volume Equivalent Diameters for Substrate Deposited Particles and Three-Dimensional Growth Factors

To account for any particle deformation from impaction, aerosol particles sizes are reported as the diameter (D) of a sphere with equivalent volume (V).

$$D = \sqrt[3]{\frac{6V}{\pi}}$$

Following the method used by Morris et al. [45] volume growth factors determined by AFM were quantified by taking the ratio of the volume equivalent diameters for the particle at a particular RH to that of the dry particle.[45]

$$GF_{vol}(RH) = \frac{D_{vol}(RH)}{D_{vol}(Dry)}$$

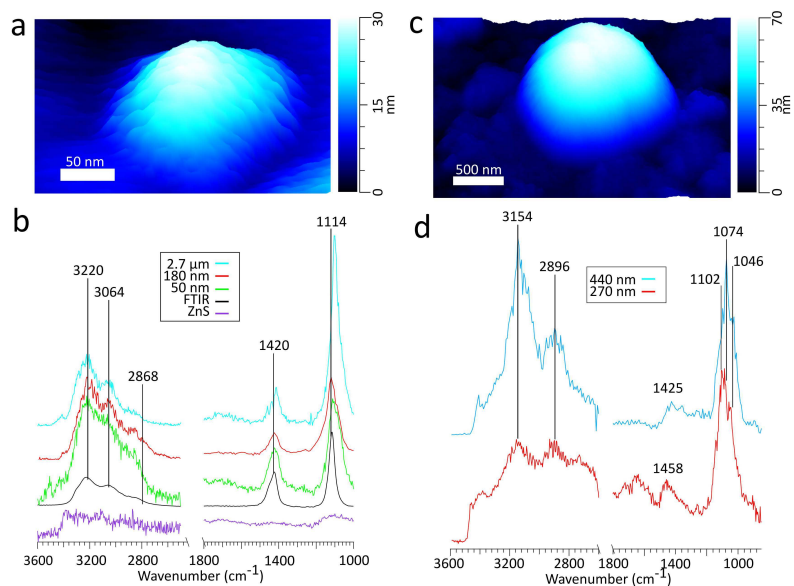


Figure 3.1: a) 3D height image of an ammonium sulfate particle on ZnS substrate with a volume equivalent diameter of 50 nm b) Comparison of the spectra obtained by FTIR (black) to PTIR for particles with volume equivalent diameters of varying sizes and the ZnS substrate. The peak frequencies in the figure correspond to the 180 nm sized particle. There is some variability in the peak frequencies, detailed in Table 3.2. c) 3D height image of a glucose particle on ZnS substrate with a volume equivalent diameter of 270 nm. d) PTIR spectra of glucose particles of varying sizes, denoted by the volume equivalent diameter.

3.4 Results and Discussion

3.4.1 Single-Component Aerosols

Ammonium Sulfate.

Figure 3.1a shows the 3D AFM height image of an ammonium sulfate particle (RH $\sim 10\%$) with a volume equivalent diameter of 50 nm on an IR inactive ZnS substrate. Figure 3.1b shows the spectral region extending from 850 to 3600 cm^{-1} , the important spectral regions for ammonium sulfate infrared bands. The blue, red, and green spectra show the AFM-PTIR spectra obtained on single particles of 2.7 μm , 180 nm, and 50 nm in volume equivalent diameter, respectively. The black spectrum shows a comparison spectrum taken

using FTIR extinction spectra of an ensemble of AS particles. A PTIR spectrum of the ZnS substrate is shown in purple. Both AFM-PTIR and FTIR spectra shows three of the four IR-active vibrational modes of the ammonium sulfate salt: $\nu_3(\text{NH}_4^+)$ (3230, 3064, 2868 cm^{-1}), $\nu_4(\text{NH}_4^+)$ (1424 cm^{-1}), and $\nu_3(\text{SO}_4^{2-})$ (1120 cm^{-1}), with peak comparisons summarized in Table 3.2. [108] The fourth vibrational mode of AS occurs at a frequency inaccessible by the tuning range of the OPO laser (below 850 cm^{-1}).

Table 3.2: PTIR and FTIR of Ammonium Sulfate particles and peak intensity ratios between $\nu_4(\text{NH}_4^+)$ and $\nu_3(\text{SO}_4^{2-})$

Vibration ν , cm^{-1}	PTIR				FTIR
	2.7 μm	180 nm	110 nm	50 nm	
$\nu_3(\text{SO}_4^{2-})$	1100	1120	1109	1112	1124
$\nu_4(\text{NH}_4^+)$	1412	1424	1426	1420	1420
$\nu_3(\text{NH}_4^+)$	2864	2868	2860	2860	2860
	3074	3064	3074	3064	3036
	3224	3220	3224	3216	3230
$\nu_4(\text{NH}_4^+):\nu_3(\text{SO}_4^{2-})$	1:5.0	1:3.1	1:2.1	1:1.9	1:2.4

Table 3.2 compares peak intensity ratios between $\nu_4(\text{NH}_4^+)$ and $\nu_3(\text{SO}_4^{2-})$ vibrational modes across the various sized particles in PTIR and the FTIR spectra. The PTIR spectra for submicron particles yields $\nu_4(\text{NH}_4^+):\nu_3(\text{SO}_4^{2-})$ peak ratios of 1:3.1, 1:2.1, and 1:1.9 for the 180, 110, and 50 nm diameter particles, respectively. The ratios for the submicron particles ($1:2.4 \pm 0.9$) are comparable to the peak ratio of 1:2.4 obtained for the FTIR spectra of an ensemble of particles. However, when examining the supermicron size regime, the 2.7 μm diameter particle gives a $\nu_4(\text{NH}_4^+):\nu_3(\text{SO}_4^{2-})$ peak ratio of 1:5.0, much larger than that of the submicron sized particles. Because PTIR signal depends on both the sample thickness and the absorbed energy per unit area (U_{abs}), [109] this deviation may be attributed to the nonlinearity of the PTIR technique beyond 1 μm in sample thickness and also differences in the power absorbed by the AS particle between the two wavelengths. Signal intensity at a given wavelength has been found to increase linearly with sample

thickness up to $\sim 1200 \mu\text{m}$, and continues to increase nonlinearly with increasing thickness until reaching a wavelength dependent maximum.[110] The nonlinear behavior has been attributed to the exponentially decaying electric field in the sample at greater thicknesses. Additionally, in the supermicron particle, deviations in $\nu_4(\text{NH}_4^+):\nu_3(\text{SO}_4^{2-})$ peak ratios may arise from differences between the U_{abs} by the two vibrational modes, where U_{abs} is expected to be greater at $\nu_3(\text{SO}_4^{2-})$ mode due to a larger absorption coefficient and penetration depth relative to the $\nu_4(\text{NH}_4^+)$ mode.[111] Thus, even in the size regime where peak intensity growth is linear, the rate of growth may differ between the two vibrational modes. Comparing the relative intensities of these peaks with the $\nu_3(\text{NH}_4^+)$ mode is less straightforward due to the difference in the pulsed laser sources used in the two different regions.

Examining the PTIR spectrum for the 50 nm diameter AS particle, distinct peaks are present at $\nu_3(\text{NH}_4^+)$ (3230, 3036, 2860 cm^{-1}), $\nu_4(\text{NH}_4^+)$ (1420 cm^{-1}), and $\nu_3(\text{SO}_4^{2-})$ (1112 cm^{-1}). The high signal from all vibrational modes suggests that chemical characterization can be conducted for particles on the sub-50 nm scale. AFM-PTIR spectroscopy is highly suitable for morphological and chemical characterization of particles around the size regimes necessary for both cloud condensation nuclei (CCN) and IN studies, where we demonstrate the capability to image and characterize particles across several magnitudes of atmospherically relevant size ranges.

Glucose.

To demonstrate AFM-PTIR's ability to analyze organics, glucose particles deposited on a ZnS substrate were used. Figure 3.1c shows the height image of a glucose particle with a 270 nm volume equivalent. Figure 3.1d is the PTIR spectra taken on particles of various sizes, with the peak assignments described in Table 3.3.[112] The peak around 1640 cm^{-1} in the 270 nm sized particle can be attributed to residual water from

the particle. In pure organics like glucose, the compounds are more viscous relative to inorganic salts,[19] making imaging in contact mode AFM more difficult as the sharp AFM tip will result in stronger particle tip-particle interactions that can lead to tip-induced particle movement or even tip-induced particle destruction. For more fragile samples, operating AFM-PTIR spectroscopy in tapping mode is preferred to prevent damaging the sample. However, the spring constants differ by roughly one order of magnitude, with 0.07-0.4 and 1-7 N m⁻¹ spring constants for contact and tapping mode probes, respectively. The larger spring constant in the tapping mode probe means that the cantilever deflection sensitivity to the photothermally induced particle expansions will be much lower than that for the more flexible contact mode tip.

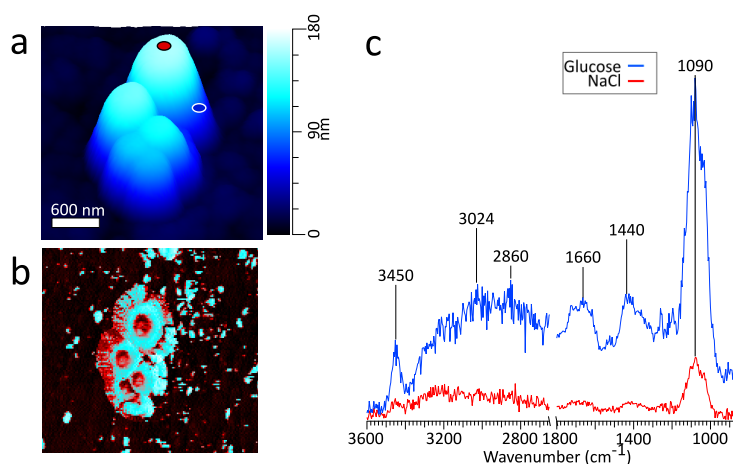


Figure 3.2: a) 3D height image of a cluster of NaCl/glucose (1:1 mass ratio) particles on ZnS substrate, with a volume equivalent diameter of 480 nm b) Phase image c) PTIR spectra taken at NaCl-rich (red) and glucose-rich (blue) regions with the corresponding locations marked in panel a).

Table 3.3: Peak assignments for glucose vibrational modes observed in AFM-PTIR spectroscopy

Vibration	ν (cm^{-1})	
	PTIR	Literature[112]
$\nu(\text{CO}) + \nu(\text{CC})$	1046, 1074, 1102	1025, 1050, 1111
$\delta(\text{CH}_2) + \delta(\text{OCH}) + \delta(\text{CCH})$	1425, 1458	1382
$\nu_{as}(\text{CH})$	2896	2913
$\nu_s(\text{CH})$	2952	2944
$\nu(\text{OH})$	3144, 3408	3003, 3410

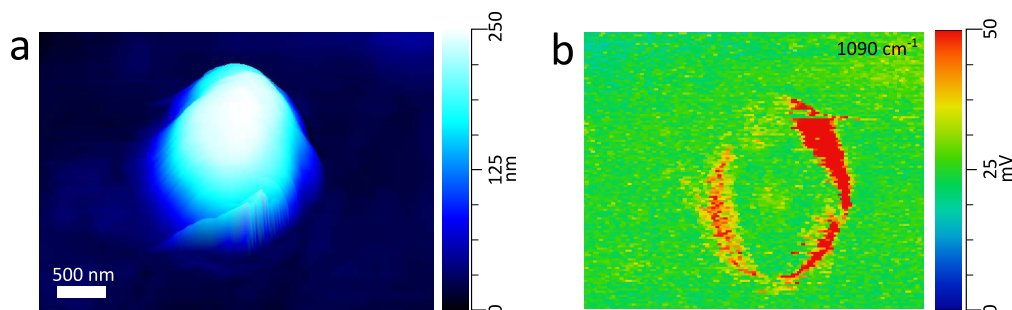


Figure 3.3: a) 3D Height image of a NaCl/PA (1:1 mass ratio) particle with a volume equivalent diameter of 510 nm b) Chemical map of the glucose rich regions of the particle taken at 1090 cm^{-1} .

3.4.2 Two-Component Aerosols: Mixed Inorganic Salts and Organic Compounds

Glucose Mixed with Sodium Chloride.

Shown in Figure 3.2a and Figure 3.2b is the height and phase image of a cluster of particles comprised of NaCl and glucose, wherein the particles exhibit a partially engulfed phase separated morphology at a 1:1 NaCl:glucose mass ratio.[19] Figure 3.2c shows the PTIR spectra taken at two phase separated locations on the particle. The spectrum corresponding to the glucose-rich core corresponds well with the PTIR spectrum of the 270 nm glucose particle in Figure 3.1d. Similar to the glucose particle, the broad peak at 1660 cm^{-1} is indicative of water content in the glucose-rich shell. The spectrum for the IR inactive NaCl-rich core shows significantly less intensity than that of the IR active

glucose-rich shell. However, some signal from the core can be attributed to a thin layer of organic coating. Detection of thin organic coatings is possible, albeit less intense peaks are much less resolvable. While point spectra are useful for identifying species, it does not provide an explicit description of the spatial distribution of chemical species. AFM-PTIR provides single wavenumber chemical maps of materials with nanometer spatial resolution by irradiating the sample with the IR source tuned to a single wavelength throughout the AFM scan. Mapping wavenumbers were selected by examining PTIR spectra for absorption frequencies exclusive or predominant for one region. A separate particle was imaged (Figure 3.3a) and a chemical map was acquired at 1090 cm^{-1} , shown in Figure 3.3b. In the chemical map, a majority of the signal at 1090 cm^{-1} arises from the $\nu(\text{C-O}) + \nu(\text{C-C})$ modes of the organic-rich glucose crown of the particle, while the IR inactive ZnS substrate and sodium chloride rich core remain relatively inactive. Compared to single-point spectra, chemical maps have far lower S/N, which is due to the significantly lower co-averaging used in chemical mapping, and thus was unable to detect any thin film organic coating on the NaCl-rich core. To obtain monolayer level sensitivity, more sophisticated methods such as resonance-enhanced AFM-PTIR are required.[113] AFM-PTIR chemical maps excel by providing nanoscale spatial distributions of chemical species. In previous studies, AFM analysis of organic volume fractions from AFM phase images operated under the assumption that the particle core is the inorganic component and the shell is the organic component. [19] With chemical maps, we explicitly demonstrate the organic and inorganic richness of the core and partially engulfing shell respectively.

Pimelic Acid Mixed with Sodium Chloride.

Figure 3.4a and Figure 3.4b show the height and phase image, respectively, for a single 280 nm particle comprised of both PA and NaCl, with a partially engulfed phase separated morphology. Figure 3.4c shows the IR spectra taken at the particle's different

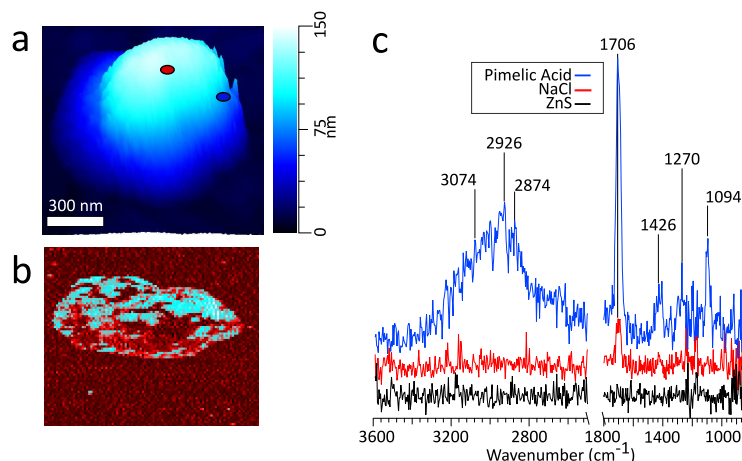


Figure 3.4: a) 3D height image of a NaCl/PA (1:1 mass ratio) particle with a volume equivalent diameter of 280 nm on ZnS substrate with markers identifying PTIR spectra locations b) Phase image c) PTIR spectra obtained for PA rich (blue), NaCl rich (red) and ZnS (black) regions at the corresponding locations marked in panel a).

phase regions and on the ZnS substrate. The blue marker/spectrum is indicative of a region rich in pimelic acid, most identifiable by the distinct carbonyl stretch (1706 cm^{-1}). The red marker/spectrum corresponds to a region rich in sodium chloride, characterized by the lack of IR active bands. The small peak at around 1700 cm^{-1} likely due to a thin coating of pimelic acid. In the particle shown, no peaks corresponding to the sodium carboxylate salt were observed. AFM and other microscopy techniques can probe the physical properties, morphology, and topography of aerosol particles, but AFM-PTIR spectroscopy adds the capability of correlating differences in physical properties or morphology with differences in chemical composition.

Pimelic Acid Mixed with Ammonium Sulfate Particles.

AS/PA particles were used to demonstrate AFM-PTIR's ability to study systems comprised of IR active inorganic salt and IR active organic compound, in contrast to the NaCl/glucose and NaCl/PA particles, which consisted of an IR inactive salt and IR active organic. Figure 3.5a shows the AFM-PTIR spectra taken at different parts a particle

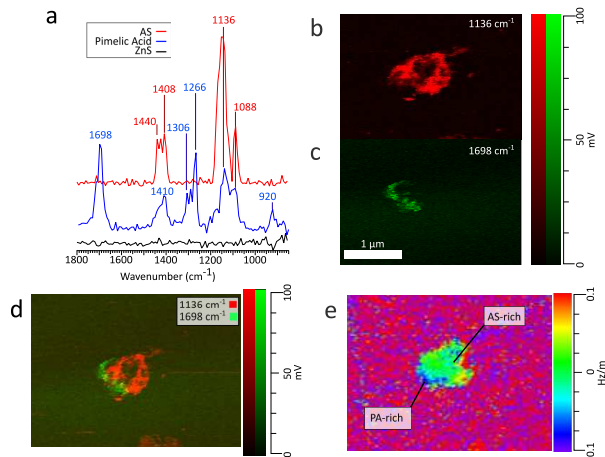


Figure 3.5: a) PTIR spectra obtained on a AS/PA particle for PA rich (blue) AS rich (red) and ZnS (black) regions at the corresponding locations marked in panel d. b) Chemical image of the particle at 1136 cm^{-1} c) Chemical image of the particle at 1698 cm^{-1} d) RGB overlay of chemical images in panels c and d. e) Ratio image of the frequency map at 1136 cm^{-1} and height.

comprised of pimelic acid and ammonium and on the ZnS substrate 280 nm away. The PA and AS particle shows two distinct IR signatures at different regions. The red spectrum corresponds to ammonium sulfate-rich regions while the blue spectrum is a region enriched with pimelic acid.

AFM-PTIR provides single wavenumber chemical maps of materials with nanometer spatial resolution by irradiating the sample with the IR source tuned to a single wavelength throughout the AFM scan. Mapping wavenumbers were selected by examining PTIR spectra for absorption frequencies exclusive or predominant for one region. The asymmetric sulfate stretch (1136 cm^{-1}) and carbonyl stretch (1696 cm^{-1}) were used to map for regions rich in pimelic acid and ammonium sulfate respectively, shown in Figure 3.5b and Figure 3.5c. The most intensely absorbing regions arise from two distinct regions within the particle. This separation is more visible with an RGB overlay of the two maps in Figure 3.5d which reveals a partially engulfed morphology. This chemical separation is consistent with cryo-TEM observations that observed phase separation between two species, but could not provide direct chemical distinction.[21] Chemical maps

provide information on the distribution of chemical species and morphological assemblies, giving chemical context to the morphological and physical properties observed in other microscopy techniques.[76]

Frequency maps are simultaneously collected with chemical maps, which plot the contact resonant frequency of the cantilever as a function of spatial position, giving insight into differences in viscoelastic properties across a single particle. The contact resonance frequency for a given oscillation mode is dependent on the sample's mechanical properties, shifting to higher values as the stiffness or viscosity of the sample increases.[76] The dependency of these shifts on the sample's mechanical properties is similar to that of phase shifts in AFM tapping mode. Figure 3.5e shows a ratio of the frequency to height images of the particle using the 1136 cm^{-1} frequency mapping. The ratio of the images was taken to show contrast the particle contact resonance frequency from the ZnS substrate. The ZnS substrate is IR transparent, so the substrate region shows no absorption features. Importantly, the collection of chemical and frequency maps is simultaneous and independent. Therefore, frequency maps can be compared directly with chemical maps to correlate chemical and mechanical properties.

3.4.3 Hygroscopic Studies: Growth Factors and Spectroscopic Signatures for Water Uptake

Extensive work has been done in measuring the water uptake of aerosol particles by using AFM to measure physical and morphological changes, such as surface tension, and growth factors. Currently, growth factors are the most straightforward metric for quantifying water uptake in AFM, where a single deposited particle is imaged at incrementally higher RH levels and the spherical diameter equivalent growth is calculated. NaCl is a well-studied system with a known deliquescence relative humidity (DRH) of $75.1 \pm 1\%$ [114] For inorganic salts such as NaCl, prior to deliquescence there is no uptake of water

vapor, and subsequently, there should be no change in particle size. Upon deliquescing, the phase changes from solid particle to aqueous droplet and should be accompanied by a significant increase in size and a corresponding decrease in viscosity. Figure 3.6a and

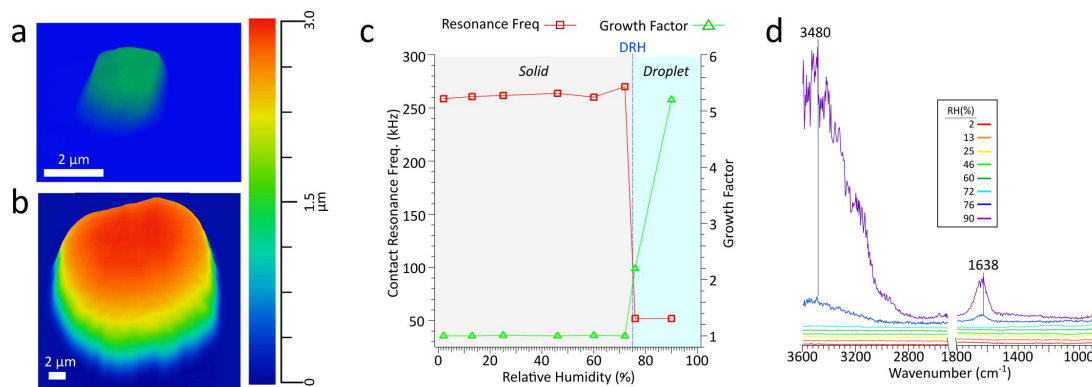


Figure 3.6: a) 3D height image of a NaCl particle with a volume equivalent diameter of $1.3 \mu\text{m}$ at 2% RH and b) the same particle now with the diameter of $6.6 \mu\text{m}$ at 90% RH c) Contact resonance frequency (red) and growth factor (green) for the $1.3 \mu\text{m}$ NaCl particle as a function of increasing RH. Above the DRH (75%) there is a sharp increase in the growth factor and decrease in the contact resonance frequency. d) PTIR spectra for the same particle as a function of increasing RH. Above the DRH, there is the growth in of two main peaks $\delta(\text{OH})$ at 1638 cm^{-1} and $\nu(\text{OH})$ at 3480 cm^{-1} , indicative of the absorbed water.

Figure 3.6b show a $1.3 \mu\text{m}$ dry volume equivalent diameter NaCl particle at 2% and 90% RH, respectively. Upon deliquescing, the particle grows in size and changes from a crystalline cubic solid to a droplet. Figure 3.6c shows the growth factor and contact resonance frequency as a function of RH. Before the DRH, there is minimal change in growth factor and contact resonance frequency. However, above the DRH, a significant increase in the growth factor (1.0 to 2.2) and a concomitant decrease in the contact resonance frequency (260 to 52 kHz), respectively, indicating that the particle has significantly increased in size and decreased in viscosity. Particle growth continues with increased water uptake at higher RH levels, the growth factor increases to 5.2. However, from 76% to 90% RH, there is no decrease in contact resonance frequency. Figure 3.6d shows the PTIR spectra taken at increasing RH. Prior to the DRH of NaCl, at 75%, there is no absorbance from the

IR inactive NaCl. Above the DRH, we observe the growth of two prominent absorbance bands at 1638 and 3480 cm^{-1} , the O-H bending and stretching modes, respectively, indicative of water absorption by the particle. In agreement with an increase in growth factor, the intensity of these two modes increases with increased water uptake at higher RH levels. Thus, we can conduct hygroscopic studies via single-particle measurements of particle size, stiffness, and chemical composition. While these results are for a supermicron sized NaCl particle, they lay the foundation for conducting similar studies in the submicron size regime, wherein, we can simultaneously observe changes in morphology, mechanical properties, and physical-chemical properties as a function of water vapor concentration.

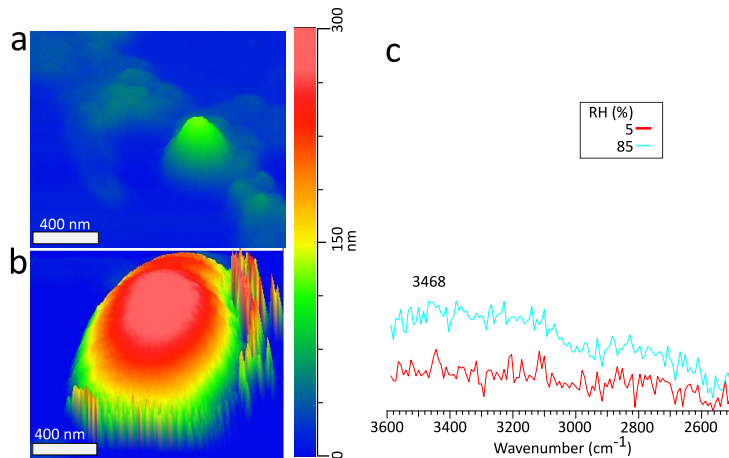


Figure 3.7: a) 3D height image a dry NaCl particle with a volume equivalent diameter of 140 nm on hydrophobic Si wafer substrate at 5%RH. b) The deliquesced particle with diameter of 390 nm at 85% RH c) PTIR spectra obtained on the particle marked in panel a) and b) at 5% RH (blue) and 85% RH (red).

To demonstrate PTIR spectra acquisition for deliquescence studies involving submicron sized particles, Figure 3.7c shows PTIR spectra taken on a sodium chloride with a 135 nm dry volume equivalent diameter at 5% (red) and 85% RH (blue), with corresponding height images in Figure 3.7a and Figure 3.7b respectively. Beyond the DRH of NaCl, we still observe the stretching (3468 cm^{-1}) modes of the absorbed water. However, the lower intensity O-H bending mode was not discernible from noise. Similar to the supermicron-

sized particle, at 85% RH we observe a 3D GF of 2.93, but no decrease in contact resonance frequency, which may occur due to the smaller particle size or contact with the substrate. The size dependence of this resonance frequency shift will be examined in more detail in future studies.

3.4.4 Sample Interactions with an IR Active Substrate

As infrared irradiation is not selective only to the aerosol particles, whenever the particle of interest is irradiated, the substrate also interacts with the incoming light. With an IR inactive substrate such as ZnS, there are no spectral deformations from the substrate absorbing IR light, but this differs when working with IR active substrates. Substrate thermal diffusivity, substrate-sample interactions, and substrate-IR radiation interactions are all potential issues that could result in particle deformations and spectral distortions. These concerns are especially important when working with an IR active substrate and increasingly smaller substrate deposited aerosol particles, which can be tens of nanometers in thickness. With smaller and subsequently thinner particles, potential interferences from the substrate absorbing IR light may arise. The thickness threshold for these interferences can be expected to vary between particles (and substrates) comprised of different chemical compositions and physical properties. As a preliminary assessment, sodium nitrate particles were deposited on a silicon wafer, SiO₂, which have a known absorbance around 1050 cm⁻¹.^[115] Sodium nitrate has a known absorbance at roughly 1360 cm⁻¹,^[116] and was chosen due to the absence of any vibrational modes near 1100 cm⁻¹, making the presence of any substrate absorbances noticeably apparent. For a reference, Figure 3.8a shows the PTIR spectra of NaNO₃ in red and the substrate in black and Figure 3.8b shows the PTIR spectra for particles of varying thickness. Below 200 nm thickness, there is a clear absorbance band from the substrate at 1100 cm⁻¹. While these impacts may be negligible for larger particles, when probing smaller particles, interference from an IR active substrate

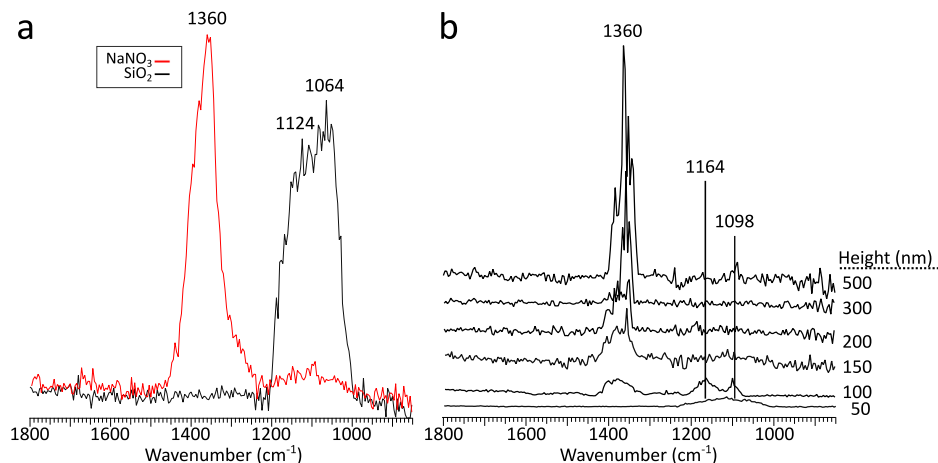


Figure 3.8: a) PTIR spectra obtained on a NaNO₃ particle (red) and silicon substrate (black), b) PTIR spectra taken for NaNO₃ particles of varying height from 500 to 50 nm

can produce noticeable spectral defects via substrate absorbance modes. In the 100 nm thick particle, the intensity of substrate and particle modes are comparable. Interestingly, in the 50 nm thick particle, no signatures from the particle were detectable. These defects were avoided in this study due to use of one (or a combination) of the following - an IR transparent substrate (ZnS), particle thickness much greater than 200 nm, or irradiating in spectral regions excluding the substrate absorption modes.

3.4.5 Tapping and Resonance Enhanced AFM-PTIR

One of the major disadvantages of using AFM-PTIR for aerosol analyses is the need for an expansion force, which is dependent on underlying material stiffness. For AFM-PTIR with lower repetition lasers such as an OPO, signal is extracted from a single expansion and displacement of a probe held in contact, followed by a ring-down decay relaxation. For aerosol particles that are either contain organics or are entirely comprised of organics, these regions are often low in aspect ratio, resulting in thin cross sections. Thus, under traditional contact AFM-PTIR, these conditions make it difficult to analyze and extract signal due to expected extremely low expansion forces. Additionally, when

collecting chemical maps, using an OPO source conventionally requires AFM to operate under contact imaging mode. For softer organics, the higher shear forces can destructively perturb the particle, resulting in material displacement and imaging artifacts.

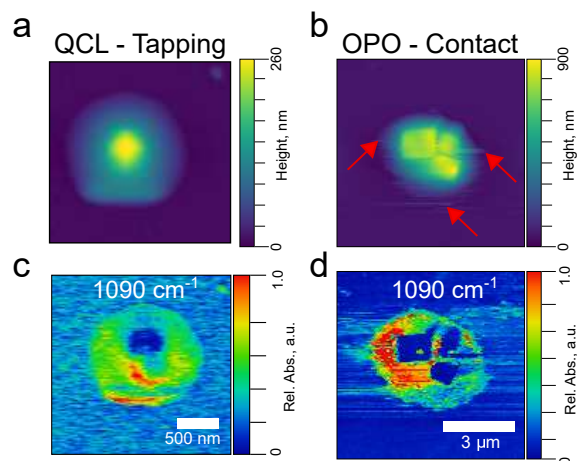


Figure 3.9: AFM height images of 1:1 mixed NaCl:Glucose particles collected in a) tapping mode with a QCL source and b) contact mode with an OPO source with corresponding maps collected at 1090 cm^{-1} are shown in panels c) and d) respectively. Distinct artifacts from the probe tearing into the organic shell of particle are seen in the OPO chemical map, and examples are indicated by the arrows in the height image in panel b)

Recent advancements in AFM-PTIR technology involved integration of tunable higher repetition rate lasers, leading to the development of tapping AFM-PTIR and resonance enhanced AFM-PTIR, assist in imaging during chemical maps and higher sensitivity respectively. Briefly, in tapping AFM-PTIR, cantilever deflection is no longer being measured for IR absorbance. Rather, the particle is irradiated by the IR source at a rate ω_s , and upon absorbance, this frequency of expansion interacts with a cantilever oscillating typically at its fundamental eigenmode ω_1 . Heterodyne mixing between the two frequencies results in excitement of a higher harmonic modes of the cantilever ω_n , and measuring the resulting response generated at ω_n allows for measuring IR absorbance spatially localized to the AFM cantilever, while remaining in oscillatory motion. This facilitates chemical imaging whilst still remaining in intermittent contact operation, reducing shear forces on

the sample, which is ideal for organic richer samples, as demonstrated by the chemical maps of mixed NaCl:glucose particles shown in Figure 3.9. In the height image (Figure 3.9b) and chemical map (3.9d) collected by the OPO in contact mode imaging, distinct tear artifacts are seen in the height image due to the softer organic coating. In contrast, the the height image (Figure 3.9a) and chemical map (3.9c) of a particle collected with the QCL in tapping mode is more accurately imaged with no presence tear artifacts. AFM-PTIR analyses of systems with softer samples benefit from the lower tip-sample interaction forces using tapping mode to collect chemical maps.

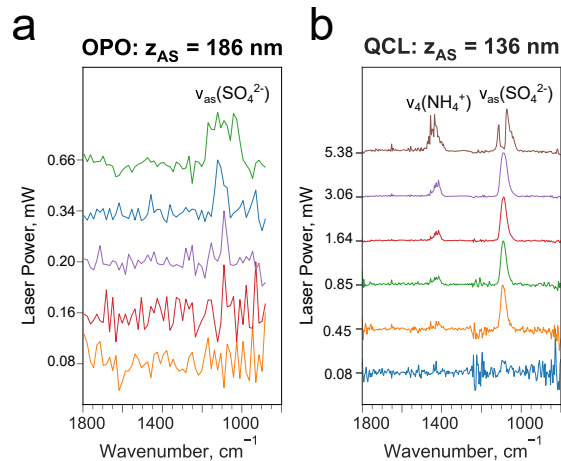


Figure 3.10: PTIR spectra collected from ammonium sulfate (AS) particles using a) standard contact AFM-PTIR with an OPO laser source and b) resonance enhanced AFM-PTIR with a QCL laser source at varying laser powers. Spectral artifacts are observed with the QCL laser at 5.38 mW.

An additional benefit of tunable frequency IR laser sources is the ability to match the laser repetition rate to frequency of a cantilever coupled to the sample surface, ω_c . Under these conditions, the cantilever response is no longer represented by a single expansion and ringdown decay, but rather held in sustained harmonic motion, wherein the particle expansion and relaxation is matched to the oscillatory motion of the tip. This results in higher signal to noise [76]. Demonstration of resonance enhanced AFM-PTIR is shown in Figure 3.10, comparing the response that the two laser sources produce from similar cross

section heights of AS particles. Comparisons are conducted with the exact same cantilever to remove any variability from probe mechanical properties. The IR spectra using a 1 kHz OPO source at varying laser powers is shown in 3.10a and the spectra from the QCL tuned to a pulse frequency equal to ω_c (277 kHz). High laser power spectral artifacts are still apparent with the QCL, as indicated by the splitting of the $\nu_{as}(\text{SO}_4^{2-})$ mode at 5.38 mW. However, at comparable laser powers, the spectral features of AS are much more clearly resolved under resonance enhancement even though the OPO spectra was collected from a 50 nm thicker particle.

3.5 Conclusions

This study demonstrates AFM-PTIR spectroscopy to simultaneously measure the physicochemical and morphological properties of sub- and supermicron individual aerosol particles. The spectral information provided via single-particle AFM-PTIR spectroscopy is in a reasonably good agreement with traditional methods such as bulk FTIR. Moreover, we show that AFM-PTIR spectroscopy is a useful method to study multicomponent aerosol particles via chemical and frequency maps that provide high spatial resolution information on the spatial distribution of chemical species and their subsequent mechanical properties. We also show the chemical characterization of aerosol particles as small as 50 nm in diameter, as well as larger particles above 2.5 μm in diameter. The nanoscale resolution of AFM-PTIR allows us to study not only submicron sized particles interacting with water vapor but also interactions between water vapor and different regions within a single particle, which is vital for linking chemical composition to hygroscopic properties that describe the ability for an aerosol particle to act as effective CCN. Future hygroscopic studies with AFM-PTIR will focus on examining localized changes within a single multicomponent aerosol particle, wherein we can compare the behaviour of different components

in response to reactive gas uptake and water vapor.

3.6 Acknowledgements

Chapter 3, in part, is a reprint of the material published by The Royal Society of Chemistry in: **Victor W Or**, Armando D Estillore, Alexei V Tivanski, Vicki H Grassian. Lab on a Tip: Atomic Force Microscopy - Photothermal Infrared Spectroscopy of Atmospherically Relevant Organic/Inorganic Aerosol Particles in the Nanometer to Micrometer Size Range. *Analyst*, 143(12), 2018. The dissertation author was the co-first author of this paper. This work was supported by the National Science Foundation through the Centers of Chemical Innovation Program under Grant CHE1305427.

3.7 Supporting Information

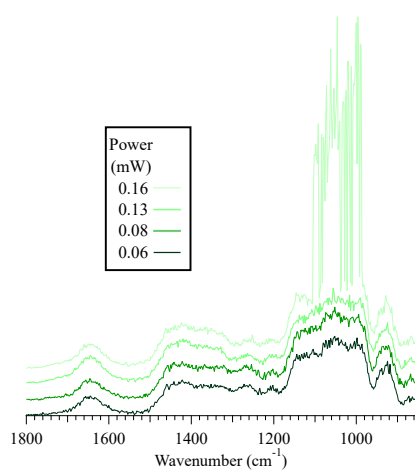


Figure S3.1: PTIR spectra taken on a sucrose particle with increasing laser power from 0.06 to 0.16 mW. Particle damage is spectrally apparent at 0.16 mW, as seen by the growth of irregular shaped peaks between 980 to 1100 cm⁻¹

Chapter 4

Influence of Size, Biological Activity, and Heterogeneous Aging on Morphology and Composition of Marine Sea Spray Aerosols

4.1 Abstract

The impact of sea spray aerosol (SSA) on Earth's climate remains uncertain in part due to size-dependent particle-to-particle variability in SSA composition and physico-chemical properties such as morphology, phase state, and hygroscopicity. These properties are probed on a single particle basis as a function of particle size from 0.1 - 0.6 μm collected throughout a phytoplankton bloom. Atomic force microscopy (AFM), and AFM photothermal infrared spectroscopy (AFM-PTIR) were utilized to correlate composition to morphology. AFM imaging at 20% RH identified main nascent and heterogeneously aged SSA morphologies: prism-like, core-shell (prism), core-shell (rod), rounded, rod, and

aggregate, and AFM-PTIR analyses linked morphologies back to known laboratory mimic compounds.

4.2 Introduction

The ocean covers approximately 70% of the earth's surface and is one of the largest source of biogenic aerosol emissions.[30, 15] However, the ocean is extremely diverse, with varying degrees of biological activity [117, 118] and anthropogenic influences.[119, 120, 121, 122] Depending on the production mechanism, composition of aerosol particles produced in marine environments varies; wave-breaking produces larger supermicron sized particles enriched with inorganic compounds and water soluble organics while jet drops produces aliphatic organic enriched submicronic particles. [1, 33] Oxidative aging transforms marine volatile organic compound emissions into secondary marine aerosols (SMA)[123], and can alter the composition of primary nascent sea spray aerosol (SSA)[53], subsequently altering their influences larger scale climate processes like cloud formation. Thus, understanding the physiochemical nature of primary SSA and their evolution with chemical aging is crucial to predicting large scale climate processes.

Aerosols are one of the largest sources of uncertainty in climate modeling and predictions, in large part due to their influences on Earth's radiative budget.[18] Aerosols can directly scatter incoming solar radiation, and indirectly play a crucial role in cloud formation and precipitation by acting as nucleators for cloud droplet and ice formation. The ability for an aerosol to influence these processes depends on various physiochemical properties including size, morphology, and chemical composition.[17, 124, 80] However, aerosols extremely complex in all of these facets, spanning multiple orders of magnitude in size, and chemically and morphologically diverse reflective of production source, mechanisms, and transformations.[37, 35, 19, 86]

Because many of these properties are dependent on size, composition, and distribution of species within a single particle, recent efforts have been focused on more detailed analyses of the evolution of morphological and physiochemical properties of single particles across varying conditions such as microbial blooms. Past microscopic studies have shown that during a microbial bloom, the distribution of nascent sea spray aerosol (SSA) particle morphologies shift as a function of size and relative organic abundances within particles evolves as function of biological activity.[86, 35, 1]

Adding to this complexity, within a single SSA particle, chemical heterogeneities have been observed. For example in systems comprised of inorganic - organic compounds, depending on the particle size phase separation can be observed through varying degrees of organic engulfment of the inorganic particle core.[19, 21] In organic-organic system, species can partition into different regions of the particle, resulting in liquid-liquid phase separations.[41, 125] Aerosol morphology influences how particles interact with water, subsequently altering their ability to act as cloud seeds or ice nuclei.[19, 126, 47] In addition, aerosol morphology and phase state vary with water vapor and temperature.[127, 128] Thus, understanding the composition, physiochemical properties, and morphology of SSA are necessary for improving our understanding of the larger climate scale processes they partake in. Additionally, accurately understanding aerosol involves understanding their fates as they undergo chemical transformations their atmospheric lifetime. Thus, there is a need for measurements of key properties such as morphology and composition, as aerosols evolve throughout their atmospheric lifetimes.

These complexities highlights the need for chemical and physical analyses on size scales relevant to capturing these heterogeneous facets. High resolution from microscopy has been used to give insight into morphology and physiochemical properties such as surface tension, phase-state, and viscosity on a single particle basis, and in some studies, sub-particle basis across phase separated regions. In this paper, morphology and compo-

sition explored using AFM based techniques. AFM imaging provides insight on particle morphology. However, the additional information from AFM-IR spectroscopy provides insight into chemical composition within and between particles. Spectra from authentic SSA are compared back to model system versions of compounds previously identified in SSA, such as complex sugars. Spectroscopic results reveal that organic rich particles are those that exhibit core-shell morphologies and rounded shaped particles. Due to the overwhelming complexity of these species, in the absence of complementary size-resolved structural characterization, spectroscopic analyses of authentic SSA are aided by comparison with reference spectra back to single compound systems commonly used as model surrogates for studies.

4.3 Methods

4.3.1 Sea Spray Aerosol Generation and MOUDI Sampling

SSA were generated from a wave-simulation channel containing filtered Pacific Ocean seawater from the southern coast of California during the Sea Spray Chemistry And Particle Evolution (SeaSCAPE) 2019 study[129], wherein samples were collected from a phytoplankton bloom that occurred from July 25th to August 14th. Additional detail of the wave flume experiment and SSA generation during the SeaSCAPE study can be found in elsewhere.[129] A schematic of the sampling lines are shown in Figure S4.1. The nascent SSA samples were collected during July 26/27th (pre-bloom), August 2nd (peak-bloom), and August 6th (post-bloom) dates. Nascent SSA was collected by directly sampling flume headspace and impacting onto substrates in a MOUDI (MOUDI-110, TSI). Samples were collected under ambient temperature (25 - 30 °C) and 70-90% RH.

Heterogeneously aged SSA (hSSA) was collected by flowing flume head space through an oxidation flow reactor (OFR, PAM-OFR, Aerodyne Inc) (25 - 30 °C). For heteroge-

neously aged SSA, samples were collected during August 2nd (peak-bloom). The particles and gases in the flume head space reacted with 5 days equivalent of hydroxyl radical and was passed through two diffusion dryers filled with ozone scrubbers (CARULITE-200, Carus) to remove ozone prior to deposition. This flow was then mixed with a bypass of liquid nitrogen before impacting onto substrates using a MOUDI (nanoMOUDI-II 125R, TSI). Due to the liquid nitrogen bypass, samples were collected under drier conditions, at 15-20% RH. In both sampling lines, MOUDI stages 7, 8, and 9 were used, corresponding to aerodynamic diameter ranges of 0.32 - 0.56 μm , 0.18 - 0.32 μm , and 0.10 - 0.18 μm , respectively.⁵⁵ Substrates were immediately placed in cleaned sealed petri dishes and stored in the dark under ambient temperature, humidity, and pressure.

4.3.2 Model System Preparation

All chemicals used were purchased directly from the manufacturers, utilized without further purification, and included docosane (>99%, Fischer Scientific), sodium nitrate ($\geq 99\%$, Fischer Scientific), sodium sulfate ($\geq 99\%$, Fischer Scientific), sucrose ($\geq 99.0\%$, Sigma-Aldrich), sodium alginate ($\geq 99\%$, Sigma-Aldrich), pimelic acid ($\geq 99.0\%$, Sigma-Aldrich), lipopolysaccharide (L4130, Sigma-Aldrich). Single component aerosol particles were generated from a 0.5 or 1% wt/v aqueous solution using ultrapure water prepared on site (Barnsted EasyPure- II; $\geq 18.2 \text{ M}\Omega \text{ cm}$ resistivity, Thermo). The aerosol particles were then sent through two diffusion dryers (model 3062, TSI) at a flow rate of 1.5 lpm to reduce the RH to ca. 5% RH. Si wafer sampling substrates (16008, Ted Pella) were used to collect the aerosol particles by mounting the substrate in front of an electrostatic classifier (TSI Inc., model 3080) for 1-10 min.

4.3.3 AFM

AFM based single particle morphology and organic volume fraction measurements. A molecular force probe 3D AFM (Asylum Research, Santa Barbara, CA) was used for imaging substrate-deposited individual SSA at 20% RH and ambient temperature (20 - 25°C).² Single particle imaging was performed in completely random and unbiased manner. Using AFM measured volume equivalent diameters, deposited SSA particles were sorted into size bins 0.32 - 0.56 μm , 0.18 - 0.32 μm , and 0.10 - 0.18 μm . Silicon nitride AFM tips (MikroMasch, model CSC37, typical tip radius of curvature 10 nm, nominal spring constant 0.5 - 0.9 N/m) were used for imaging.² AFM AC mode imaging was used to collect height and phase images of individual SSA to determine their morphology, and relative abundances of each morphology category were recorded across the bloom for particles with three selected volume-equivalent diameter ranges of 0.10 - 0.18, 0.18 - 0.32 and 0.32 - 0.60 μm .

4.3.4 AFM-IR Spectroscopy

AFM-IR spectroscopy measurements were conducted using a commercial nanoIR² (Bruker, Santa Barbara, CA) microscope equipped with a tunable mid-IR quantum cascade laser (QCL) and a tunable mid-IR optical parametric oscillator laser (OPO). Experiments were performed at 20% RH and ambient temperature (23-26 C) on SSA samples collected on MOUDI stages 7, 8, and 9 during July 26th (pre-bloom) and August 2nd (peak-bloom). AFM height images were collected in tapping mode at a scan rate of 0.5 Hz using silicon nitride probes with a chromium-gold coating (HQNSC19/CR-AU, MikroMasch, typical tip radius of curvature 35 nm, and a nominal spring constant range of 0.05 - 2.3 N/m). AFM-PTIR spectra were collected at a preselected tip-localized position across the sample surface with a nominal spatial resolution below 35 nm and a spectral resolution of 8

cm⁻¹ (OPO) and 5 cm⁻¹ (QCL), while co-averaging over 128 laser pulses. To account for a possible substrate AFM-PTIR signal contribution, a reference spectrum was taken on the substrate and subtracted from all corresponding spectra obtained on individual particles. Approximately 10 individual SSA with core-shell and rounded morphologies were investigated. For core-shell SSA, spectra were taken at the core and shell particle regions, while for the rounded SSA spectra were taken at an approximate center of the particle.

4.4 Results and Discussion

4.4.1 Nascent Sea Spray Aerosols

Morphology

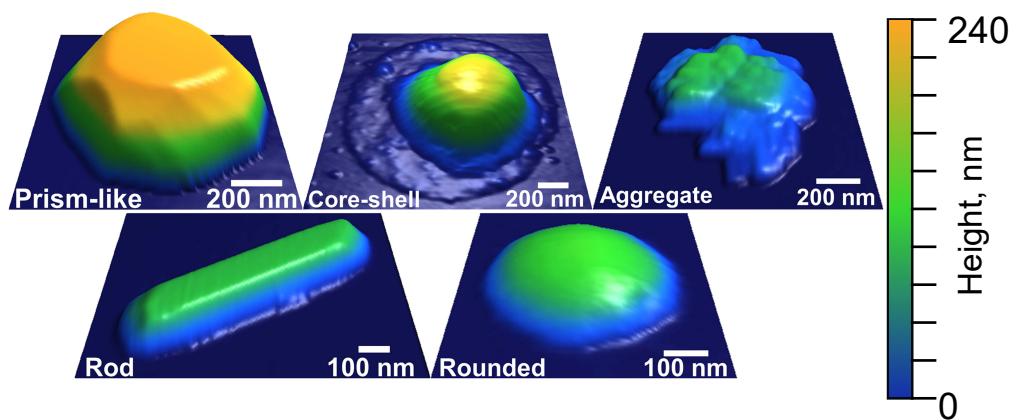


Figure 4.1: Selected illustrative AFM 3D-height images of five main morphological categories (prism-like, core-shell, rounded, rod, and aggregate) identified for nascent SSA. Images provided from Chathuri Kaluarachchi from Professor Alexei Tivanski’s group.

Figure 4.1 shows representative AFM images of the five main morphology classes observed: 1) prism-like where the particle was primarily comprised of an inorganic crystal, relatively tall and cubic-like in structure, 2) core-shell where an inorganic core is sur-

rounded by a flatter organic shell, 3) rounded particles, which were relatively flat circular particles, 4) rod structured with an elongated major axis and 5) aggregates which were irregularly shaped clusters of multiple morphologies. The presence of these five morphologies is largely consistent with a past mesocosm study, with the exception of a rod-inclusion morphology which is included under aggregates. Lee et al. 2020[130] found that the relative abundance of each morphology shifts with particle size, and subsequently, organic enrichment in smaller size ranges correlated with enhancements of core-shell and rounded particles. Size dependence in organic enrichment is consistent across multiple mesocosm studies. However, there lacks insight into how SSA morphology distributions shift as a result of progressive changes in microbial activity or subsequent chemical transformations

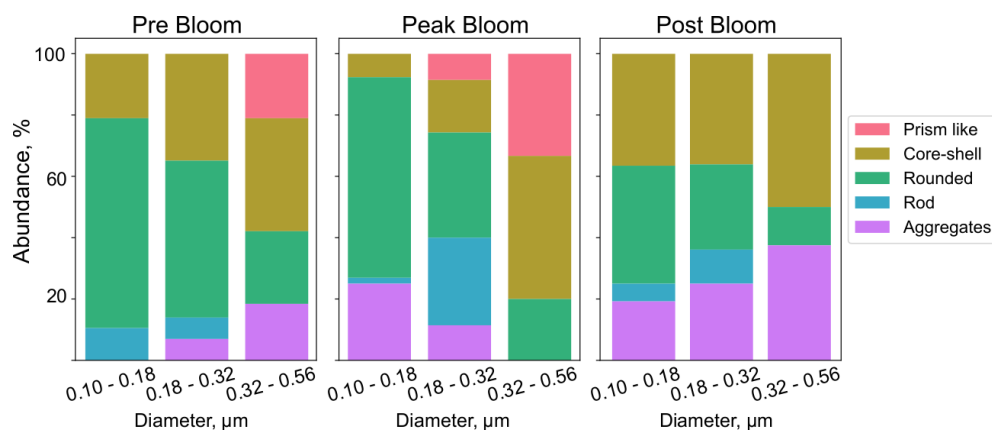


Figure 4.2: Stacked bar plots of morphology distribution for nascent SSA produced during different dates of the bloom: pre-(left), peak-(middle) and post-bloom(right). Particles are separated into size bins according to their volume equivalent diameter. Data is provided from Chathuri Kaluarachchi from Professor Alexei Tivanski’s group.

The relative morphology distribution of nascent produced SSA particles throughout a microbial bloom is shown in Figure 4.2, with stacked bar graphs for three size bins across three separate key dates. Pre-bloom corresponding to the beginning of the mesocosm and lowest level of microbial activity, peak bloom with the highest level of biological activity measured by Chlorophyll-a, and post-bloom corresponding to the grazing phase of the bloom corresponding to the highest level of heterotrophic bacteria counts. Within each

date, SSA particles were size separated into bins based on volume equivalent diameter: 0.10 - 0.18, 0.18 - 0.32 and 0.32 - 0.60 μm .

From the pre-bloom, particles between 0.10 - 0.18 μm were predominantly rounded in morphology, with a small contribution of rods and core-shell particles, and no prisms or aggregates were measured. Increasing particle diameter to 0.18 - 0.32 μm , the particles were largely rounded and core-shell morphologies, with relatively fewer rounded particles. A small number of rods and aggregates were detected but still no prism shaped particles. In largest size bin, 0.32 - 0.60 μm , we observe a decrease in the fraction of rounded particles, and a corresponding increase of prism particles, while the fraction of core-shell particles remained fairly consistent. No rods were observed, but more aggregates are present. During this period of lower biological activity, generally observed that rounded and rod shaped particles decrease with size, while aggregates increase. Prisms, which are presumed to be inorganic rich, are only observed in largest size range. At the peak-bloom, distributions of rounded and core-shell particles follow similar size dependent to the pre-bloom, where rounded morphologies are less abundant with increasing size but core-shell particles increase in abundance. Prisms behaved in a similar manner to core-shell, wherein they were not detected in the smallest sized particles, and showed the highest abundance in the largest size bin. In contrast, the aggregates and rods trend conversely with size, where rods were the most frequent in the 0.18 - 0.32 μm particles while aggregates were the most abundant in the smallest size bin 0.10 - 0.18 μm .

Particles produced during the post-bloom were 0.10 - 0.18 μm : no prisms, largely rounded and core-shell morphologies. Aggregates were present, followed by a small amount of rods. 0.18 - 0.32 μm : increased abundance of aggregates and rods, lesser number of rounded particles observed. 0.32 - 0.60 μm : slight increase in core-shell particles observed, and aggregates increased, rods no longer observed, and rounded decreased. General Trends: Highest abundance of core-shell and aggregates. Aggregates increase with size, while

rounded decrease. As particle size increases, the fraction of rounded particles observed decreases. Core shell particles increase with size. In contrast, prism morphology particles are only observed in the larger size ranges. Rods were only observed in smallest size while aggregates present in all 3, with no clear trend between all 3 dates. Trends within, rounded decrease across bloom, morphologies like aggregates rods show no trend between dates. The relative increase in inorganic rich prism morphology with larger particle sizes is likely tied back to the production sources and mechanisms. Larger supermicron sized particles typically arise from wave-breaking jet droplets, enriched in inorganic species welled up from the underlying bulk seawater. In contrast, smaller sized particles come from film drops due to bubble bursting at the sea surface microlayer, subsequently resulting in an enrichment in hydrophobic organic species. [1, 35]

Composition

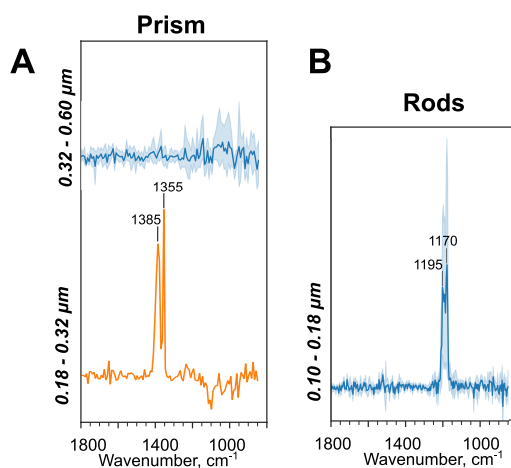


Figure 4.3: PTIR spectra taken for (A) prism and (B) rod SSA measured using AFM-IR. Spectra are divided into at three selected volume-equivalent diameter ranges of 0.1 - 0.18, 0.18 - 0.32 and 0.32 - 0.60 μm . Due to lower abundance and IR activity for these morphologies, no comparison is provided between bloom dates, and only certain size ranges were found in analyses. Solid lines show the average spectra for a given class, with shaded lines representing the 95% confidence interval.

The AFM-PTIR spectra collected for prism-like and rod particles are shown in Fig-

ure 4.3. Rods were only analyzed within the smallest size ($0.10 - 0.18 \mu\text{m}$) and the spectra are characterized by a single sharp peak around 1170 cm^{-1} associated with $\nu_{as}(\text{SO}_4^{2-})$ from inorganic sulfates (Figure S4.2B).[131] The larger size ($0.32\text{-}0.60 \mu\text{m}$) prism-like particles are IR inactive as detected by AFM-PTIR spectroscopy. However, in smaller prism-like particles ($0.18 - 0.32 \mu\text{m}$), there is evidence for nitrates, due to sharp peaks around $1355, 1380 \text{ cm}^{-1}$, that overlap well with measured nitrate spectra (Figure S4.2B), and the asymmetric nitrate stretching motion $\nu(\text{NO}_3^-)$. [132, 131] These spectral features correspond well to their corresponding sodium salts, as shown in Figure S4.2B. The prism-like morphology particles thus are expected to be relatively low in organic content as detected by AFM-PTIR spectroscopy.

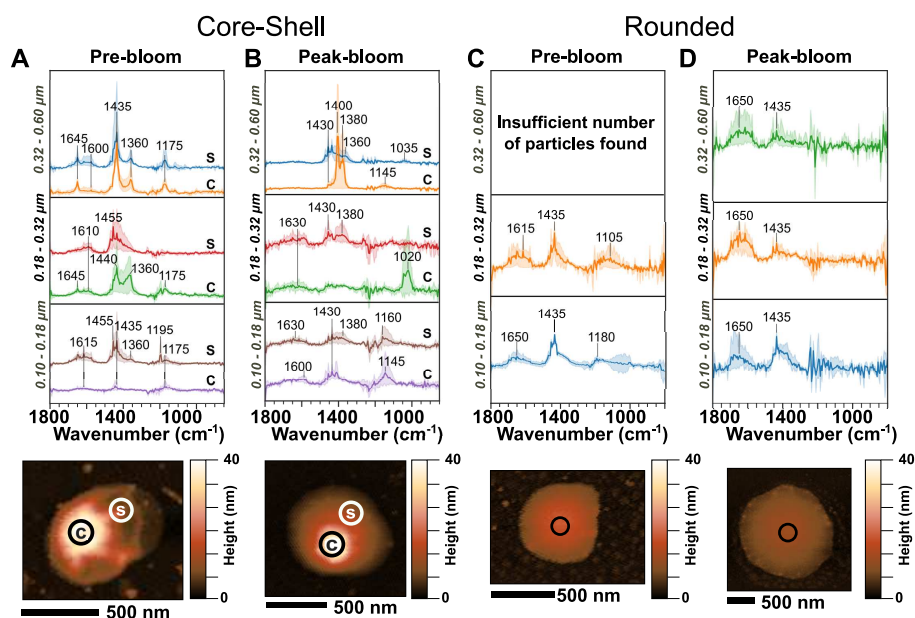


Figure 4.4: PTIR spectra and representative AFM height images for core-shell and rounded SSA measured using AFM-IR for (A), (C) pre-bloom and (B), (D) peak-bloom days. SSA spectra are divided into three selected volume-equivalent diameter ranges of $0.1 - 0.18 \mu\text{m}$, $0.18 - 0.32 \mu\text{m}$ and $0.32 - 0.60 \mu\text{m}$. For core-shell SSA, spectra were taken at two positions: in the core (c) and shell (s). For rounded SSA, spectra were taken at the approximate center of each particle. Solid lines show the average spectra for a particular morphology/particle region and shaded lines representing the 95% confidence interval.

Figure 6 shows the AFM-PTIR spectra taken on core-shell and rounded SSA for

volume-equivalent diameter ranges of 0.10-0.18 μm , 0.18-0.32 μm and 0.32-0.60 μm during pre-bloom and peak-bloom. Due to the small volume of material contained in each particle and relatively low signal associated with softer organics, resulting AFM-PTIR modes associated with organics in these particles are broad and low in intensity. The most common organic functional groups associated with spectral features observed are absorbances around: 1000 – 1200 cm^{-1} which is related to the stretching motion associated with carbon-carbon and carbon-oxygen bonds, $\nu(\text{C-C})$ or $\nu(\text{C-O})$; 1350 – 1450 cm^{-1} which can be associated with CH_2 and CH_3 bending modes in organic compounds, $\delta(\text{CH}_2, \text{CH}_3)$ or symmetric carboxylate stretches, $\nu_s(\text{COO}^-)$; and 1550 – 1750 cm^{-1} which can be associated with unsaturated carbon-carbon double bonds, $\nu(\text{C=C})$, carbonyl stretches, $\nu(\text{C=O})$, or asymmetric carboxylate stretches $\nu_{as}(\text{COO}^-)$. [133, 134, 135, 136]

Figure 4.4A shows the PTIR spectra for pre-bloom core-shell SSA. The particle shells spectra display no major spectral differences as a function of size within the studied size range of 0.10 – 0.60 μm . The spectral signatures are similar to complex sugars such as lipopolysaccharide and sodium alginate (Figure S4.2A). The presence of these sugars is consistent with prior studies performed on nascent SSA. [86, 137, 138, 139] The core of the 0.18 – 0.32 and 0.32 – 0.60 μm sized particles are spectrally similar to the corresponding shells, suggesting organic coatings extend onto the core surface of the particle. However, in the smaller sized SSA, 0.10 - 0.18 μm , the core is seen to be nearly IR inactive, likely implying absence of the organic coating on the core or a very thin coating.

Spectra of peak-bloom core-shell SSA are shown in Figure 4.4B. Shells of the 0.10 – 0.18 and 0.18 – 0.32 μm sized particles are spectrally similar to those observed in the pre-bloom, again suggesting these shells are largely comprised of complex sugars. Similar features are observed in the 0.10 - 0.18 μm size SSA cores suggesting the presence of organic coatings, while the 0.18 - 0.32 μm SSA cores contain a single peak around 1020 cm^{-1} , potentially associated with the presence of a thin coating of simple sugars (e.g.,

sucrose Figure S2A), but accurate assignment is difficult due to relatively low absorbance in the higher wavenumber modes. The larger 0.32 – 0.60 μm sized particles from peak-bloom are more spectrally distinct. From the shell, there are absorbances around 1300 – 1450 cm^{-1} with no detectible peaks at 1550-1700 cm^{-1} , and are spectrally similar to long chain n-alkanes such as docosane (Figure S2B).[86, 140] The same spectral features are also present on the particle core, suggesting similar n-alkanes organic coatings as in the shell, in addition to an intense sharp peak at 1380 cm^{-1} , potentially due to nitrates.[132, 141, 142]

PTIR spectra for rounded SSA are shown in Figure 4.4C, D, where similar vibrational modes and peak shapes associated with complex sugars (Figure S4.2A) are observed across all size ranges, most notably two broad peaks centered around 1615 – 1650 cm^{-1} and 1435 cm^{-1} . Slight differences are seen in the peak ratios between pre-bloom and peak-bloom spectra, where peak-bloom rounded SSA exhibit a larger mode around 1550 – 1700 cm^{-1} relative to the $\delta(\text{CH}_2, \text{CH}_3)$ mode around 1435 cm^{-1} , suggesting a higher degree of unsaturation or oxygen content relative to pre-bloom rounded SSA.[133, 136]

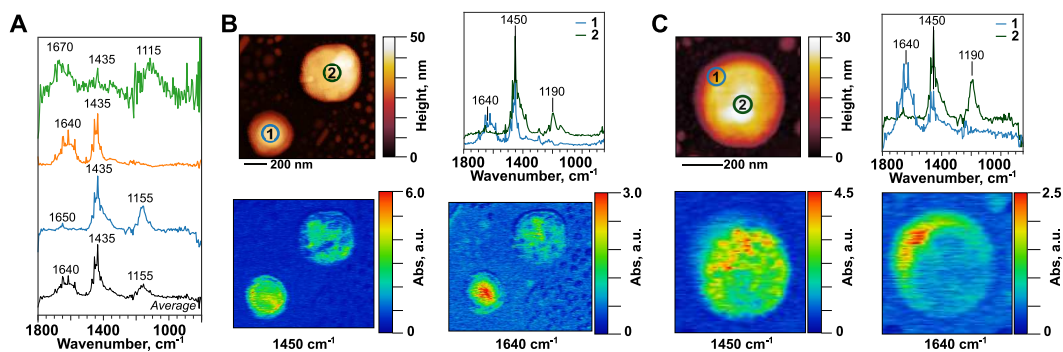


Figure 4.5: A) PTIR spectra for rounded SSA particles, each with 180 nm equivalent diameter, and their average spectrum (black). AFM height images, PTIR spectra, and chemical maps taken at 1450 and 1640 cm^{-1} for rounded SSA that showed (B) two different spectrally homogeneous particles and (C) a spectrally heterogeneous particle. Spectra taken at positions 1 and 2 are shown by blue and green colors, respectively. All particles shown were collected from the pre-bloom date.

Particle-to-particle chemical variability is demonstrated in Figure 4.5A, where PTIR spectra were taken on three different rounded particles, each with the same volume equiv-

alent diameter of $0.18 \mu\text{m}$. Rounded particles shown in Figure 4.5B exhibit external phase mixing, wherein particles are more homogeneously mixed, and absorbance from chemical maps correlates with particle height. Shown in Figure 4.5C is an internally mixed particle with no distinct morphological phase separation, one region of the particle is more absorbing around 1640 cm^{-1} due to complex sugars and may suggest chemical heterogeneity and some phase separation within these small organic particles. The AFM-PTIR measurements showed that core-shell and rounded SSA are primarily enriched with organic components such as lipopolysaccharide and sodium alginate, while prism-like and rod morphologies were predominantly inorganic salts with relatively low organic content.

4.4.2 Influence of Aging

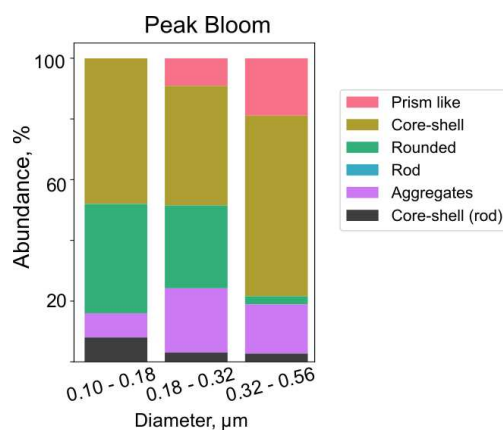


Figure 4.6: Stacked bar plots of morphology distribution for heterogeneously aged SSA produced during the peak-bloom. Particles are separated into size bins according to their volume equivalent diameter. Data is provided from Chathuri Kaluarachchi from Professor Alexei Tivanski’s group.

To better understand the influence of heterogeneous aging, particles from the peak of the microbial bloom were analyzed for changes in morphology and composition. The morphological distribution is shown in Figure 4.6. Upon reacting with hydroxyl radical, the relative morphology distribution changes. Rods are no longer observed, but rather appear as aggregates or inclusions. Across all size ranges there was an enhancement of

aggregates, most notable in the larger size ranges. Relative to the nascent distribution, the relative number of particles that had a prism morphology was consistent. Rods were not observed in the particles across any of the sizes analyzed. However, aggregates are more prevalent in the larger sized particles. Rounded particles were slightly less abundant in all size ranges, but the overall trend followed similarly - decreasing size lowered relative fraction of rounded particles.

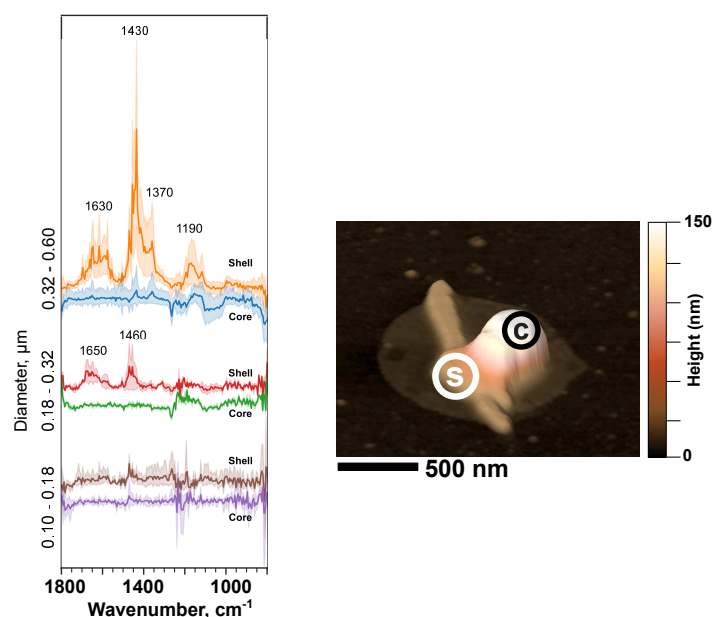


Figure 4.7: PTIR spectra and representative 3D AFM height images for core-shell heterogeneously aged SSA measured using AFM-IR for peak-bloom days. SSA spectra are divided into three selected volume-equivalent diameter ranges of 0.1 - 0.18 μm , 0.18 - 0.32 μm and 0.32 - 0.60 μm . For core-shell SSA, spectra were taken at two positions: in the core (c) and shell (s). Solid lines show the average spectra for a particular morphology/particle region and shaded lines representing the 95% confidence interval.

Spectral analyses, shown in Figure 4.7, were largely focused on comparing core-shell particles, which were expected to be organic rich and comprised the largest fraction across most size ranges. For core-shell particles collected during the peak-bloom, in the smallest particles from 0.10 to 0.18 μm , there was insufficient signal to discern any absorbance modes. However, from 0.18 - 0.32 μm , the core is IR inactive, while in the shell, we observe the same organic-associated modes similar to alginate. In the largest size range

analyzed, 0.32 - 0.60 μm , the core is entirely IR inactive, while the shell appears more oxygenated in comparison to the n-alkane-like spectra observed in the nascent shells, as indicated by the larger vibrational mode around 1600 cm^{-1} . Sufficient rounded particles of larger sizes could not be identified.

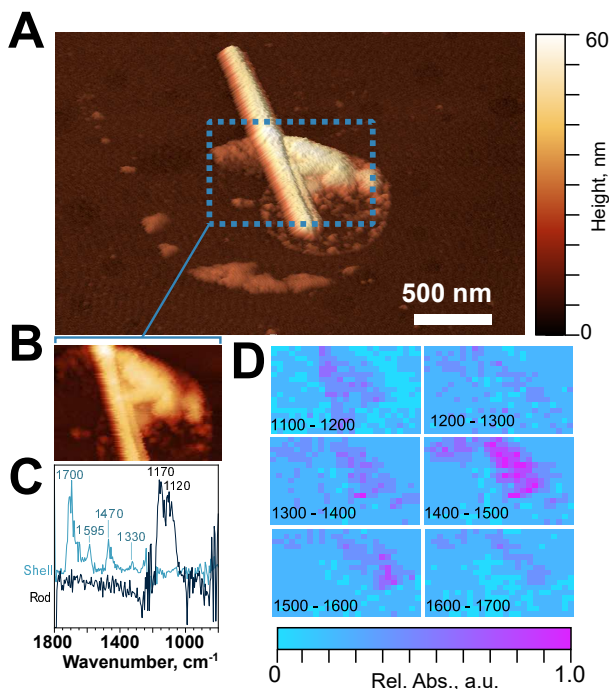


Figure 4.8: A) 3D AFM height image of a core-shell particle with a rod core B) zoomed in region of the rod and shell C) PTIR spectra of the rod and shell in black and cyan respectively D) hyperspectral maps of 100 cm^{-1} windows for the zoomed-in region shown in panel B.

Figure 4.8A shows the morphology of a core-shell particle with a rod-shaped core. There is a distinct rod with a slightly irregular shaped shell encasing part of it. IR spectra taken on the rod and shell shown in Figure 4.8C reveal that the rod is sulfate, as evidenced by the $\nu_{as}(\text{SO}_4^{2-})$ mode at 1170 cm^{-1} . The shell, as expected, is organic rich, with a distinct 1700 cm^{-1} mode from $\nu(\text{C}=\text{O})$. Hyperspectral maps of the particle show in Figure 4.8D show the spatial distribution of absorbances in 100 cm^{-1} integrated spectral bins. The sulfate vibrational modes within 1100 - 1200 cm^{-1} are largely concentrated in the rod of the particle, while shell is more intensely absorbing in maps for other spectral regions such

as $\delta(\text{CH}_2, \text{CH}_3)$, $\nu_{as,s}(\text{COO}^-)$, and $\nu(\text{C}=\text{O})$. However, accurately assigning these peaks to vibrational modes is not confidently possible due to the low signal generated from these thin organic sections of the particle.

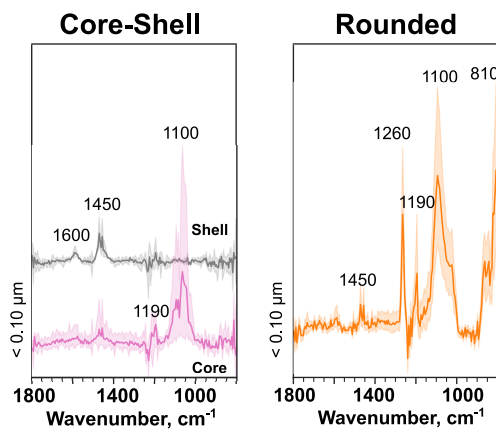


Figure 4.9: PTIR spectra taken for core-shell (left) and rounded (right) hSSA smaller than $0.1 \mu\text{m}$ measured using AFM-IR. Solid lines show the average spectra for a given class, with shaded lines representing the 95% confidence interval.

One of the concerns with off-line sampling in the absence of a scrubber for volatile species is the potential for gas-phase species to react with hydroxyl radical and either condense onto existing SSA or lead to new particle formation. Some evidence of these particles is present in the ultrafine particles ($D_{eq,V} < 100 \text{ nm}$). Similar chemical analyses were conducted for the core-shell and rounded particles found in this size range. Spectra collected are shown in Figure 4.9. From the spectra from the core shell particles, there is evidence of organic modes corresponding to $\delta(\text{CH})$ at 1450 cm^{-1} , and a smaller mode at 1600 cm^{-1} . However, accurate peak assignment is difficult due to the low signal from these small particles. From the core, there is a distinct intense peak around 1100 cm^{-1} , corresponding to presence of sulfate modes. [131, 143] Similarly, in rounded particles shown, there is a clear distinct mode present around 1100 cm^{-1} indicative of sulfates. Presence of these sulfate rich species is consistent with measurements of sulfur containing gases in the marine boundary layer. The presence of sulfate in these particles can be attributed to the oxidation of sulfur containing marine volatile compounds such as dimethylsulfide or

dimethylsulfoxide.[144] Hydroxyl radical oxidation of these sulfur containing marine biogenic gases results in the formation of lower volatility species such as methylsulfonic acid, sulfuric acid, and hydroxyperoxymethyl thioformate,[145, 53, 146] and could lead to new particle formation, resulting in secondary marine aerosols.

4.5 Conclusion

This study investigated the size-dependent particle-to-particle variability of nascent SSA between 0.1 - 0.6 μm . Chemical and physical properties such as morphology, composition and mixing states were probed in response to seawater biological activity and heterogeneous aging in response to hydroxyl radical species. Atomic force microscopy (AFM) imaging identified five main nascent SSA morphologies across the bloom: prism-like, core-shell, rounded, rod, and aggregates. The heterogeneously aged SSA at the peak of the bloom resulted in the formation of rods encapsulated in a shell. The majority of smaller SSA were rounded and core-shell, while larger SSA showed core-shell and prism-like morphologies. The organic nature of smaller SSA was primarily attributed to rounded and core-shell SSA as determined by AFM photothermal infrared spectroscopy, largely comprised of complex sugars and alkanes. Aging resulted in an enhancement of core-shell particles, and evidence of more oxidized species is present spectrally in the larger sized core-shell particles. Additional oxidative processes can be seen through the formation of sulfate-rich particles in the ultrafine size regime. Collectively, present findings revealed a complex and dynamic interplay between SSA size-dependent physicochemical properties, which should be considered to accurately quantify and predict SSA's climate-related effects.

4.6 Acknowledgements

Chapter 4 in part is currently prepared for submission for publication of the material. Kaluarachchi, Chathuri; Or, Victor; Grassian, Vicki; Tivanski, Alexei. The dissertation author was one of the primary investigators and author of this material

This work was supported by the National Science Foundation through the Centers of Chemical Innovation Program under Grant CHE1305427. We would like to thank Dr. Chris Lee, Kathryn Mayer, Jon Sauer, and Professor Kimberly Prather for planning, organizing, and executing the SeaSCAPE mesocosm experiment. We also want to acknowledge Professor Alexei Tivanski and Chathuri Kaluarachchi for helping with sample collection and conducting AFM morphology experiments. The dissertation author was the primary investigator of spectroscopic measurements.

4.7 Supporting Information

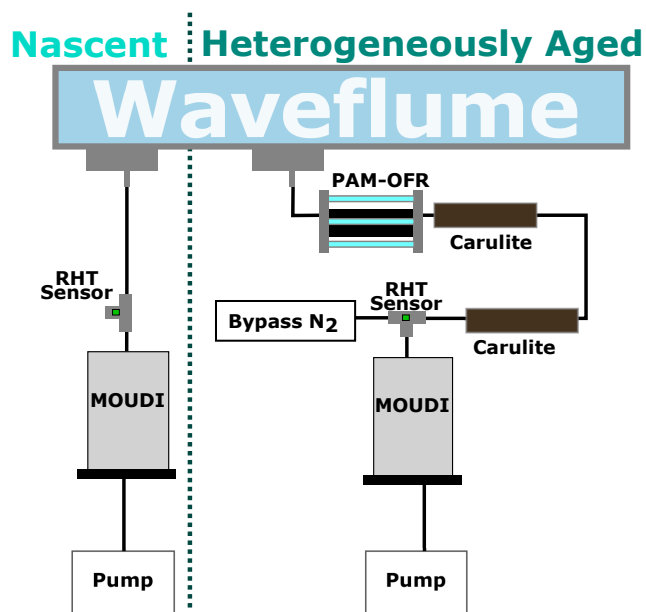


Figure S4.1: Schematic showing sampling lines for preparing substrate deposited SSA from the waveflume. Particles are impacted onto hydrophobic Si wafer substrates in the MOUDI. RH and temperature are measured at right before the MOUDI inlet. For the heterogeneously aged SSA line, two diffusion dryers with Carulite are used to scrub residual ozone. The line is mixed with a bypass of N₂ prior to deposition.

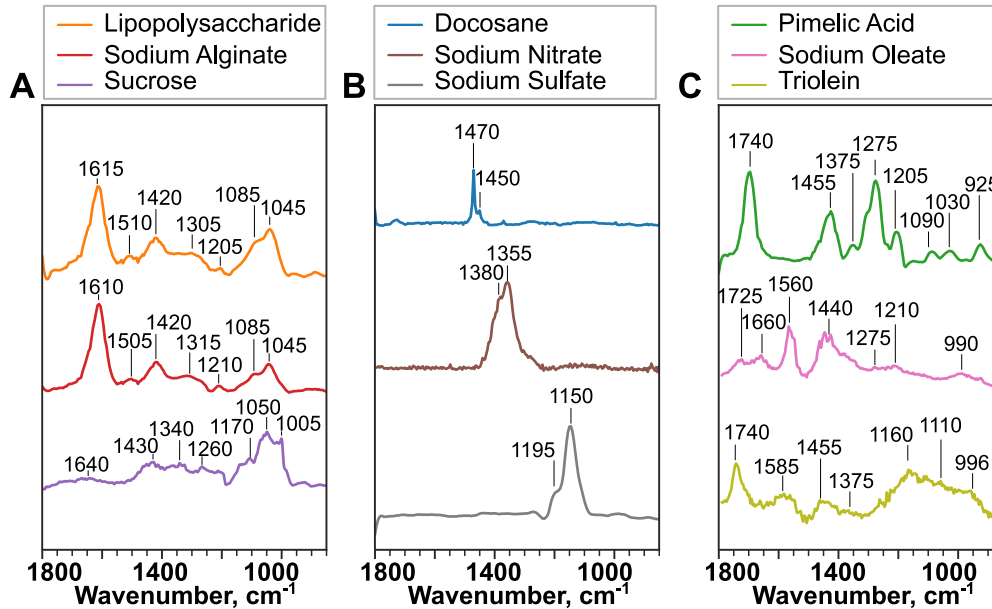


Figure S4.2: AFM-PTIR spectra for substrate deposited reference compounds

Table S4.1: Numerical values for abundances and counts of nascent SSA particles produced throughout the bloom.

Nascent SSA Morphology Distribution					
<i>Pre-Bloom</i>					
$D_{eq,V}$	Prism like	Core-shell	Rounded	Rod	Aggregates
0.10 - 0.18	0	8	26	4	0
0.18 - 0.32	0	15	22	3	3
0.32 - 0.56	8	14	9	0	7
<i>Peak-Bloom</i>					
$D_{eq,V}$	Prism like	Core-shell	Rounded	Rod	Aggregates
0.10 - 0.18	0	4	34	1	13
0.18 - 0.32	3	6	12	10	4
0.32 - 0.56	5	7	3	0	0
<i>Post-Bloom</i>					
$D_{eq,V}, \mu m$	Prism like	Core-shell	Rounded	Rod	Aggregates
0.10 - 0.18	0	19	20	3	10
0.18 - 0.32	0	13	10	4	9
0.32 - 0.56	0	8	2	0	6

Table S4.2: Numerical values for abundances and counts of heterogeneously aged SSA particles produced at the peak of the bloom

Het-Aged SSA Morphology Distribution						
<i>Peak-Bloom</i>						
$D_{eq,V}, \mu m$	Prism like	Core-shell	Rounded	Aggregates	Core-shell (rod)	
0.10 - 0.18	0	12	9	2	2	
0.18 - 0.32	3	13	9	7	1	
0.32 - 0.56	7	22	1	6	1	

Chapter 5

Microspectroscopic imaging and physicochemical characterization of long term indoor depositions on window glass surfaces

5.1 Abstract

Deposition and surface-mediated reactions of adsorbed species can play a role in the level of exposure of occupants to indoor pollutants, which include gases and particles. Detailed molecular-level descriptions of these processes occurring on indoor surfaces are difficult to obtain because of the ever-increasing types of surfaces and their proximity to a variety of different indoor emission sources. The results of an investigation of interactions of glass surfaces in unique indoor environments are described here. Window glass, a ubiquitous indoor surface, was placed vertically in six different locations to assess differences in particle and coating depositions. Atomic force microscopy- photothermal

infrared (AFM-PTIR) spectroscopic analysis of these glass surfaces reveals differences in morphology and chemical composition, which reflects the diversity of surface processes found in local environments indoors. Overall, this detailed microspectroscopic imaging method shows deposition of particles and the formation of organic thin films that increase the surface area and surface roughness of the glass surface. PTIR spectroscopy demonstrates that depositions can be linked to primary emitters intrinsic to each of the different local environments.

5.2 Introduction

A large number of studies focused on understanding atmospheric chemistry and its impact on human health have been undertaken in the past decade. High-impact discoveries in this field maintain a strong focus on atmospheric aerosols, heterogeneous and multiphase chemistry, greenhouse gas emissions, and overall air quality.[147, 84, 83] Although atmospheric chemistry and outdoor air quality remain important, the average person reportedly spends a large majority of their lives (~87%) indoors. Oxidative gases and airborne particulate matter exist indoors at concentrations comparable to, if not higher, than those outdoors.[148, 149, 150, 151, 152, 153] In addition, because of differences in lighting conditions, air circulation, and unique chemical sources and sinks, the impact of indoor air quality on human health is poorly understood.[25, 154, 155] Because a high surface to volume ratio is in indoor environments,[25] indoor surfaces play an important role in defining levels of exposure of occupants to a wide range of indoor pollutants.[156, 157] In particular, complex multiphase and heterogeneous processes have been proposed to occur on indoor surfaces;[5] however, analyzing these complex surfaces to better understand these processes remains a challenge, and there is a current lack of knowledge of various indoor materials.[154, 156, 157] Furthermore, the local indoor environments within which mate-

rials exist can alter the types of primary emitters and transformative processes that are most likely to occur on material surfaces.[69, 158, 159, 160]

Building on this need to understand more details of surfaces in indoor environments, we placed window glass and painted wallboard, surfaces ubiquitous to the indoor environment, in different indoor locations, including a copier room, office, kitchen, and garage. Each of these offers unique local environments with their distinct characteristic primary emitters that can interact with glass surfaces.[150, 69, 158, 161, 162, 163, 68] Herein, microspectroscopic imaging and chemical analysis of these glass surfaces demonstrate that the chemical and morphological evolution of the surface reflects emissions characteristic to a specific indoor environment.

5.3 Materials and Methods

Glass specimens and painted wallboards were placed in the field for 6 months at four field locations: a photocopy room on the campus of The University of Texas at Austin (UT Austin) (copier room), on the desk of a graduate student office at UT Austin (office), on a refrigerator in a residential kitchen (kitchen), and in a residential garage (garage) (see Table S5.1 for details). Laboratory (control) blanks were left unexposed and used as a reference control.

Samples were analyzed using a commercial microscopy system (nanoIR2, Bruker). Atomic force microscopy (AFM) imaging of authentic indoor surfaces was conducted at 298 K and a relative humidity (RH) of $\sim 40\%$ at ambient pressure. For AFM studies, $50 \mu\text{m} \times 50 \mu\text{m}$ images were collected per surface at a scan rate of 0.25 Hz, using silicon nitride probes (tip radius of $\leq 30 \text{ nm}$) with a 33-77 N m⁻¹ spring constant and a 200-400 kHz resonant frequency in tapping mode. Images were collected with a 1-2 mm separation between scanned regions. Image processing and particle property measurements were

conducted using Gwyddion software.

For AFM-PTIR spectroscopy studies, images were collected at a scan rate of 0.5 Hz using gold-coated silicon nitride probes (tip radius of ≤ 30 nm), a 1-7 N m⁻¹ spring constant, and a 75 ± 15 kHz resonant frequency in tapping mode. Spectra were collected by averaging 256 laser pulses at each wavenumber with a spectral resolution of 4 cm⁻¹ and a spatial resolution of < 30 nm. All spectra shown were recorded on a single point within a particle or film without additional averaging between spectra or smoothing filters applied.

Inductively coupled plasma mass spectrometry (iCAP RQ-ICP-MS, ThermoFisher), operated in standard mode, was used to quantify the elemental content of these surfaces. Samples from UT Austin used in this analysis include blank nonexposed, kitchen, office, copier room, garage, and an additional blank containing only the adhesive backing present on all samples.

5.4 Results and Discussion

5.4.1 Glass Surface Morphology

AFM amplitude images of glass surfaces placed in four different indoor environments are shown in Figure 5.1A along with a control sample. It is clear from these images that glass surfaces, after being placed in these different environments, show unique features and characteristics. The images shown in Figure 5.1A are representative of the images obtained for the different environments. To quantify the differences in these surface features, panels B and C of Figure 5.1 show an analysis of surface properties readily quantifiable from AFM images that include the change in surface area and surface roughness, represented by the root-mean-square roughness (R_q). An increase is observed in both surface properties because of deposition. Deposition of particulate matter is expected to cause

increases in surface area and roughness, especially on window glass, a relatively flat indoor surface. The large spread in surface properties within a single piece of glass indicates that these indoor surfaces are far from exhibiting homogeneous depositions. The surface area increases across all exposed glass, most exemplified in the garage and kitchen glass, with increases of up to 50 and 770 μm^2 , respectively, indicating indoor surface to volume ratios naturally will increase with time as deposition of particulate matter continues. The surface roughness increased upon exposure to various environments. The roughest surfaces were the garage and kitchen glass, with R_q values reaching 220 and 500 nm, respectively. Changes in surface roughness are of interest to the indoor environment as the surface structure of the indoor materials will govern the mechanical interaction of the surface with airborne gaseous compounds and particulate matter, where rougher surfaces alter particle adhesion or change rates of surface-mediated reactions.[164]

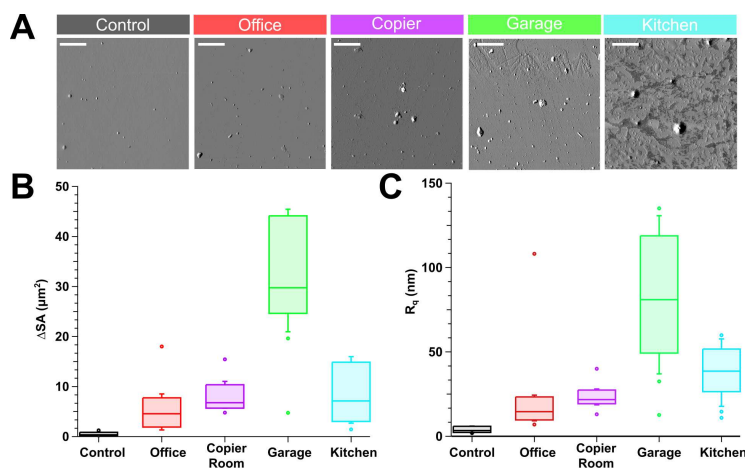


Figure 5.1: (A) AFM amplitude images of the glass surfaces placed in different indoor environments with scale bars set to 10 μm . Box-and-whisker plots (close-up) of AFM-measured changes in (B) surface area and (C) R_q roughness following exposure in each location for 6 months using 10 images (50 $\mu\text{m} \times 50 \mu\text{m}$). Lines show 20 and 80th percentiles. A full view of the plot is available in Figure S5.1

In addition to particle deposition, thin organic films were observed on the glass surfaces placed in the various locations. Film surface coverages were calculated by taking the fraction of the coating surface area over the total surface area. This analysis is

summarized in Figure 5.2A. In the control, office, copier, and garage samples, the surfaces experienced film coatings ranging from 0 to 11%. In contrast, glass exposed to kitchen conditions was heavily coated, ranging from 70 to 99% coverage. Film formation on impervious indoor surfaces has been observed in past studies and has been demonstrated to be largely comprised of organic matter. [165, 166, 64] These films are expected to form in indoor locations with elevated levels of organic compound emissions, exemplified in the kitchen where large quantities of oils and fats are regularly emitted during cooking and cleaning.

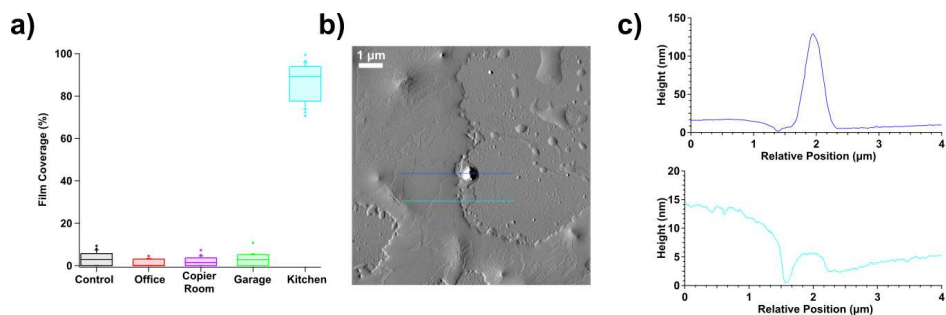


Figure 5.2: (A) Organic film (thickness > 10 nm) coverage on glass surfaces after exposure in each local environment for 6 months taken from the 10 AFM images ($50 \mu\text{m} \times 50 \mu\text{m}$). (B) AFM amplitude image of the organic film coating on kitchen glass after exposure for 6 months. (C) Height profiles taken at lines marked in panel B for a particle (top) and film (bottom). Note the difference in the scale of the height axis.

Shown in Figure 5.2B is an AFM amplitude image of a typical film on kitchen glass. Height profiles are shown at the corresponding line colors in Figure 5.2C. These films are not homogeneous, nor do they completely engulf the surface, where regions of bare silica are visible in the AFM image shown. With films reaching thicknesses in the tens of nanometers, relative to the other locations, in an organic emission-rich indoor environment such as a kitchen, the presence of these coatings confirms that surfaces, when left unattended, act as sizable reservoirs for organic and inorganic compounds. Organic film formation on indoor surfaces is of great interest as coatings will affect surface properties and subsequent interactions with the local environment. Film coatings can be expected

to alter the electrostatic, hydrophobic, and other properties of the surface, altering the adsorption efficiency of the surface toward other molecular species.[56] Films consisting of unsaturated organic compounds can also lead to increases in the levels of surface reactions with ozone.[167, 168, 169] For indoor environments with higher humidity levels such as faucets, baths, and toilets, surface coatings alter the water content of indoor surfaces because of differences between the hygroscopicity of the organic film and underlying building material. Formation of water films on these hygroscopic coatings enables aqueous phase reactions, which are suggested production pathways of very important indoor gases, including the OH radical and HONO.[170]

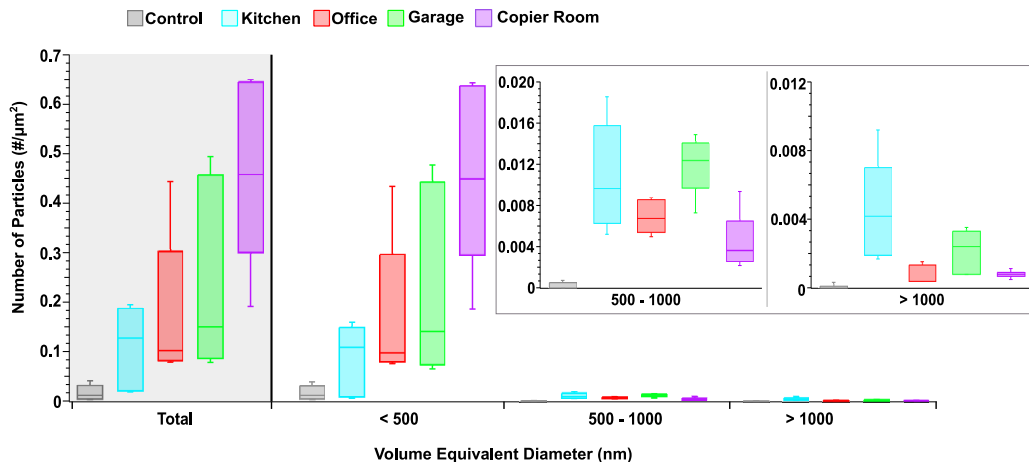


Figure 5.3: Box-and-whisker plot of the number of particles (thickness > 30 nm) deposited per square micrometer on glass surfaces from 10 AFM images ($50 \mu\text{m} \times 50 \mu\text{m}$) for each indoor location. Lines show 20 and 80th percentiles. Particles are categorized by volume equivalent diameter into three size bins: < 500 nm, between 500 and 1000 nm, and > 1000 nm (with total particle counts shown at the far left). Insets show close-ups of the particle counts for the larger-sized particle bins.

The data plotted in Figure 5.3 show the particle depositions across all images on the window glass held in various locations, grouped by diameter into three size bins: < 500 nm, between 500 and 1000 nm, and > 1000 nm. Relative to the control glass, there is an increase in the number of particles deposited across all particle sizes for each location. In all locations, particle depositions were predominantly in the submicrometer size range

with many particles being ≥ 500 nm in diameter, the largest being that of copier glass (avg. 0.449 particle/ μm^2). In contrast, kitchen glass was covered in significantly fewer sub-500 nm sized particles (avg. 0.108 particle/ μm^2). The absence of smaller particles on kitchen glass can be attributed to the heavy coating of organic films, which mask or engulf smaller particles. Exposure of the glass to all indoor locations resulted in a higher level of deposition of the larger-sized particles, the most significant being kitchen and garage glass. The deposition of the smallest particles had a weaker impact on the surface area and roughness. The glass specimens in the photocopy room had the largest fraction of sub-500 nm sized particles but experienced smaller changes in surface area and roughness. In contrast, kitchen and garage surfaces had the largest deposition of particles in the size range of 500-1000 nm, 0.0096 and 0.0124 particle/ μm^2 , respectively, and >1000 nm and subsequently produced the roughest surfaces. The kitchen glass experienced near double the deposition of supermicrometer-sized particles, 0.0044 particle/ μm^2 , in comparison to garage glass, 0.0024 particle/ μm^2 , but produced surfaces with comparatively lower surface areas and roughness, which can be attributed to the morphology of the depositions. Kitchen emissions tended to form smoother mounds of coatings, potentially pools of organic compounds arising from aggregation of smaller organic matter over the sampling period, while garage emissions formed coarser particles with significantly lower levels of organic coatings (see Figure S5.2).

5.4.2 Glass Surface Composition

AFM-PTIR enables acquisition of spectra from depositions with spatial resolution in the tens of nanometers, allowing for microspectroscopic imaging and characterization of depositions.[76, 109] Shown in Figure 5.4 are the PTIR spectra from 1200 to 3600 cm^{-1} taken from the corresponding images of organic depositions found on the kitchen and copier room glass surfaces. Spectra of pure glass are dominated by peaks corresponding to

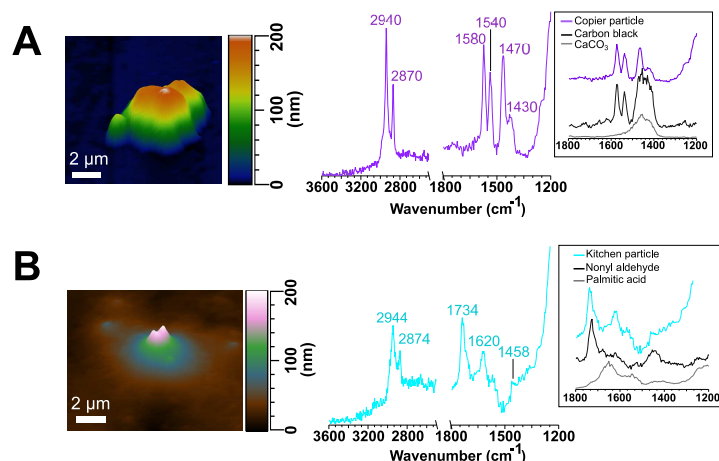


Figure 5.4: (A) Three-dimensional (3D) AFM height image (left) and PTIR spectrum (right) for a deposited particle on the copier glass. The inset shows a comparison with carbon black (black) and CaCO_3 (gray) PTIR spectra. (B) 3D AFM height image (left) and PTIR spectrum (right) for a particle and film on the kitchen glass. The inset shows a comparison with nonyl aldehyde (black) and palmitic acid (gray) PTIR spectra. The region from 800 to 1200 cm^{-1} has been omitted because of the presence of a large Si-O vibrational mode from the underlying glass.

the SiO_2 matrix at $\nu(\text{Si-O})$ (942 , 1018 , and 1092 cm^{-1}) and $\nu(\text{OH})$ (3390 cm^{-1}) (see Figure S5.3A). In comparison, spectral features from deposited particles can be correlated to primary emissions characteristic of a particular indoor location. Most notably, the kitchen particle shown in Figure 5.4B contains a carbonyl stretching frequency associated with an aldehyde compound, identified by $\nu(\text{C=O})$ (1734 cm^{-1}). Carbon-hydrogen stretching motions were identified as CH_2 and CH_3 groups with peaks at 2874 and 2944 cm^{-1} , respectively. We propose these films formed from deposition of aldehydes and long chain fatty acids, the two abundant classes of organic emissions found during cooking.[158, 56, 65] PTIR spectra of palmitic acid and nonyl aldehyde are shown as representatives for these compounds commonly emitted during cooking. Shown in Figure 5.4A is a particle deposited from the copier room with organic content, as indicated by $\nu(\text{CH}_2, \text{CH}_3)$ (2870 , 2940 cm^{-1}). Spectral features suggest a mixture of CaCO_3 from $\nu(\text{CO}_3^{2-})$ (1466 cm^{-1}), a major component of paper, and carbon black from $\nu(\text{C=C})$ (1540 , 1580 cm^{-1}), the primary coloring component of black toners.[69]

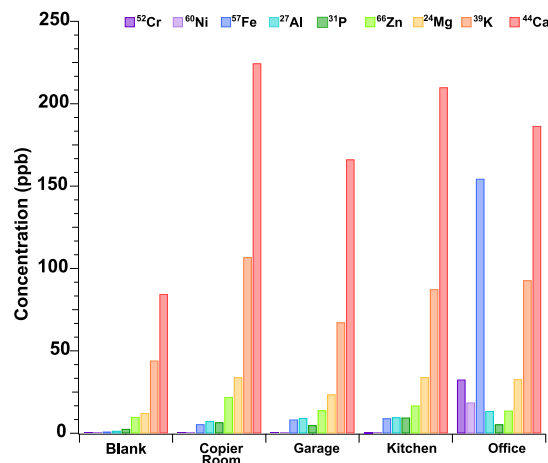


Figure 5.5: ICP-MS analysis of an 1.27 cm × 1.27 cm piece of window glass exposed to various indoor locations showing the nine most abundant elements found. Selected elements for detection include chromium, nickel, iron, aluminum, phosphorus, zinc, magnesium, potassium, calcium, vanadium, cobalt, manganese, copper, lead, and barium. A similar plot of the less abundant elements and a full list of elements screened is available in the Supporting Information. ICP-MS data provided by Michael Alves from Professor Vicki Grassian’s group

To complement the microspectroscopic imaging and physicochemical characterization of AFM-PTIR spectroscopy, analysis of elements present in the different samples was also performed. Shown in Figure 5.5 are the ICP-MS concentrations measured for selected ions. All components detected in the blank sample were measured as the lowest concentration in this study. The relatively high background signal of calcium and potassium in the blank is due to interfering species, ^{40}Ar and $^{38}\text{Ar}^1\text{H}$ respectively, present in the sample matrix. Copier room, garage, and kitchen samples show relatively similar metal concentrations for most elements analyzed. Copier room samples exhibit higher levels of copper, barium, and zinc. Barium and zinc are among the number of metals that can be used as a ferromagnetic composite carrier (for example, barium ferrite), whereas copper is found in many dye compositions.[157] Other commonly found elements in printing toners such as potassium, magnesium, lead, nickel, and others are found at similar concentrations compared to those of the other samples, possibly suggesting selective particulate formation or deposition pathways. A stark difference is seen in the office sample where elevated

levels of iron, chromium, nickel, cobalt, vanadium, and manganese are observed. This can be attributed to the office sample being in the proximity of a stainless steel heating vent, whose composition includes iron, chromium, nickel, molybdenum, and manganese, with trace amounts of vanadium, cobalt, copper, and other elements.[171]

5.5 Painted Surfaces

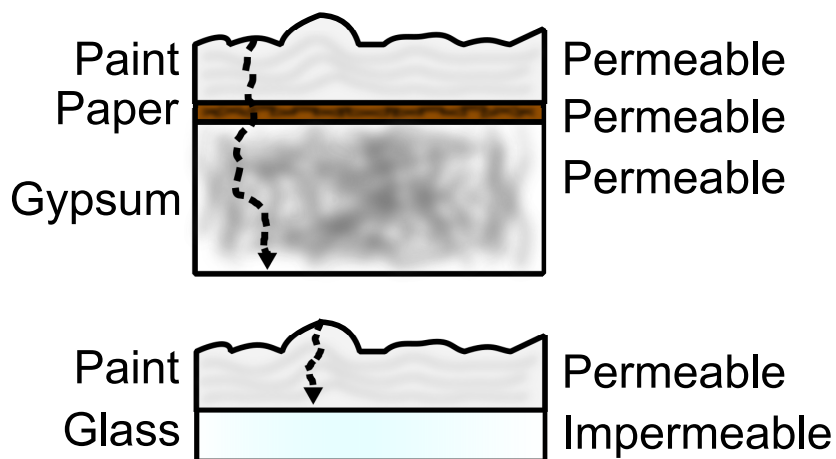


Figure 5.6: Cartoon depiction of the two different types of painted materials: painted paper-on-gypsum wallboard (upper) and painted glass (lower)

Paint is a permeable surface for gas and material diffusion. Consequently, indoor emissions can interact with both the paint coating and the underlying material. To assess the changes to the surface or near-surface composition of painted surface, painted samples were exposed to the kitchen environment for 3 months. Three sets of painted samples were applied on different support material (Figure 5.6): low VOC eggshell paint applied on paper-on-gypsum wallboard (LVOC-WB) and window glass (LVOC-G), and a zero-VOC paint on window glass (ZVOC-G). All paints included acrylic latex resin with 10-30% titanium dioxide (TiO₂) by weight. Wallboard is a more realistic material paint is applied upon, and is permeable to material diffusion, making painted surfaces a larger potential reservoir for materials to accumulate prior to any surface film formation. In con-

trast, window glass is an impermeable material that would more readily facilitate material accumulation in the paint layer, and potential surface modifications. All samples were exposed vertically for three months to examine for material accumulation at the surface or saturation of the underlying material.

5.6 Painted Surfaces

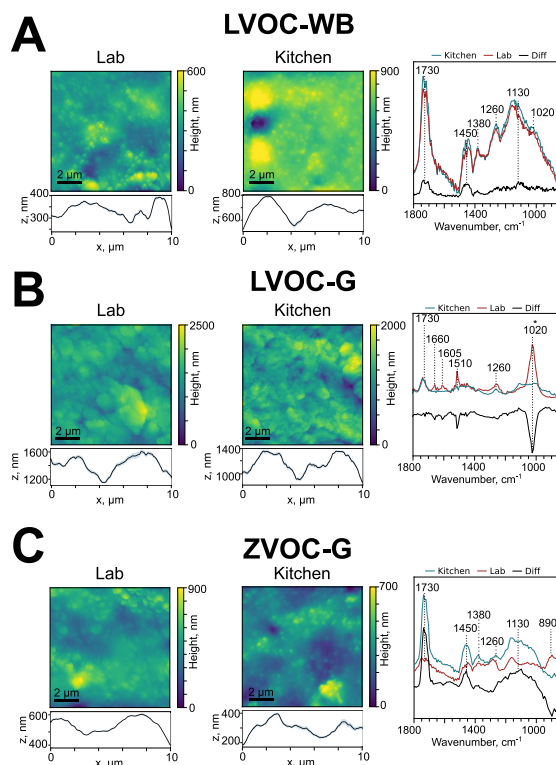


Figure 5.7: AFM height images and profiles for lab (left) and 3-month kitchen exposed (middle) surfaces, with PTIR spectra and difference spectra (right) for: A) LVOC-WB, B) LVOC-G, and C) ZVOC-G

The results from the painted surface are shown in Figure 5.7, with AFM height images and height profiles for the lab (unexposed) and kitchen (3-months) samples in the left and middle panels. The right panel shows the average PTIR spectra from the sample exposed to the kitchen ($N_{spectra} = 25$) and lab ($N_{spectra} = 40$), as well as the difference

spectra between the two to assess spectral changes due to aging. Figure 5.7A shows the LVOC-WB sample, where from AFM height image, there no distinguishable morphological differences between kitchen and lab samples. The surface root-mean-squared roughness (R_q) values shown in Figure 5.8A are also similar between the lab (79 ± 52 nm) and kitchen (79 ± 47) LVOC-WB. The spectral features are largely similar between lab and kitchen exposed LVOC-WB in peak positions and intensities. In the difference spectra, there appears to be two modes around 1730 and 1450 cm^{-1} , which would correspond to $\nu(\text{C}=\text{O})$ and $\delta(\text{CH}_3, \text{CH}_2)$ modes. While these modes are consistent with fatty acids, a common emission from cooking activities, because the peaks overlap with the spectra of the acrylic polymer in the paint material, spectral differences cannot be confidently attribute to the uptake of carbonyl containing organic compounds from kitchen emissions. In the LVOC-G shown in Figure 5.6B, the AFM height images, and roughness values (Figure 5.7A) are similar between the lab and kitchen samples. In the spectra, there are no noticeable differences beyond the loss of a 1020 cm^{-1} peak, which is likely due to the cantilever absorbances from an incomplete gold coating. These results do not demonstrate any evidence of material uptake on or near the surface.

5.7 Painted Surfaces

The changes to the ZVOC-G surface following aging in the kitchen are shown in Figure 5.7C. The latex painted glass appears slightly smoother from the AFM images but cannot readily distinguish due to the non-smooth surface morphology of paint. On the nanoscale, there are large variations in roughness within unexposed paint, limiting statistical comparisons without larger datasets. The R_q of the painted surfaces decreases in both magnitude and intensity upon exposure to the kitchen environment, decreasing from 212 ± 112 nm (lab) to 107 ± 12 nm (kitchen), suggesting the paint layer is saturating and

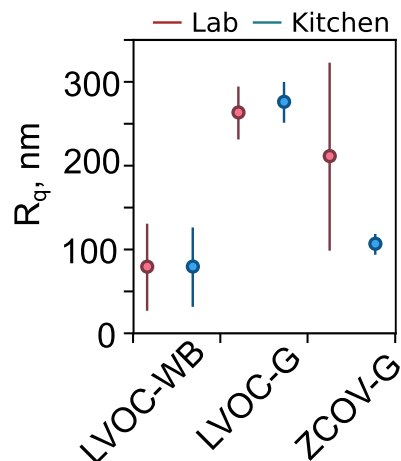


Figure 5.8: A) Root mean squared roughness (R_q) for painted wallboard and painted glass samples B) PTIR difference spectra from the painted surfaces and a reference PTIR spectra from a film on kitchen glass.

subsequently, sorbed indoor materials area accumulating at the surface. These results are corroborated by the PTIR spectra. The kitchen aged Latex-G is more strongly absorbing in regions at 1730, 1450, and 1130 cm^{-1} corresponding to ν (C=O), $\delta(\text{CH}_2, \text{CH}_3)$, and $\nu(\text{C-C}, \text{C-O})$ respectively. While the peak locations are identical between kitchen and lab ZVOC-G, differences in the peak shapes relative to the unexposed material indicates the changes in spectral features are likely attributed to uptake of new material and are spectrally similar to the organic film formed on window glass (Figure 5.8B). However, laboratory studies or longer exposure-time samples are needed to assess the validity of the difference in behavior between these painted samples.

5.8 Conclusion

Overall, these data taken together provide a unique look at the impact of local environments on glass surface physicochemical properties. A comprehensive understanding of the chemistry occurring on indoor surfaces and its subsequent impact on the quality of indoor air requires knowledge of the nature of these surfaces. Unsurprisingly, the different

environments to which indoor surfaces are exposed play a large role in the composition of particles deposited on the surface and the nature and amount of organic coatings. Understanding changes in indoor surfaces over time will enhance our understanding of how these surfaces interact with other gases that are present, including water vapor. Hydrocarbon depositions are expected to increase surface hydrophobicity, whereas water-soluble organic films and salts would enhance surface hygroscopicity. The variance in the distinct indoor emitters will be reflected by differences in the surface properties and chemical composition of the exposed surface. Examination of indoor surfaces under realistic conditions is essential for obtaining a crystal clear understanding of “authentic” indoor surfaces, and this will be only further enhanced with the emergence of new methods to better understand indoor surfaces, which provides insights into their physicochemical characteristics.

5.9 Acknowledgements

Chapter 5, in full, is a reprint of the material published by American Chemical Society in: **Victor W Or**, Michael R Alves, Michael Wade, Sarah Schwab, Richard L Corsi, Vicki H Grassian Crystal Clear? Microspectroscopic Imaging and Physicochemical Characterization of Indoor Depositions on Window Glass. *Environmental Science & Technology Letters*, 5(8), 2018. The dissertation author was the co-first author of this paper. This work was supported by the Alfred P. Sloan Foundation, grant no. G-2017-9692. The authors also thank Dr. Richard Cochran for helpful discussions.

5.10 Supporting Information

5.10.1 Glass and Paint preparation

Clear float glass was purchased from a commercial retailer (AGC Flat Glass North America), 2.5 mm thickness, and cut into $1.27 \times 1.27 \text{ cm}^2$ ($\pm 0.1 \text{ cm}^2$) squares. Glass sample were prewashed with liquinox detergent and DI water, double rinsed with DI water, and then dried with a low lint Kimtech wipe. Upon collection, specimen were immediately stored in air tight opaque containers until analysis. For ICPMS analysis, glass samples were sonicated in a cleaned polypropylene tube with 5 mL of 2% HNO_3 (trace metal grade, Fischer Chemical) and Milli-Q (Thermo, Barnsted EasyPure-II; $\geq 18.2 \text{ M}\Omega \text{ cm}$ resistivity) for 30 minutes at room temperature. Internal standards (ThermoFisher IV-ICPMS-71D) were added after to normalize for transfer error.

Three sets of indoor painted material specimens were prepared for surface/chemical analysis. The materials included gypsum board coated with a low-VOC paint, window glass coated with a low-VOC paint, and window glass coated with a zero-VOC flat paint. All materials were purchased from retail outlets in Austin, Texas. All gypsum board samples were cut into 25.8 cm^2 rectangles. All gypsum board samples were conditioned at approximately $25 \text{ }^\circ\text{C}$ and 50% relative humidity (RH) for two weeks, to simulate the timeframe between painting a new house and occupying the house. Preparation of painted samples were based on California Department of Public Health Standard Method V1.1. Both paints included acrylic latex resin with specifications of 10-30% titanium dioxide by weight. Approximately 0.5 grams of paint was applied to each painted sample. After painting and conditioning, the sides and back of the gypsum board were covered with aluminum tape. All specimens were mounted on foam poster board, which was placed in a vertical position in the field at heights ranging from 0.9- 1.8 m from the floor.

Table S5.1. A summary of the mean field conditions is listed, with data presented

as mean (standard deviation). All specimens were mounted with double sided adhesive on foam poster board, which was placed in a vertical position in the field at heights ranging from 0.9 - 1.8 m from the floor. Participants were instructed to use the area where material specimens were placed as they would under normal (everyday) conditions. With the exception of the residential garage, all locations have an air system operating and supplying conditioned air. The kitchen is connected to the house’s central AC. The office and copier room are inside the same multiple story college building supplied with a Multi-zone VAV system

Table S5.1: Summary of mean field conditions. Data presented as mean (standard deviation). a Connected to a 106 m^3 kitchen and living room. b Connected to a 57.6 m^3 living room

Location	Temp. (°C)	RH (%)	Light Intensity (lumen/m ²)	Room Vol. (m ³)
Photocopier room	22.4(0.2)	56.1(15.1)	146.0(109.7)	54.8
Student Office	23.0(0.8)	52.7(12.5)	40.1(71.5)	48.4
Residential Kitchen	23.5(2.6)	55.0(8.5)	16.9 (38.4)	31.6
Residential Garage	26.7(7.4)	46.2(8.1)	13.2(18.7)	128

5.10.2 Materials for Reference PTIR Spectra

All chemicals used were purchase directly from the manufacturers, utilized without further purification, and included palmitic acid ($\geq 98\%$, Sigma-Aldrich), CaCO₃ ($\geq 99.95\%$, Alfa Aesar), and black carbon (Degussa). Samples were generated from a 1% wt/v aqueous solution using ultrapure water prepared on site (Thermo, Barnsted EasyPure-II; ≥ 18.2 M Ω cm resistivity) . Solutions were deposited onto Si wafer sampling substrates (Ted Pella) and allowed to dry for 24 hours

5.10.3 Analysis of Glass

The AFM-PTIR used consists of an atomic force microscope integrated with a pulsed, tunable infrared optical parametric oscillator (OPO) laser source with a repetition rate of 1 kHz, tuning range of 850 to 2000 cm^{-1} and 2235 to 3600 cm^{-1} , and an average spectral resolution of 4 cm^{-1} . 10 AFM images ($50 \times 50 \mu\text{m}^2$) used to evaluate surface increases in projected surface area (μm^2), root-mean-square roughness (nm), film coverage (%), and number of deposited particles ($\# / \mu\text{m}^2$). Increase in surface area was determined by taking the difference between the measured surface area and the projected surface area ($2,500 \mu\text{m}^2$) for each image. Root mean square roughness (R_q) is a parameter used to describe the distribution of standard deviations for surface heights (z)[172]:

$$R_q = \sqrt{\frac{1}{n} \sum_{i=1}^n z_i^2} \quad (5.1)$$

Where a lower R_q value indicates a flatter surface. Film coverage was determined by taking the ratio of the film surface area and total surface area per image. Particles were identified by setting a lower threshold height limit (thickness = 30 nm) and sized according to their spherical volume equivalent diameter. The total and size categorized particle counts were normalized to the surface area of each image. Films were determined by lowering the height threshold to a thickness of 10 nm.

Table S5.2: Calculated limit of detection (LOD) and limit of quantification (LOQ) values for elements plotted from ICP-MS analysis of glass samples. A LOD or LOQ value of 0.0 indicates a corresponding limit of less than 10 pptv (less than 0.09 $\mu\text{g}/\text{m}^2$).

Element	LOD (ppb)	LOQ (ppb)	LOD ($\mu\text{g}/\text{m}^2$)	LOQ ($\mu\text{g}/\text{m}^2$)
²⁴ Mg	0.1	0.3	0.9	2.6
²⁷ Al	0.1	0.3	0.9	2.6
³¹ P	1.1	3.3	9.5	28.6
³⁹ K	2.2	6.9	19.1	57.3
⁴⁴ Ca	0.3	0.9	2.6	7.8
⁵¹ V	0.0	0.0	0.0	0.0
⁵² Cr	0.0	0.0	0.0	0.0
⁵⁵ Mn	0.0	0.0	0.0	0.0
⁵⁷ Fe	0.0	0.0	0.0	0.0
⁵⁹ Co	0.0	0.0	0.0	0.0
⁶⁰ Ni	0.0	0.0	0.0	0.0
⁶³ Cu	0.0	0.0	0.0	0.0
⁶⁶ Zn	0.0	0.0	0.0	0.0
¹³⁷ Ba	0.0	0.0	0.0	0.0
²⁰⁸ Pb	0.0	0.0	0.0	0.0

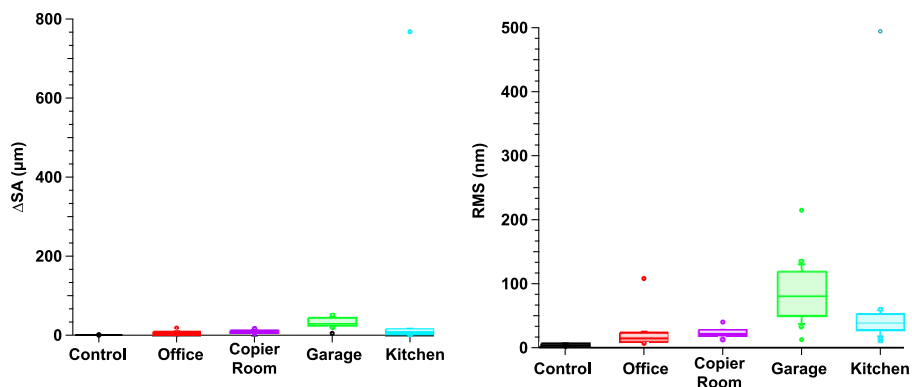


Figure S5.1: Full box and whisker plots showing outlier measurements of A) change in surface area and B) Change in root mean squared roughness. Zoomed in view for the most common values are shown in Figure 5.1 of the main text. Lines show the 20 and 80th percentiles respectively.

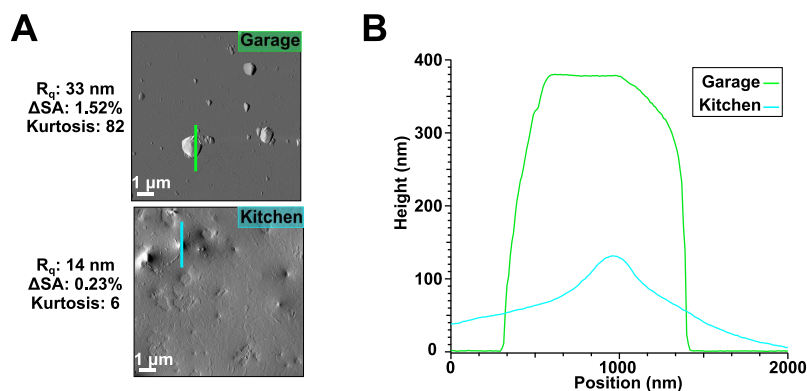


Figure S5.2: A) AFM amplitude images of particles on garage versus kitchen exposed glass, with lines indicating regions where B) height profiles are taken. Also provided are some values for root mean square roughness, change in surface area and kurtosis. For the height versus position plot, it is shown that kitchen particles show a less defined progression in height in contrast to the particle deposited on the glass placed in the garage suggesting these particles are of different composition and phase.

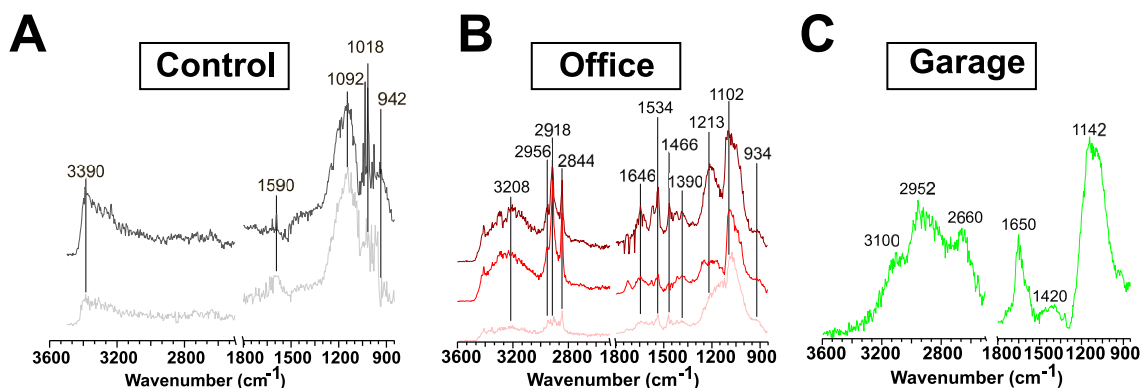


Figure S5.3: A) PTIR Spectra taken on the control glass sample. PTIR spectra taken on particles from the B) office and C) garage exposed glass respectively, showing organic content. Deposition from each indoor location show differing spectral features, suggesting that the location of the window glass determines the chemical composition of subsequent depositions

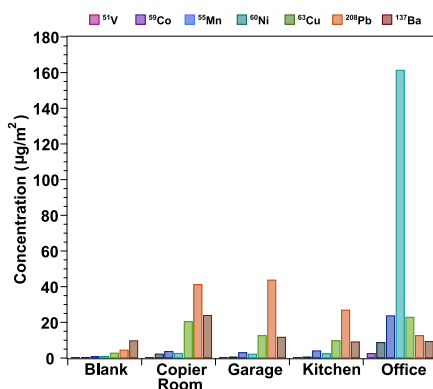


Figure S5.4: Less abundant metals found from ICP-MS analysis of a $1.27 \times 1.27 \text{ cm}^2$ piece of window glass exposed to various indoor locations. Elements detected below 0.1 ppb ($0.9 \mu\text{g}/\text{m}^2$) are not shown, and include Be, Ga, As, Se, Rb, Ag, Cs, La, Ce, Pr, Nd, Sm, Eu, Gd, Dy, Er, Tm, Yb, Lu, Tl, Th, and U.

Chapter 6

Short Term Glass Surface Evolution: Cooking and Cleaning Emissions

6.1 Abstract

Indoor surfaces are extremely diverse and their interactions with airborne compounds and aerosols influence the lifetime and reactivity of indoor emissions. Direct measurements of the physical and chemical state of these surfaces provide insights into the underlying physical and chemical processes involving surface adsorption, surface partitioning and particle deposition. Window glass, a ubiquitous indoor surface, was placed vertically during indoor activities throughout the House Observations of Microbial and Environmental Chemistry (HOMEChem) campaign and then analyzed to measure changes in surface morphology and surface composition. Atomic force microscopy-infrared (AFM-IR) spectroscopic analyses reveal that deposition of submicron particles from cooking events is a contributor to modifying the chemical and physical state of glass surfaces. These results demonstrate that the deposition of glass surfaces can be an important sink for organic rich particles material indoors. These findings also show that particle deposition contributes

enough organic matter from a single day of exposure equivalent to a uniform film up to two nanometers in thickness, and that the chemical distinctness of different indoor activities is reflective of the chemical and morphological changes seen in these indoor surfaces. Comparison of the experimental results to physical deposition models shows variable agreement, suggesting that processes not captured in physical deposition models may play a role in the sticking of particles on indoor surfaces.

6.2 Introduction

Humans spend a majority of their time indoors[54] and there has been an emerging interest in studying the fundamental chemistry influencing the quality of indoor air to which occupants are exposed.[26, 25] Increased effort in indoor chemistry research has been directed towards the characterization and chemistry of gases and aerosols in indoor air.[26, 168, 173, 154, 174, 58] Surfaces and their influence on indoor air quality have begun to receive more attention, as surfaces are important not only for gas-phase adsorption and absorption,[8, 175, 176, 9] the dry depositional loss of particles,[56, 64, 165, 177] and organic film formation[8, 178] but also serve as reaction sites that facilitate new reaction pathways and mechanisms.[179, 180, 5] There are many challenges that complicate the development of a comprehensive molecular level understanding of indoor surface processes and their impacts on indoor air quality.[154] For example, the composition of indoor surface materials are extremely complex and diverse both structurally and chemically.[26, 71] These surfaces range from permeable micro- and macroscopically rough, such as painted walls, to smoother impermeable materials such as window glass. On an impermeable surface contaminant accumulation is expected to occur immediately at the air-surface interface, whereas permeable surfaces can facilitate prolonged uptake via diffusion into the underlying material matrix. Adding on to this complexity, the exact location of the surface will

determine the environmental reaction conditions (light, humidity, and temperature) and the proximity of the indoor surface.[178, 150, 160] For example, windows are more prone to exposure to direct and attenuated sunlight,²⁴ thus photochemistry may be important for these surfaces. Photochemical processes play a role in the production and regulation of oxidative gases in the indoor environment,[176, 62, 181] as well as SOA formation.[182] Surfaces in the presence of high levels of elevated humidity, whether periodic or maintained, can take up water vapor depending on the surface physical and chemical properties. This can lead to the formation of aqueous thin films, which are a potentially important source for gases, including nitrous acid formation, in the indoor space.[170]

As surfaces age, material accumulates through adsorption, absorption, and deposition of gases and particles, respectively. The degree of deposition to a surface obviously depends not only on the exposure time and concentrations of relevant species in air, but also the physical and chemical properties of the surface, which will also evolve with time and move away from the native surface material's original properties. For example, organic film coatings on window glass are predicted to be substantial in theoretical indoor models[8] and have been observed in high-organic loading locations such as kitchens.[178] These organic films are different from the underlying glass from both physical and chemical perspectives. Thus, there is a need to not only study the physiochemical properties and reactivity of the bare indoor surfaces, but also how these properties transform as these surfaces age.

Window glass is a ubiquitous indoor surface, and its interaction with airborne constituents of indoor air have begun to receive more attention. Glass surfaces evolve as material accumulation[64, 165, 183] and film growth[8] occur at the air-surface interface, and substantial material modification is present on glass surfaces aged for weeks or even months.[178] However, these long accumulation time scales restrict the ability to understanding faster processes and interactions at the air-surface interface. Higher time resolu-

tion analyses of surfaces have been conducted but are typically carried out in laboratory environments, often coupled with theoretical simulations, targeting the mechanistic and kinetic behavior of interactions between glass surfaces or proxies with both aerosols[63] and indoor relevant organic compounds,[184, 185, 186] and subsequent reactivity to common gaseous constituents of indoor air such as ozone.[179, 187, 188, 189] The highly specified nature of these experiments often requires use of window glass proxies and use a smaller number of species representative of a broad family of common indoor compounds. By measuring loss behaviors of species in the airborne fraction, higher time resolution field measurements demonstrated that gas-surface partitioning play a major role in the behavior of indoor constituents.[9] However, direct surface measurements capturing the faster timescale evolution of authentic indoor surfaces has yet to be demonstrated.

To probe the progression of authentic indoor surfaces in the presence of common indoor emissions, window glass was exposed to single day cooking activities throughout the month-long HOMEChem experiments. Cooking and cleaning events during the campaign resulted in elevated levels of submicron aerosols and gaseous compounds.[190, 191, 66] Analyses of these glass surfaces reveal substantial particle deposition, dominated in number and volume by the presence of ultrafine and accumulation mode particles respectively. Spectroscopic analysis of particles shows signals associated with organic matter that is interacting with the glass surface, which may facilitate longer-term deposition of more particles onto the glass surface and subsequent increased reactions of the surface with ozone. Interpretation of spectra are supported by chamber studies demonstrating that depositions are spectroscopically mimicked by a mixture of oleic acid, a representative for fatty acids, and its byproducts following reactions with ozone. While the majority of glass surface areas examined were mostly uncoated, the overall volume of the deposited particles over a single day of exposure is equivalent to that of a film on the order of nanometers of thickness.

6.3 Methods

6.3.1 HOMEChem

The House Observations of Microbial and Environmental Chemistry (HOMEChem) study took place in June 2018 at the UTest house in Austin, TX. The study is described in detail by Farmer and Vance *et al.*[190] and included a series of scripted perturbations, including cooking and occupancy events. Of particular relevance to this surface study were two event based days that largely revolved around cooking: a simulated thanksgiving day, in which a traditional US holiday meal was cooked for, and consumed by, 10–15 guests in the test house and a sequential cooking day, in which a vegetable stir-fry and rice were cooked four times throughout a day, separated by periods in which windows and doors were opened to ventilate the house. Additionally, two cleaning events were analyzed, sequential terpene-based floor cleaning, and sequential chlorine-based floor cleaning wherein the floors were mopped using the corresponding cleaning solvents, separated by periods of ventilation. While there are differences in the overall occupancy and appliances used between the two events, time resolved size distributions show that events such as cleaning, cooking, and post-cooking decay phases dominated the degree of aerosol concentration.[191]

6.3.2 Online SMPS particle measurements

Real-time airborne particle size distributions in the size range of 10 nm–533 nm were measured using a Scanning Mobility Particle Sizer (SMPS, TSI). The SMPS recorded one particle size distribution every five minutes. Cumulative size distributions (dN/dDp) were generated by summing the particle counts across the entire exposure duration of each window glass sample collected for AFM and AFM-IR analyses. It is worth noting that number concentrations from the cumulative airborne size distribution cannot be exactly compared to the surface deposited number concentrations without making accurate

measurements of surface deposition rates.

6.3.3 Window glass sampling

For AFM and AFM-IR analyses, window glass was cleaned using sequential methanol and water rinses, and dried in an oven. The glass was cut into 1.3 cm \times 1.3 cm pieces and exposed to several high-emission indoor activities across the HOMEChem campaign. All samples were placed vertically within the shared kitchen and living room area of the UT Test House. Individual glass slides were exposed for approximately 24 hours to one of the following emission activities: thanksgiving (June 18, 2018), and sequential stir-fry cooking (June 6, 2018). A control was taken by exposing the sample for approximately 40 hours during the unoccupied house (June 1–June 3, 2018) scenario. Exact sampling dates and times are provided in Table S6.1. Samples were placed directly on top of the SMPS to minimize spatial differences in emission concentrations and any subsequent transformation or loss processes. Due to the limited time resolution of sample collection, these surface analyses probe the surfaces evolution following the cooking event as well as all other indoor events (ventilation, occupancy, etc.) throughout the exposure period. Samples were stored in sealed stainless-steel containers and shipped to UC San Diego immediately after collection for analyses. Laboratory blanks were prepared at UT Austin, stored for one month in stainless steel shipping containers, and shipped at the end of the of the campaign. Samples were stored in the dark at ambient conditions to minimize changes in surface composition and structure from condensation or photodegradation.[192] We note that during the shipping process, higher volatility products may be lost from the surface. Thus, these offline surface analyses are limited to species that do not readily desorb from the surface passively or during the transportation process. The following results should be interpreted as a characterization of the surface evolution primarily due to lower volatility organic compounds and deposited particles. Additionally, for the smaller sized particles,

these microscopy analyses cannot differentiate between either SOA formation and subsequent deposition or preferential adsorption and aggregation of SVOCs on the surface as island domains.[193, 10]

For ATR-FTIR analysis, a cumulative sample collected over the last three weeks of the campaign was used. Two glass plates (25.5 cm \times 30 cm) were cleaned and placed on top of the shelving unit directly above the stove. The glass plates were placed near vertically, with an approximate tilt of 5°, leaning against the wall. After the end of the campaign, the plates were collected, placed with dirty sides facing each other, wrapped in aluminum foil, sealed in a plastic bag and transported back to William & Mary for analysis. Except for time on a commercial aircraft, samples were stored frozen and were thawed before sample extraction/removal. From a slight tilt of these samples, gravitational settling is expected to enhance material accumulation relative to the fully vertical window glass samples used for microscopy analyses, and inter-sample assessments with these plates and the smaller slides for AFM-IR are strictly limited to spectroscopic comparisons.

6.3.4 AFM-IR method

Samples were analyzed using a commercial microscopy system (nanoIR-2, Bruker) equipped with a tunable mid-IR optical parametric oscillator laser (OPO). AFM imaging was conducted under ambient conditions at 298 K and a relative humidity (RH) of ~40% at ambient pressure to minimize particle deformation or loss. For AFM studies, N = 8 images (30 \times 30 μm^2) were collected per surface at a scan rate of 0.5 Hz and resolution of 1024 \times 1024 px, using silicon nitride probes (tip radius \leq 10 nm) with 33–77 N m⁻¹ spring constant and 200–400 kHz resonant frequency in tapping mode. For AFM-IR studies, images were collected at a scan rate of 0.5 Hz using gold-coated silicon nitride probes (tip radius \leq 30 nm) 1–7 N m⁻¹ spring constant and 75 \pm 15 kHz resonant frequency in tapping mode. Photothermal infrared (PTIR) spectra were collected at tip-localized locations across the

surface with a nominal spatial resolution of <30 nm, a spectral resolution of 8 cm^{-1} , co-averaging 128 laser pulses per wavenumber. All spectra shown were taken on a single point without smoothing filters applied.

6.3.5 ATR-FTIR method

Sample material was removed from the glass plate by scrapping an area of $\sim 8 \times 8\text{ cm}^2$ worth of deposited material off with a cleaned razor blade, piling it onto the ATR-FTIR crystal, and pressing it down onto the crystal with the back side of the cleaned razor blade. The bulk ATR-FTIR spectra were collected with a Shimadzu IRTracer-100 MIRacle 10 with a diamond crystal ATR probe. Spectra were acquired from $600\text{--}4000\text{ cm}^{-1}$; averaging 100 scans per spectrum; Happ–Genzel apodization was applied; and the spectra were recorded as % absorbance. Background spectra were collected using room air.

6.3.6 Teflon chamber and laboratory sample preparation

A 240 L chamber made from fluorinate ethylene propylene (FEP) Teflon film (American Durafilm, MA) was used to replicate an indoor environment. Window glass substrates were cut into $2.0 \times 2.0\text{ cm}^2$ pieces and cleaned by sonicating for 20 minutes in both Milli-Q and methanol and then subsequently dried in an oven ($120\text{ }^\circ\text{C}$) to remove any remaining solvent at the surface. Substrates were placed inside of the chamber and mounted vertically by a Teflon holder. 1 L min^{-1} of zero air (RH ; 5%) was passed through a glass bubbler (frit size A, Ace Glass) containing 300 mL of DI water and 5 mL of oleic acid, to create oleic acid particles. The RH in the chamber was $36 \pm 3\%$ throughout the exposure. The particles then passed through a desiccator that mixed with 3 L min^{-1} of zero air and entered the chamber. A vacuum pump was set to 4 L min^{-1} at the outlet of the chamber. The glass substrates were exposed to oleic acid aerosols for about 8 hours.

Clean unexposed substrates were covered and set to the side as experimental blanks. For ozone exposure, remaining oleic acid in the suspended particle or vapor phase was first removed by letting the chamber go through 4 air exchanges. An ozone generator (Model 2000, Jelight) was used to produce 500 ppb of ozone within the chamber for 4 hours to ensure sufficient oxidation of the deposited oleic acid particles. Ozone was continuously monitored using a Model 202 Ozone Monitor (2B Technologies).

6.3.7 Particle and surface characterization

Image processing and measurements were conducted using Gwyddion™ software. In AFM/AFM-IR analyses, deposited particles were identified by setting a 4 pixel area threshold with a lower height threshold of 2.0 nm relative to the underlying glass. To account for differences in deposition morphologies, particles were sized by converting their volume (V) into their spherical equivalent volume diameter ($D_{eq,V}$):

$$D_{eq,V} = \left(\frac{6V}{\pi} \right)^{1/3} \quad (6.1)$$

The particle aerodynamic diameter (d_a) is related to the volume-equivalent diameter by the formula

$$d = D_{eq,V} (\rho_a / \rho_\chi)^{1/2}$$

$$d_a = D_{eq,V} \left(\frac{\rho C(D_{eq,V})}{\rho_0 C(d_a)} \right) \quad (6.2)$$

where ρ is the particle density, ρ_0 is the unit density and C is the slip factor.[194, 195] To assess particle morphologies, aspect ratios (AR) were determined for each identified particle by taking the ratio of maximum particle height (z_{max}) to the diameter of a circle with an equivalent projected area (A_p):

$$AR = \frac{1}{2} z_{max} \left(\frac{\pi}{A_p} \right)^{1/2} \quad (6.3)$$

A film equivalent thickness ($z_{eq, film}$) was calculated by taking the ratio of the cumulative volume of particles over the projected surface area (SA_0) for each AFM image:

$$z_{eq, film} = \frac{\sum_{i=1}^n V_i}{SA_0} \quad (6.4)$$

Deposition densities ($\rho_{N, surf}$) were calculated by dividing the total number of particles measured by the overall surface area ($900 \mu\text{m}^2$ per image). Values are expressed as per cm^2 for more convenient macroscopic comparisons.

Changes in surface area are calculated by taking the difference between the measured and projected surface area per AFM image:

$$\Delta SA = SA - SA_0 \quad (6.5)$$

The measured surface area (SA) includes the additional surface area provided by the additional dimension of topography, while the projected surface area (SA_0) is the two-dimensional area imaged. A perfectly flat surface should have equal measured and projected surface areas, and subsequently a null change in surface area. Surface roughness values were calculated using root mean square roughness (R_q) per height image, which is readily calculated from an n pixel height images using the height per pixel (z_p) and mean height (\bar{z}):

$$R_q = \sqrt{\frac{1}{n} \sum_{p=1}^n (z_p - \bar{z})^2} \quad (6.6)$$

Surface coverage by particles was calculated by taking the ratio of the summed particle

surface area (SA_i) to the total surface area per AFM image:

$$\theta = \frac{\sum_{i=1}^n SA_i}{SA} \quad (6.7)$$

6.3.8 Modeling methods and parameters

Size-resolved particle deposition rates were analyzed using the Lai–Nazaroff model (2000)[63] that estimated particle deposition onto a smooth surface considering size dependent Brownian and turbulent diffusion and gravitational settling. These modeled results were compared to the glass samples from AFM analyses, which were placed vertically. Thus, gravitational settling was considered negligible. The local airflow condition near the glass surface was approximated by using friction velocity (u^*). The typical range of friction velocity for the indoor environment is 0.3 to 3.0 cm s⁻¹, based on experimental and modeling studies.[196] During the experiments, the central mixing fan circulated indoor air in the house every 7.5 min (eight house volume of air per hour); therefore, to calculate particle deposition onto the vertical glass surface with the sample area of 7200 μm^2 , we used two relatively high values of friction velocity: (1) 1 cm s⁻¹ which represents the typical indoor friction velocity and (2) 3 cm s⁻¹ as an upper boundary limit with a relatively high indoor air mixing condition. Particle sizes were restricted to diameters between 10–532 nm, which were the size ranges that overlapped between the AFM and SMPS measurements. Using the size dependent deposition velocities with airborne concentrations, the time- and size-resolved particle concentrations on the glass surface were calculated for the thanksgiving cooking and stir-fry events. Comparisons were also made between the measured and modeled 24 h integrated particle concentrations (size-resolved) for those two measurement events.

6.4 Results and discussion

6.4.1 AFM surface measurements



Figure 6.1: 3D AFM height images of the glass surfaces exposed to different activities with scale bars set to $5\ \mu\text{m}$. Note height scales increase from 70 to 260 nm across the images of the different activities.

Representative AFM images of particle depositions on window glass are shown in Figure 6.1, where enhanced particle loading is observed in both cooking events. Two controls were employed to look at the relative enhancement of particle deposition. A material blank was exposed to zero emissions, while the unoccupied background served as an event control wherein the glass samples were left to interact with the ambient room air in the absence of any indoor activities. Relative to the material blank, the unoccupied-glass was far from clean, with approximately four-fold more particles (Figure S6.1). These deposited particles can be attributed to infiltration and ventilation of outdoor air which will introduce ambient aerosols to the indoor environment, in combination with emissions of semi-volatile gaseous compounds from building materials and furnishings.[197] The airborne size distribution from the unoccupied background is shown in Figure S6.2. Prior to collection, the oven was running to remove residual material, resulting in an enhancement of PM levels during the collection period. However, even with the elevated PM levels in the unoccupied background, both cooking conditions produced an enhancement in particle deposition across all sizes (Figure 6.1).

As measured by AFM images, the thanksgiving and stir-fry events resulted in an overall density of 6.7×10^8 and 4.3×10^8 particles per cm^2 respectively. Size-segregated particle deposition densities as a function of airborne particle number concentrations for

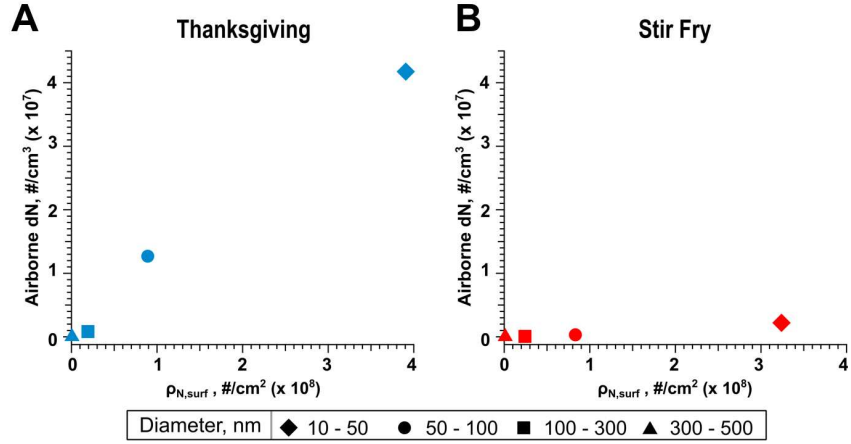


Figure 6.2: Surface deposition densities as a function of cumulative airborne PM number concentrations for (A) thanksgiving (blue) and (B) stir fry (red) events for four particle size bins: 10–50 nm, 50–100 nm, 100–300 nm, and 300–500 nm diameters (D_p and $D_{equiv,V}$ for airborne and surface measured diameters respectively).

each event are shown in Figure 6.2. As expected, the $\rho_{N,surf}$ increases with the airborne concentration in both cases, and the majority of deposited particles are observed in the smaller size bins. However, the densities of surface deposited particles were comparable, if not elevated, from the stir fry event in all size bins. Even in smallest size bin of 10–50 nm particles, there are comparable deposition densities on the surface – 3.9×10^8 and 3.2×10^8 particles per cm^2 in the thanksgiving and stir fry event respectively, but over an order of magnitude higher particles were measured in the airborne fraction during the thanksgiving event. Cooking events size distributions of the airborne PM from the thanksgiving and

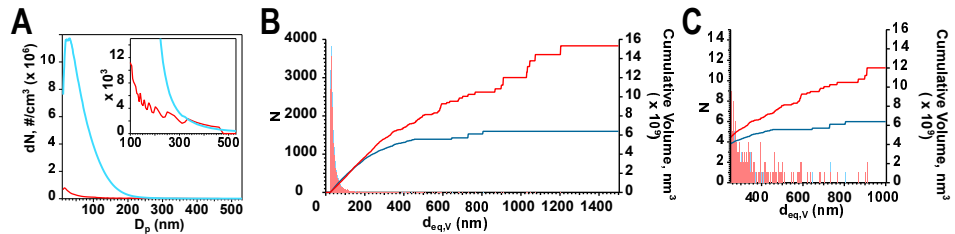


Figure 6.3: (A) Cumulative airborne size distributions from stir fry (red) and thanksgiving (blue) events. (B) Surface deposited number and cumulative volume size distributions from stir fry and thanksgiving events, with a zoom in of the larger submicron sized particles in panel (C). Airborne size distributions provided from Dr. Sameer Patel from Professor Marina Vance’s group.

stir fry cooking events are shown in Figure 6.3A, with corresponding surface deposited size and cumulative volume distributions in Figure 6.3B and C. The thanksgiving event produced higher levels of particles in terms of both mass and number, especially for the particles under 200 nm. However only a slight increase in the deposition of ultrafine sized particles is observed, with a decrease in both accumulation-mode and supermicron sized deposited particles relative to the stir fry event.

In all samples, the predominant fraction of deposited particles by number is within the ultrafine size regime ($D_{eq,V} < 100$ nm). These results are expected as the ultrafine particles dominated the airborne concentration. While we cannot distinguish any preferential surface adsorption of SVOCs in aggregate structures, these results suggest that impermeable flat indoor surfaces like window glass can actively partake in removing ultrafine particles via deposition. Ultrafine particles emitted from these common household events are difficult to regulate and monitor, and a comprehensive understanding of their surface interaction processes are important for gauging the capability of indoor surfaces to remove these particles from the air.

While the majority of deposited particles by number occur in the ultrafine size range, these smaller particles are not necessarily responsible for most of the material modification of indoor surfaces. Relative to the unoccupied background, deposition of the larger particles ($100 \text{ nm} < D_{eq,V} < 1000 \text{ nm}$) are heightened during the thanksgiving, and stir fry events by 208 and 265% respectively. As expected, the overall volume (and subsequent mass) loading of these surfaces due to deposition is dominated by the particles with $D_{eq,V}$ greater than 100 nm. These larger particles comprised 89% and 71% of the deposited material in the stir fry and thanksgiving events respectively. Thus, events with emissions of larger particles (such as cooking) are expected to produce the most organic material loading on surfaces.

Comparison with deposition models

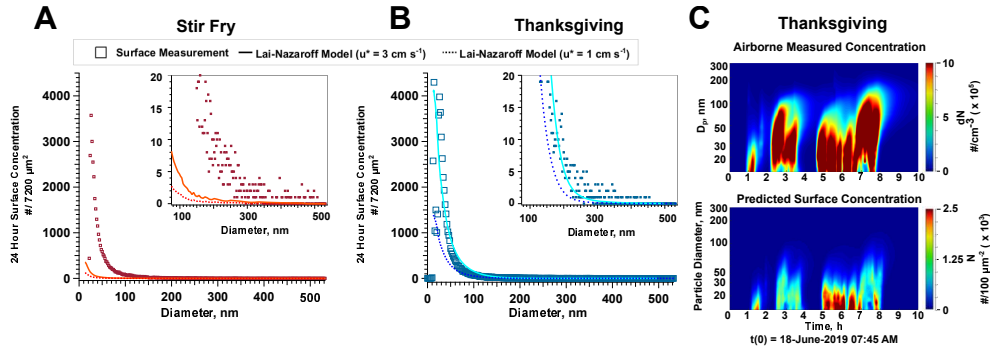


Figure 6.4: Comparison between the size dependent deposition (square markers) measured by AFM and predicted by the Lai–Nazaroff model with surface friction velocity of 1 (dashed line) and 3 (solid line) cm s^{-1} for the (A) thanksgiving and (B) stir fry events. Insets show a zoom in of the larger sized particles. Panel (C) shows the model predicted surface concentrations using the time resolved airborne size distributions from the SMPS. Computational results provided from Professor Donghyun Rim

Particle deposition requires transport from air to a surface and then adhesion (stick) to the surface upon collision. Transport to a surface depends on mixing conditions above the surface and the size of the boundary layer adjacent to the surface. Under otherwise similar air velocities above a surface, a surface with a smaller characteristic length, e.g., small glass specimens versus an entire wall, will have a much smaller average boundary layer thickness and hence a smaller transport resistance for particle interactions with a surface.[29] As such, it is expected that for the small glass specimens used in this study the friction velocity should have been relatively large and transport resistance relatively small. If this was the case, the effects of adhesion resistance were magnified. A comparison of the field measurements with the Lai–Nazaroff deposition model for particles onto smooth surfaces is shown in Figure 6.4A and B for the thanksgiving and stir fry events, respectively. The model itself accounts for turbulent diffusion and Brownian motion on a smooth vertical surface. Size-resolved particle deposition was modeled for the size range of 10–532 nm that overlaps between the SMPS and AFM measurements. We see good agreement between the model and measured values for particle deposition in the thanksgiving cooking event

wherein particles under 75 nm are predicted well with a surface friction velocity of 3 cm s⁻¹. The calculated ranges for deposition velocity were 6.98×10^{-5} to 5.24×10^{-3} cm s⁻¹ ($u^* = 3$ cm s⁻¹) and 2.0×10^{-5} to 1.75×10^{-3} cm s⁻¹ ($u^* = 1$ cm s⁻¹). These deposition velocities are slightly lower but comparable to previously reported deposition velocities of fine-mode particles onto vertical surfaces, where reported deposition velocities ranged from 5×10^{-3} to 2×10^{-5} cm s⁻¹. [63, 198, 28, 199, 200, 201, 202] The detailed simulated time- and size-resolved particle depositions for the thanksgiving event are shown in Figure 6.4C, wherein the elevated levels of deposition are predicted to be around the 13:00–15:00 (t = 5–6.5 h) and 15:30–16:00 (t = 7–7.5 h), which corresponded to the thanksgiving preparation and cooking events, large sources for primary and secondary aerosols. Interestingly, even with a surface friction velocity of 3 cm s⁻¹, the model vastly under predicts the deposition observed in the stir fry scenario, in which we observe roughly an order of magnitude more deposited particles than predicted.

Several factors may have contributed to discrepancies between modeled and measured levels of particle deposition. It is possible, for example, that the stir-fry event produced lower volatility particles or compounds that had a higher affinity to adhere to window glass, thereby resulting in lower adhesion resistance and enhanced particle deposition. Specific surface chemical interactions are not considered in the current deposition models nor are issues related to surface adhesion forces, which dictate whether particles “stick” or “bounce” after contact. It is also possible that transport resistance was lower for stir-fry events than for the thanksgiving event due to greater air speeds adjacent to glass surfaces. Measurements of air speed above surfaces were not completed during experiments and so it is not possible to confirm whether lower transport resistance occurred during experiments. These discrepancies and findings highlight the importance of probing in more detail the physiochemical interactions between indoor surface and particle emissions. Cooking events release considerable amounts of organics, highly diverse in composition, [65] from

both any oil splash and cooking processes. Emissions of primary particles from cooking and formation of secondary particles from condensation of semi- and low-volatility gases on new or existing particles enhances particle mass in to the indoor air space.[158, 203] Primary emissions from the cooking processes are likely the main driving factor causing enhanced levels of organic aerosols in the indoor air and thus deposited on window glass surfaces.[190, 67]

6.4.2 Particle viscosity

Shown in Figure 6.5 are plots of the particle height-to-base aspect ratio (AR) as a function of their spherical volume equivalent diameter. Briefly, a higher aspect ratio is indicative of little to no deformation upon deposition and tends towards more viscous solid particles, whereas low aspect ratios are found in flat, highly spread particles, suggestive of liquid or semi-solid particles[204]. While the final morphology of the deposited particles will depend on complex interactions arising from surface-particle interactions and other physiochemical properties of the particle and surface, the size-specific provide qualitative insight into the viscosity of different particle types.

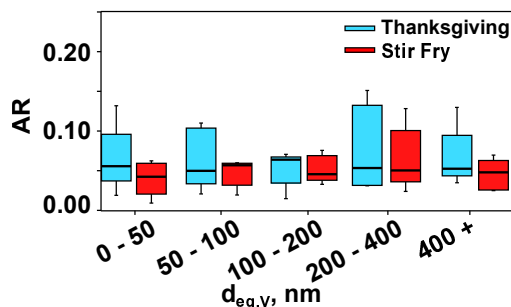


Figure 6.5: Box plots of particle aspect ratio as a function spherical equivalent diameter for all deposited particles taken from the AFM images ($30 \times 30 \mu m^2$) per event (thanksgiving – blue and stir fry – red). Boxes show the 25th and 75th percentiles, and lines show 10 and 90th percentile respectively.

Due to changes in environmental conditions, some evaporation of water vapor and higher volatility organic compounds is to be expected during shipping and storage, which

can alter the phase state, viscosity, and morphology of the particles.[205, 45, 206, 207, 208] These discrepancies can be addressed by future investigations into different environmental conditions focused on the reversibility of different VOCs and water vapor uptake. Nearly all deposited particles were flat – 99.9% and 99.6% of particles under an AR of 0.165 in the stir fry and thanksgiving events respectively. This large degree of spreading is typically indicative of less viscous liquid-like organic particles.[205] It is conceivable that the large predominance of highly spread particles could have arisen due to higher viscosity particles bouncing off of the surface. Even in higher pressure impactor systems, aerosols that collide with substrates and collection surfaces can either collide and remain on the surface or bounce back off into the headspace.[209] The depositions observed in this study are more representative of the deposition and adsorption part of the overall particle–surface interactions. While AR analyses provide some insight into the phase state of deposited particles, these measurements do not provide any metric directly translatable into actual values of the particle viscosity or relevant forces such as adhesion or surface tension. These parameters can be accessed with techniques such force spectroscopy[205, 105, 210] and tensiometry,[211, 212] and such measurements are needed to properly address the impact of viscosity on deposition model accuracy.

6.4.3 Spectroscopic characterization of deposited particles

A comparison of spectra taken from different deposited material on window glass is shown in Figure 6.6. Tip-localized PTIR spectra shown were taken on deposited particles from a day of stir-frying events in HOMEChem. A reference PTIR spectra was also taken on a film that developed on window glass exposed to a residential kitchen environment for one month, separate from the HOMEChem campaign. The ATR-FTIR spectra shown in black are taken from material extracted from window glass samples exposed to the last three weeks of HOMEChem activity. Spectrally, there is strong overlap between spectra

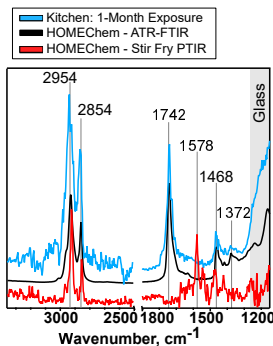


Figure 6.6: Comparison of PTIR spectra taken from a film coating on kitchen glass from 1 month old kitchen glass outside of the HOMEChem campaign (blue), ATR-FTIR spectrum of acetonitrile-extracted material from 3 week exposed glass during HOMEChem (black), and PTIR spectra of deposited particles on window glass from a single day of exposure to stir fry cooking (red). ATR-FTIR data provided from Hannah Przelomski from Professor Rachel O’Brien’s group

taken from the two long-term exposed glass surfaces. The glass from HOMEChem (ATR-FTIR) exposed for three weeks and 1 month glass exposed to the kitchen, with a strong $\nu(\text{C}=\text{O})$ peak around 1742 cm^{-1} . It is important to note that the ATR-FTIR spectra show the spectral signatures of species that have been scraped off the window glass. However, there is still strong spectral overlap with the PTIR spectra from the 1 month exposed kitchen glass, wherein analyses of deposited particles can be conducted without disturbing them from their interactions with the underlying glass. In comparison, in the glass exposed to just a single day of sequential stir fry events, there is a noticeable peak around 3414 cm^{-1} from OH stretching motions. In addition, there is no obvious peak present in the spectral range associated with a carbonyl stretch, $\nu(\text{C}=\text{O})$ around 1700 cm^{-1} , but instead a predominant peak at 1578 cm^{-1} , which we are attributing to the asymmetric stretch of carboxylate and potentially some unreacted alkenyl functional groups. The absence of this mode in the longer-term exposed window glass may be indicative of longer time-scale processes displacing surface-bound compounds or changing the speciation of deposited materials via acid–base reactions.

To confirm the organic nature of the deposited materials from both cooking events,

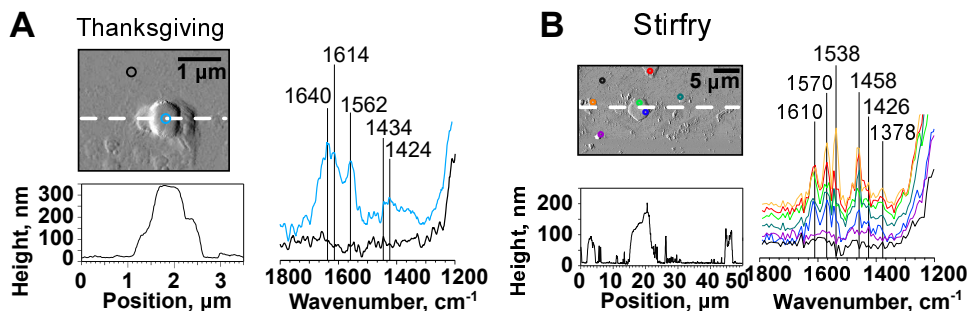


Figure 6.7: PTIR spectra and the corresponding AFM images (with color marked locations) of deposited particles from (A) thanksgiving, and (B) stir fry events. Spectral features of these particles show deprotonated organics, as indicated by the $\nu_{as}(\text{COO}^-)$ and $\nu_s(\text{COO}^-)$ modes around 1580 and 1450 cm^{-1} respectively.

tip-localized IR spectra were collected on deposited particles from the corresponding events, with representative particles shown in Figure 6.7. The high spatial resolution [109, 76] of the AFM-IR enables spectroscopic analyses of these submicron particles on a single particle basis. [213] Spectra from deposited particles reveal that these particles contain carboxylate moieties, as indicated by the strong $\nu_{as}(\text{COO}^-)$ and $\nu_s(\text{COO}^-)$ modes around 1570 and 1430 cm^{-1} respectively, with slight variations in the overall curve shape and peak positions. Additional spectroscopically characterized particles are shown in Figure S6.4 and S6.5 wherein the most common spectra in analyzed particles are carboxylate-rich species. Low exposure time and lack of ambient oxidants would allow some alkenyl groups to persist within depositions, and if so, $\nu(\text{C}=\text{C})$ modes can be expected to contribute to the peak observed around 1610 cm^{-1} . The presence of these species may be caused by non-acidic environments at the aqueous silica interface. [214, 215] Alternatively, they may arise due to bonding with the silica surfaces in window glass. [216] In the spectra shown, particles also show bands around 1400 cm^{-1} that can be associated with $\delta(\text{CH}_3)/\delta(\text{CH}_2)$ modes. A spectral comparison of the stir fry deposited particles with some laboratory generated surfaces is shown in Figure 6.8, wherein oleic acid particles, representing fatty acids which are commonly emitted during cooking, [65] are used as a laboratory proxy for cooking organic aerosols.

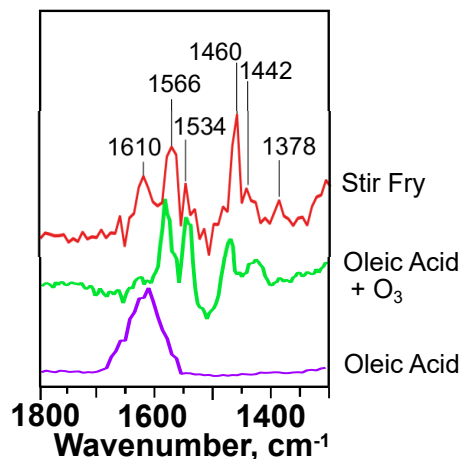


Figure 6.8: Spectral comparison between PTIR spectra taken on depositions from the stir fry event and laboratory mimetics generated in a Teflon chamber: oleic acid particles in purple and oleic acid particles oxidized with ozone in green.

We observe that there is fairly good overlap of the vibrational modes associated with the functional groups from a mixture of oxidized and unoxidized fatty acids. Some of the major products of oleic acid oxidation through ozone are nonyl aldehyde (nonanal), nonanoic acid, among many other carbonyl containing compounds. Previous studies reported sharp increases in nonanal emissions over time from material placed in a kitchen environment and sequentially exposed to ozone.[167] Unreacted oleic acid particles deposited on window glass gives rise to a single detected mode at 1610 cm^{-1} . Surprisingly, even with the oxidation of oleic acid we do not observe the vibrational modes associated with protonated carboxylic acids or other carbonyl groups that we expect around 1700 cm^{-1} . Rather, we observe the formation of a pair of doublets corresponding to the asymmetric and symmetric carboxylate stretches around $1566, 1534\text{ cm}^{-1}$ and $1469, 1442\text{ cm}^{-1}$ respectively. The presence of a carboxylic acid group could potentially be important for enabling long term binding of the particle onto the surface, allowing them to remain adsorbed for longer durations of time. These results suggest the potential importance of surface-particle chemical interactions, the influence surface acidity on deposition speciation, and the availability of binding moieties on the surface to facilitate particle

deposition. The deposited particle from the thanksgiving event shows similar carboxylate modes present around 1610, 1562 and 1424 cm^{-1} . However, an additional more intense mode is observed around 1640 cm^{-1} . Narrowing down the exact family of molecules responsible for this absorbance feature is beyond the capabilities of these analyses. However, potential contributors are unreacted alkenyl moieties from of unsaturated organics, amides which have been detected from meat cooking,[65] or from the O–H bends of hydroxyl containing species like absorbed water.[217] Nebulized water-soluble extracts from the larger glass plate have reported elemental ratios O/C and H/C of 0.21 and 1.8 respectively,[190] consistent within the reported range of typical O/C ratios for cooking organic aerosols measured in both residential kitchens and produced and aged in chambers. The collection period of the extract is on the order of weeks, and thus are susceptible to reactions with light or reactive gases. Chamber and laboratory studies looking at elemental ratios of cooking organic aerosols found that unreacted emissions were typically found with an O/C around 0.1. Upon aging in the presence of ozone or UV light, O/C ratios increased to around 0.2 to 0.3.[218, 219] These results further suggest the surface deposited particles samples have been aged, however, narrowing down the exact source, location (surface deposited or aerosol phase), and mechanism for this aging (oxidant, photochemical, or even degradation from high cooking temperatures) is beyond the current capabilities of these analyses. Future investigations are needed to investigate the influence of particle composition on deposition, and subsequent physiochemical properties of indoor surfaces such as photochemical reactivity, water uptake, and gas-species partitioning. In addition to how these properties change upon surface aging under realistic indoor conditions.

6.4.4 Impact of deposition on surface properties

A few surface properties of interest calculated using the same AFM images ($N = 8$) as above are summarized in Table 6.1. These properties include surface roughness, change

in surface area, equivalent film thickness, and surface coverage. Properties such as film equivalent thickness and roughness can be heavily skewed by the presence of supermicron particles, which could have originated from deposition of dust or glass shards during the substrate cleaving. Because these offline analyses cannot discriminate the origin of these large particles, calculated values shown in Table 6.1 do not include corrections for the presence of these large particles. These larger particles were present in only one image from both the unoccupied background (Figure S6.3) and laboratory blank, resulting in relatively large errors. However, a comparison of the surface properties is summarized in Table S6.2 with and without the corresponding images.

Table 6.1: Surface properties of window glass exposed to various indoor events throughout HOMEChem measured by AFM, with standard deviations shown in parentheses

Event	^a R_q , nm	^b ΔSA , μm^2	^c $z_{eq, film}$, nm	^d θ , %
Laboratory blank	6.0(8.5)	1.0(1.2)	0.4(0.7)	1.8(1.2)
Unoccupied background	7.8(13.2)	1.4(1.2)	0.8(1.2)	6.0(3.9)
Thanksgiving	4.9(2.1)	2.7(0.7)	0.9(0.5)	10.9(1.9)
Stir Fry	11.2(5.3)	3.3(2.0)	2.1(1.1)	18.5(5.6)

^a R_q : root mean square roughness (eqn 6.6).

^b ΔSA : change in surface area (eqn 6.4).

^c $z_{eq, film}$: film equivalent thickness (eqn 6.5).

^d θ : surface coverage by deposited material taller than 2.0 nm in height (eqn 6.7)

For all properties measured, the stir fry event saw the larger departure from the control. For comparisons with current models and studies on indoor film formation, the total volume of the particles is projected as a film of uniform thickness onto the surface area of each image. In the unoccupied control, due to the high levels of adsorbed particles there is a 0.8 ± 1.2 nm thick film. However, this value is noticeably enhanced following the stir fry (2.1 ± 1.1 nm) event and slightly elevated for the thanksgiving (0.9 ± 0.5 nm) event. Under the assumption that the deposited particles are 50% organic, this would still correlate to a 1.2 nm equivalent film of organics in the stir fry event, suggesting that in high emission events like cooking, particle mass loading onto indoor surfaces will play a

major role in altering the organic coating of the indoor emissions.

Surface coverage values (Table 6.1) provide further insight into deposition heterogeneity across the surfaces, where regions of bare glass and particle-coated glass are present. Coverage in the background sample was approximately $6 \pm 4\%$. Expectedly, the largest deviation from the blank occurred in the stir fry event ($8 \pm 6\%$) and thanksgiving produced moderate coverage ($11 \pm 2\%$), but overall much of the surface was left uncovered. Low surface coating is unsurprising as the samples were only exposed for a single day event. Surface roughness increased marginally relative to the unoccupied scenario (7.8 ± 13.2 nm) in the stir fry (11.2 ± 5.3 nm) but decreased in the thanksgiving event (4.9 ± 2.1 nm). Similarly, changes in surface area for the stir fry and thanksgiving scenarios were small, $3.3 \pm 2.0 \mu\text{m}^2$ and $2.7 \pm 0.7 \mu\text{m}^2$ respectively. These findings are consistent with a recent study which found that increases in surface area and roughness were most drastically impacted by larger sized particles.[178] In all emission cases, particle deposition was predominantly ultrafine in terms of number, and subsequently, changes to surface area and roughness are relatively low.

6.4.5 Cleaning events: Influences on surfaces

The impact of the cleaning events on glass surfaces differed between the two the cleaning agents, with representative AFM images shown in Figure 6.9A. The corresponding AFM measured size distributions is shown in Figure 6.9B, in which the terpene based cleaning resulted in a slight increase in deposited particles relative to the blank, while the chlorine cleaning resulted in particles detected in similar quantities to the cooking events. The discrepancy between the two observed cleaning events can be potentially attributed to the composition of the primary emission and reactions they can partake in. The active ingredient in household chlorine bleach cleaning is NaOCl, which can readily dissociate in water to form HOCl, releasing large quantities of both gaseous HOCl and Cl₂,

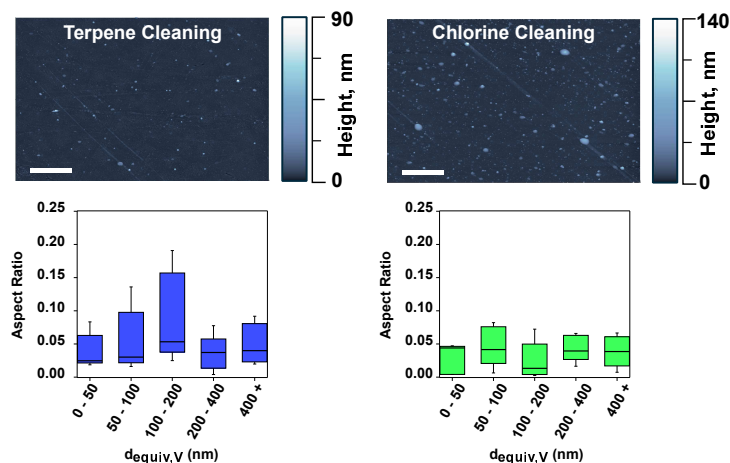


Figure 6.9: 3D AFM height images (upper) of the glass surfaces exposed to different activities with scale bars set to $5 \mu\text{m}$. Note height scales increase from 90 to 140 nm across the images of the different activities. Corresponding box plots of particle aspect ratio as a function spherical equivalent diameter for all deposited particles taken from the AFM images ($30 \times 30 \mu\text{m}^2$) per event. Boxes show the 25th and 75th percentiles, and lines show 10 and 90th percentile respectively.

reaching up to hundreds of ppb.[176] These chlorine containing oxidizing agents has been shown to readily react with unsaturated hydrocarbons to produce higher molecular weight nonvolatile chlorinated products.[176, 220, 188] Accordingly, these nonvolatile compounds can readily condense and form new small particles or grow larger particles. The large degree of surface depositions suggests that chlorine chemistry plays a major role not only in altering the composition of the indoor air, but also contributes to significant deposition onto glass surfaces. These findings are consistent with previous laboratory studies, which predicted significant HOCl loss to surfaces.[176] Chlorine cleaning has been shown to not affect the organic content levels of aerosol, and the significant increase in depositions following chlorine cleaning may be indicative of reactive partitioning processes of chlorine, altering the composition and subsequent deposition efficiency of the ambient particles or even the composition of the glass surface itself.

In contrast, terpene-based cleaning materials are largely surfactants and terpene hydrocarbons and alcohols. These hydrocarbons and alcohols can partake in secondary

organic aerosol formation following oxidative reactions with ozone, which produce various aldehydes, ketones, and carboxylic acids. The formation of secondary organic aerosols following terpene oxidation has been extensively characterized in atmospheric studies, and fairly well characterized with an indoor environmental emphasis.[159, 221, 222, 223, 224] Ozonolysis of gas-phase terpenes occurs at a rate comparable to the air exchange rates[147], and thus significant enrichment enhancement of organic aerosols is expected following terpene cleaning. However, we observe minimal changes in surface depositions, suggesting the impact of these particles on window glass surfaces is low. This can be due to either the time scale between sample collection and analysis, allowing for these oxidized products to desorb, or low collection efficiency of terpene based cleaning constituents and their oxidized byproducts onto window glass and warrant additional laboratory and field studies.

6.5 Conclusion

Common indoor activities like cooking and cleaning contribute high levels of particle emissions that subsequently deposit onto indoor surfaces. These particles are largely organic as suggested by their deposited morphologies and spectral signatures. Studying the evolution of these surfaces due to single events provides a more complete picture of how a specific set of activities contributes towards the evolution of indoor surfaces. Coexistence of coated and bare surface creates a more complex picture that must be considered when accurately modeling these indoor surfaces. Depending on the coverage, aged surfaces can behave like a mixture of the native surface and surface-bound particulate matter, and this ratio between bare and coated regions can vary over time. These surface-based analyses provide a more comprehensive picture, which can be used to guide modelers on which properties contribute towards more long-term evolution of surfaces. Additional studies are needed to expand the existing knowledge base indoor surface chemistry towards

different types of surfaces, such as painted walls and carpet, where nanoscale imaging techniques may be challenged by the roughness, softness, and porous nature of these surfaces. Moreover, characterizing these surfaces is only part of the picture, and future studies are required to understand how these surfaces and the constituents that deposit on them undergo reaction chemistry in indoor environments. What we observe from this study is that even just considering a single event indoors such as cooking with window glass, there remains complexities and challenges with some suggestions of interesting underlying chemical interactions not captured in current deposition models. A single day of simulated exposure produces large amounts of material loading onto these surfaces, the nature of which will depend on the type surface in addition to the type and duration of the details of the different activities, leaving many challenges as well as opportunities in unraveling the complexities associated with the chemistry and composition of indoor surfaces.

6.6 Acknowledgements

Chapter 6, in full, is a reprint of the material published by The Royal Society of Chemistry in: **Victor W Or**, Michael Wade, Sameer Patel, Michael R Alves, Deborah Kim, Sarah Schwab, Hannah Przelomski, Rachel O'Brien, Donghyun Rim, Richard L Corsi, Marina E Vance, Delphine K Farmer, Vicki H Grassian Glass surface evolution following gas adsorption and particle deposition from indoor cooking events as probed by microspectroscopic analysis, *Environmental Science: Processes & Impacts*, 22(8), 2020. The dissertation author was the co-first author of this paper. This work was supported by the Alfred P. Sloan Foundation, grant no. G-2017-9692. We also want to acknowledge Professor Atila Novoselak for his key role in organizing and conducting the HOMEChem campaign and Professor Charlie Weschler for his helpful discussions and insight.

6.7 Supporting Information

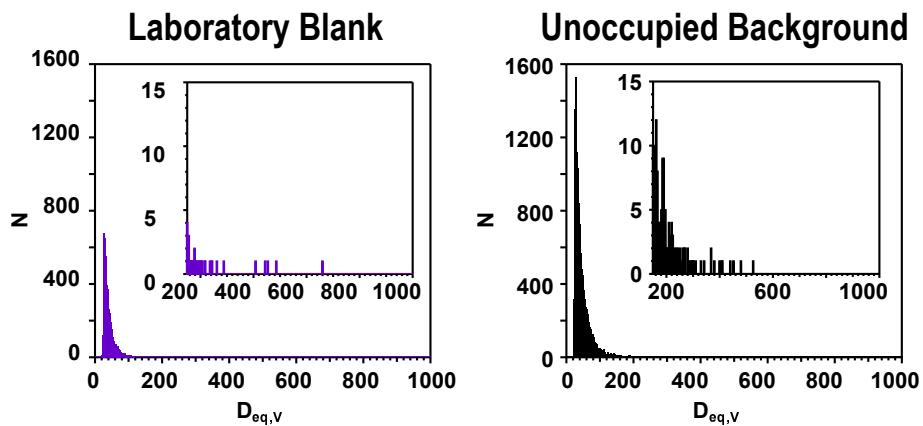


Figure S6.1: Surface deposited number distributions from laboratory blank (left) and unoccupied background (right) event, with insets showing the larger submicron sized particles.

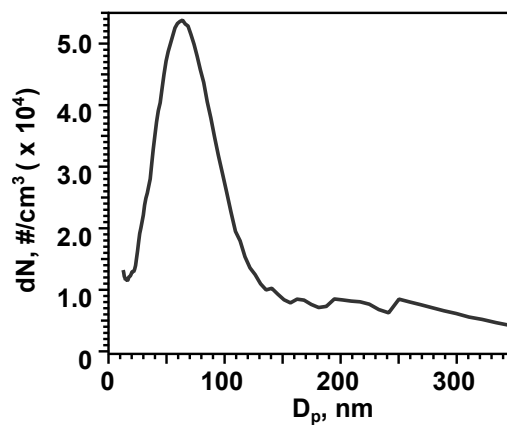


Figure S6.2: Cumulative airborne size distributions from the unoccupied background event measured by the SMPS. The start of the sampling overlapped with the decay phase of an oven run which resulted in an elevated concentration of UFP.

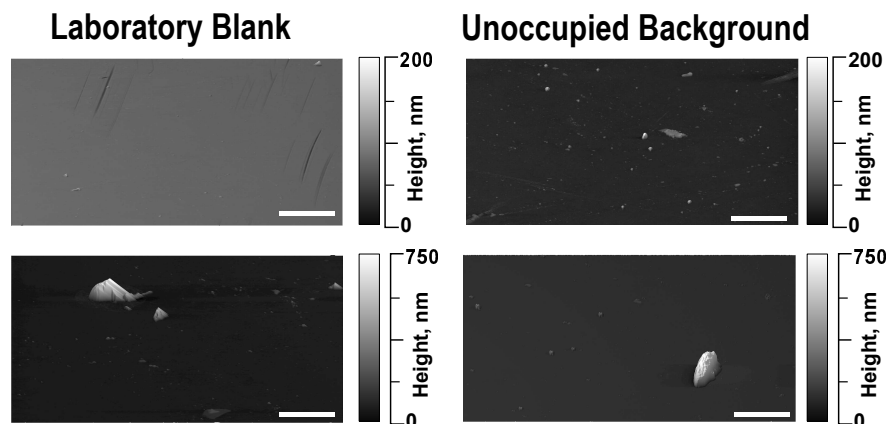


Figure S6.3: 3D AFM height images of the laboratory blank and unoccupied background glass slides in left and right panels respectively. The upper image is a typical image of the corresponding sample while the lower shows the images where a large supermicron particle remained deposited.

Table S6.1: Sampling Times (CDT) and Dates for each exposure period.

Event	Sampling Start	Sampling End
Unoccupied Background	June 1 (16:30)	June 3 (7:00)
Stir Fry	June 6 (08:15)	June 7 (08:25)
Thanksgiving	June 18 (07:45)	June 19 (07:30)
Chlorine Cleaning	June 7 (08:25)	June 8(08:15)
Terpene Cleaning	June 5 (08:15)	June 6 (08:15)

^a R_q : root mean square roughness (eqn 6.6).

^b ΔSA : change in surface area (eqn 6.4).

^c $z_{eq, film}$: film equivalent thickness (eqn 6.5).

^d θ : surface coverage by deposited material taller than 2.0 nm in height (eqn 6.7)

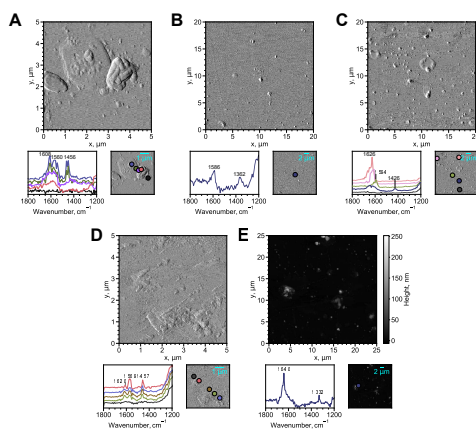


Figure S6.4: AFM-IR spectra and the corresponding AFM images (with color marked locations) of deposited particles from the stir fry event. In each panel shown, the upper image is the AFM image, with corresponding color spectra and the same AFM image with corresponding color markers showing spectra position below in the bottom left and right subpanels respectively.

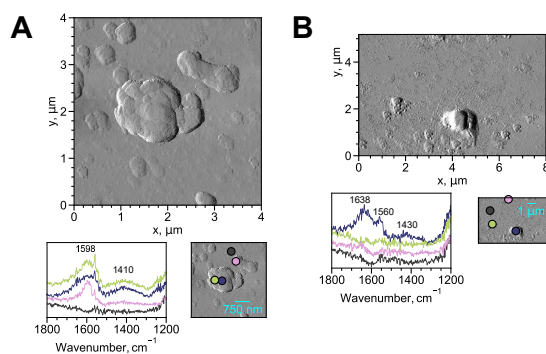


Figure S6.5: AFM-IR spectra and the corresponding AFM images (with color marked locations) of deposited particles from the Thanksgiving event. In each panel shown, the upper image is the AFM image, with corresponding color spectra and the same AFM image with corresponding color markers showing spectra position below in the bottom left and right subpanels respectively.

Table S6.2: A comparison of the surface properties of the laboratory blank and unoccupied background with the image containing the supermicron particle shown in Figure S6.3 excluded from analyses. The uncorrected surface properties from Table 6.1 are included in the lower half of the table for comparison.

Event	^a R_q , nm	^b ΔSA , μm^2	^c $z_{eq, film}$, nm	^d θ , %
Laboratory blank _{corr}	3.1(4.1)	0.6(0.6)	0.2(0.2)	1.4(0.4)
Unoccupied background _{corr}	2.9(0.6)	0.9(0.3)	0.4(0.2)	6.4(4.1)
Laboratory blank	6.0(8.5)	1.0(1.2)	0.4(0.7)	1.8(1.2)
Unoccupied background	7.8(13.2)	1.4(1.2)	0.8(1.2)	6.0(3.9)

^a R_q : root mean square roughness (eqn 6.6).

^b ΔSA : change in surface area (eqn 6.4).

^c $z_{eq, film}$: film equivalent thickness (eqn 6.5).

^d θ : surface coverage by deposited material taller than 2.0 nm in height (eqn 6.7)

Chapter 7

Water uptake on glass surfaces exposure to indoor cooking activities: Comparison to model systems

7.1 Abstract

Water uptake into thin organic films and organic particles on glass substrates at 80% relative humidity (RH) was investigated using Atomic Force Microscopy - Infrared (AFM-IR) spectroscopy. Glass surfaces exposed to kitchen cooking activities show a wide variability of coverages from organic particles and organic thin films. Water uptake, as measured by changes in volume of the films and particles, was also quite variable, showing for particles present a dependence on size. A comparison of glass surfaces exposed to kitchen activities to model systems shows that they can be largely represented by oxidized oleic acid and carboxylate groups on long and medium chain fatty acids. Overall, we demonstrate that organic particles and thin films that cover glass surfaces can take up water under indoor relevant conditions but that the water content is not uniform. The

heterogeneity of the changes in these aged glass surfaces under dry (5% RH) and wet (80% RH) conditions is quite marked. Overall, measurements such as the ones show here highlight how heterogeneous these surfaces are on the nano and micro-scales, length scales needed to understand molecular-level details of chemical partitioning and surface chemistry in indoor environments.

7.2 Introduction

There is growing interest in how indoor environments act as exposure sites for disease, irritants, and other health hazards. [225, 26, 174] Recent efforts have been directed towards developing a comprehensive understanding of processes relevant to indoor spaces.[26, 190, 226, 27] There are distinct indoor spaces with varying emission sources and activities[160, 191, 227, 66], ventilation rates[58] and building materials[228, 229], which indicates different micro-environments present indoors. Within this framework, it is recognized that the fundamental chemical and physical processes that occur indoors span a broad range of temporal, spatial, and size scales.[190, 27, 2] There is increased efforts toward understanding fundamental molecular level processes that occur in indoor spaces.

Understanding air quality indoors involves resolving the multitude of dynamic processes that influence the composition of indoor air. Indoor air quality is determined by the production and emission[190, 160, 191, 66, 67], transport[191, 162], and transformation [227, 230, 159, 179, 231, 224] of trace gases and particulate matter. Contributions arise from outdoor air mixing with direct emissions from indoor activities and sources, which can be episodic from activities like cooking and cleaning[191, 66, 67, 65] or persistent like off-gassing from building materials.[232, 233, 234] Primary emissions can react with a wide array of oxidants that can infiltrate from outdoors such as ozone[235], or produced indoors such as hydroxyl radical[168], HOCl[176], and HONO[180]. The concentrations of many

indoor species are influenced by the presence of surfaces, which act as a both sources of removal and sites for transformations. Accurately estimating the lifetime and concentrations of compounds in indoor air requires integrating an understanding of surfaces and their impacts on distinct indoor processes.

Surfaces form the basis of indoor spaces and more prevalent in indoor spaces, with a typical surface area to volume ratio of 3 m^{-1} [236], comprising a larger fraction of the overall space. Surface influences span across all ranges of physical and chemical processes, acting as a sink for particulate matter losses[75, 178, 237], partitioning of gaseous compounds[66, 9, 8, 183], and reaction sites for formation of new species through surface-mediated reactions or heterogeneous reactions with trace indoor gases.[179, 238, 189, 5, 4] The composition and structure of surfaces are highly diverse, and their evolution depends largely on location and the emission sources nearby. Modeling and field measurements have shown that over time thin films and particulate matter cover the surface.[178, 8, 56, 165] In the absence of external perturbations, these materials compounds can remain on surfaces for long periods of time, and thus enable longer timescale transformative processes than the indoor air exchange rate, the limiting time factor for most airborne reaction processes.[58, 59]1,11,44

The broad temporal and spatial scale these processes occur on make it difficult to accurately capture these processes in authentic indoor environments. On an impermeable glass surface, experimental measurements and numerical models have demonstrated lower volatility organic compounds accumulate on the surface.[178, 237, 8, 56, 165, 64] Direct analyses of surface aging can be aided by high spatial and lateral resolution analyses, as initial particle depositions can be sparse and long-term film growth is predicted to be on the order of tens of nanometers. Higher volatility compounds can reversibly adsorb onto surfaces but capturing these transfer processes often involves model system studies in laboratory settings[186, 185] or measuring loss behavior from the airborne fractions.[66] For

most analyses involving authentic surfaces, longer term exposures are more easily accessible and primarily targeting low volatility species but may mask distinct transformations from being determined.

Humidity levels are variable between and within indoor spaces, and at elevated levels water vapor can adsorb onto and or be absorbed into various surfaces and aerosols.[239, 240, 241] There are multiple sources contributing to indoor water vapor such as the humidity of outdoor air, ventilation and air conditioning, humidifiers, and water sources like faucets. Measurements and estimations of condensed water content can be appropriated from atmospheric aerosol and material surface analyses, which provide insight into aerosol and surface water content respectively. However, direct measurements of indoor aerosol water uptake are sparse. Cooking organic aerosols (COA) were found to be emitted with low hygroscopicity, but increase in hygroscopicity upon oxidation.[240] A modeling study by Cummings *et al.* used thermodynamic parameterizations of water activity to estimate the total water content contained within the indoor aerosol fraction.[241] To the authors' knowledge, in terms of indoor surfaces, similar analyses and predictions have not yet been conducted. Deposited material and adsorbed gases can hinder or compete with water for interaction sites on bare surfaces. As an impermeable surface like window glass ages, it accumulates materials that coat surfaces via gas-phase partitioning and the deposition of aerosols. Thus, as surfaces age over time, the surface water content is expected to change depending on the hygroscopicity of the accumulated material. A recent study using quartz crystal microbalance (QCM) measurements revealed that thin organic films formed on QCM sensors from kitchen activities readily uptake water at elevated RH levels.[188] However, there is a lack of studies probing the hygroscopicity of thin films and particles coating authentic indoor surfaces.

To address some of the gaps within this understanding, coatings from kitchen activities on indoor relevant surfaces, window glass, as well as laboratory generated coatings

using oleic acid (OA) and nonanoic acid (NA) were analyzed under low and elevated humidity levels using atomic force microscopy (AFM) to better contextualize surface water content and provide images/insight into how aged surfaces change over time. Results from surface measurements reveal that smaller particles take up more water relative to their size, speciation enhanced growth in medium chain fatty acids, and oxidative conditions influenced subsequent particle hygroscopicity. Functional group characterization using AFM-infrared spectroscopy (AFM-IR) demonstrates that the short term stir fry exposed glass resembled sodium nonanoate while glass surfaces exposed to the kitchen for month long timescales were a more ambiguous mixture of fatty acids, deprotonated fatty acids, and ozonolysis products.

7.3 Methods

7.3.1 Model Systems

Window glass was cut into $1 \times 1 \text{ cm}^2$ pieces and rinsed with water to remove debris. The glass surfaces were then cleaned with this alternating water and methanol rinses, followed by 1-hour soaks in water and methanol. Glass surfaces were baked in the oven at $400 \text{ }^\circ\text{C}$ for 2 hours and stored in ultrapure water (Barnsted EasyPure-II; $\geq 18.2 \text{ M}\Omega \text{ cm}$ resistivity, Thermo). Particles were generated by atomizing a 1% weight solution of fatty acid in ethanol. The resulting particles were dried by flowing through two diffusion dryers. Particles were then impacted onto glass surfaces in a micro-orifice uniform-deposit impactor (MOUDI) (NanoMOUDI-II 125R, TSI) and size selected: stage 7 (320 – 560 nm). For oxidized samples, OA was deposited on window glass and immediately transferred to a stainless-steel flow cell. The sample was then exposed to ozone under dry (<5% RH, 200 ppm, 0.5 min) or humid (80% RH, 8 ppm, 15 min) conditions respectively.

7.3.2 Field Samples

Glass samples preparation and collection in the field were discussed in detail in previous papers. Briefly, two main samples were examined: glass exposed to a simulated stir fry cooking event for roughly 24 hours during the HOMEChem campaign and window glass left exposed in a kitchen for 3 months in Austin, Texas. Samples were sealed in containers and shipped to San Diego for analyses. All samples were stored in the dark under ambient temperature, pressure, and humidity. Samples for AFM analyses were roughly $1.5 \times 1.5 \text{ cm}^2$ window glass rectangles. For gas chromatography mass spectrometry (GC-MS), a larger $25 \times 25 \text{ cm}^2$ window glass pane exposed the same time duration in the kitchen for 3 months was covered in cleaned aluminum foil for storage.

7.3.3 GC-MS Analyses

Organic thin films deposited on glass were collected using a cleaned, stainless steel, straight razor that was then washed with HPLC grade 1:1 methanol and acetonitrile (Fisher Scientific). A method blank which was comprised of the 1:1 methanol acetonitrile solvent and a clean straight razor, was used for background and peak subtraction. The samples were then immediately analyzed using GC-MS (Thermo Trace 1300/TSQ 8000 Evo Triple Quadrupole, Thermo Fisher Scientific). Using a Trace TR-5MS GC column (Thermo Fisher Scientific), a 26-min method was used to separate out the surface sorbed organics. Following a 2-minute hold period at $50 \text{ }^\circ\text{C}$, the GC oven was ramped to $330 \text{ }^\circ\text{C}$ at a rate of 15 C/min and held for 5 additional minutes. The data was analyzed using the Thermo Xcalibur software, Genesis for peak detection, and NIST-14 mass spectral database for the identification of the majority of the observed peaks

7.3.4 AFM and AFM-IR Analyses

For both AFM and AFM-IR analyses, samples were analyzed using a commercial AFM-IR system (nanoIR2, Bruker) with two tunable mid-IR laser sources, an optical perimetric oscillator laser (OPO, EKSPLA, NT-277-XIR) and a quantum cascade laser (QCL, MIRcat, Daylight Solutions). All operation using commercially available AFM probes. For AFM measurements, samples were imaged using silicon nitride tips (HQ:NSC15-AIBS, Mikromasch) with a tip radius of less than 10 nm, nominal spring constant and resonant frequencies of 40 N/m and 325 kHz respectively. To image low viscosity compounds, tapping-AFM images were collected at high set point to minimize interaction forces while being able to image water droplets. To facilitate humidity dependent measurements, samples were analyzed in a modified environmental cell. Humidity was controlled by altering the mixing ratio between dry air and air bubbled through a water cell. Relative humidity and temperature of the chamber were recorded with a sensor (SHT3x, Sensirion). Samples were imaged at approximately 5 and 80% RH levels after equilibrating for at least 10 minutes. Prior to analyses, the environmental cell sensor was calibrated using sodium chloride deliquescence (75% RH) and stage motion was calibrated using 3-dimensional array rectangular gratings (NT-MDT, TGQ1).

For AFM-IR analyses, gold coated rectangular silicon nitride tips (HQ:NSC19/Cr-Au, Mikromasch) with a tip radius of less than 30 nm, with a nominal frequency and spring constant of 65 kHz and 0.5 N/m respectively. Samples were analyzed under ambient temperature (25 °C), pressure, and humidity (15% RH). Photothermal infrared (PTIR) spectra were collected at a spectral resolution of at least 4 cm^{-1} , averaging at least 5 spectra per sample.

7.3.5 Surface and Particle Properties

Surfaces and single deposited particle properties were calculated from AFM images after processing in Gwyddion. Briefly, particles were sized according to volume equivalent diameters ($D_{eq,V}$), and particle properties such as aspect ratio (AR) and changes in volume were calculated using equations provided elsewhere.[205, 178, 242] Hygroscopic growth factors (GF) were measured by taking ratio between the volume equivalent diameters at dry (5% RH) and wet (80% RH) conditions:

$$GF(RH) = \frac{D_{eq,V}(RH)}{D_{eq,V}(Dry)} \quad (7.1)$$

Single particle water uptake can be parameterized using κ -Köhler theory, which describes the influence of aerosol composition and size on the water activity (a_w) of the solution, where V_s is the solute volume, and V_w is the volume of water.

$$\frac{1}{a_w} = 1 + \kappa \frac{V_s}{V_w} \quad (7.2)$$

Using AFM measured growth factors and diameters, single substrate deposited particle κ values can be calculated from the following equation:

$$\frac{RH/100}{\exp\left(\frac{4\sigma_{s/a}M_w}{RT\rho_w D_{eq,V}(Dry)GF}\right)} = \frac{GF^3 - 1}{GF^3 - (1 - \kappa)} \quad (7.3)$$

where T is temperature, R is the universal gas constant, $\sigma_{s/a}$ is the surface tension, M_w is the molecular weight of water, and ρ_w is the density of water.

7.4 Results

7.4.1 Hygroscopicity of Kitchen and Cooking Particles Deposited on Glass

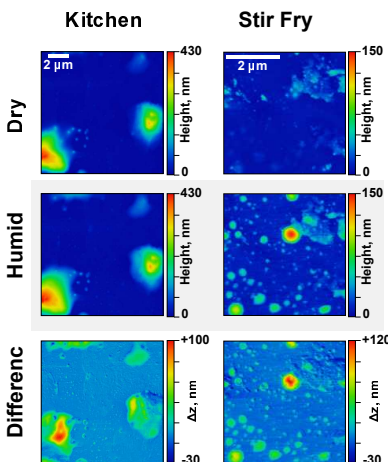


Figure 7.1: AFM height images of organic films and organic particles on window glass after 3 months exposure in a residential kitchen (left) and a single day of simulated stir fry cooking (right). Images were collected at dry (5% RH, upper) and humid (80% RH, middle) conditions, and difference images (bottom) between the two reveal regions of the surface that grew due to water uptake.

Shown in Figure 7.1 are representative AFM images of deposited particles from 3-month exposure in kitchen and a single simulated stir fry event at low and high humidity levels. Thin films form and particles deposit over time on glass surfaces from kitchen emissions, which are rich in low- to semi-volatile hydrophobic organic compounds such as aldehydes and long chain fatty acids.[65] Differences between images collected under dry (upper) and humid (middle) conditions are used to determine interactions of coated indoor surfaces with water vapor, where regions of increased height are indicative of water uptake. Hygroscopic growth of particles and films is observed in both the kitchen and stir fry exposed glass, where changes in surface morphology is most prevalent for deposited particles. In the stir fry exposed glass, deposited particles were predominantly submicron sized and flat[242], with water uptake transforming the particles into larger more hemi-

spherical droplets. In the 3-month exposed kitchen glass, small particles behaved similarly in response to high relative humidity (Figure S7.1). However, longer exposed kitchen glass samples contained a relatively higher fraction of supermicron sized particles. In these larger sized particles, difference images reveal that water uptake is more prevalent at the particle edges.

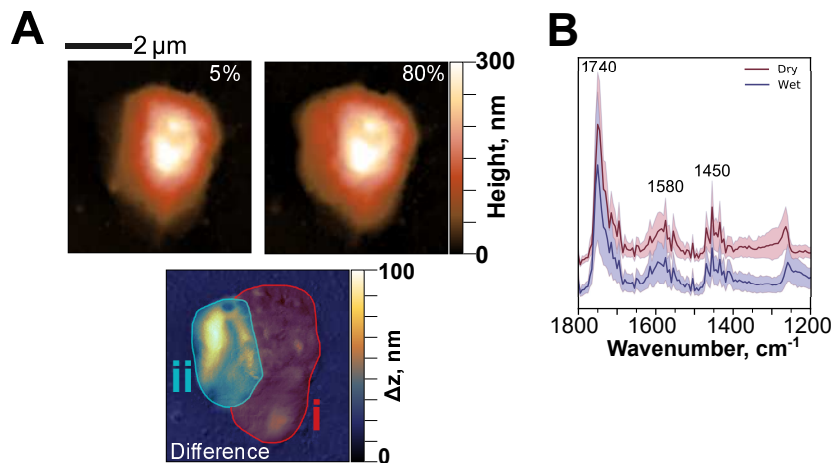


Figure 7.2: AFM images of two particles from the kitchen glass in panel A) at dry and humid conditions, with difference images masked to highlight regions where water was prevalent. (i) and regions that did not grow (ii). PTIR spectra collected at 10% RH taken in the corresponding regions are shown in panel B, with solid and shaded regions indicating the average and one standard deviation respectively.

To examine if chemical heterogeneities correlated with difference in water uptake throughout the particle, AFM-IR spectra were taken across the larger particles deposited on kitchen glass. Two different particles from the kitchen exposed glass shown in Figure 7.2 with AFM height images in panels A) and C). Difference images were used to determine which regions of the particle grew the most upon exposure to elevated RH levels, and correspondingly, spectra were taken in regions that grew (wet) or remained static (dry) and plotted in panels B and D. In both particles shown, there is no noticeable or significant differences between the measured regions as detected by AFM-IR, the particles are largely homogeneous in IR active functional groups, with major modes observed at 1740, 1580, and 1450 cm^{-1} , corresponding to $\nu(\text{C}=\text{O})$, $\nu_{as}(\text{COO}^-)$ and $\nu_s(\text{COO}^-)$ respectively.[216]

7.4.2 Spectral Comparisons with Laboratory Generated Model Systems

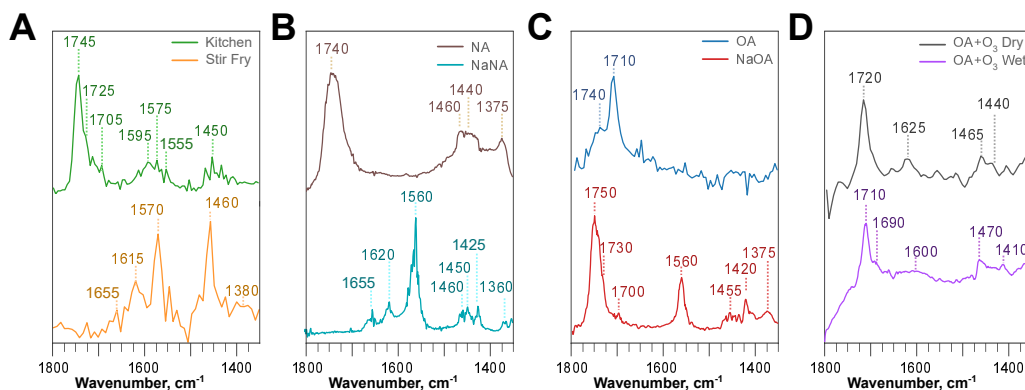


Figure 7.3: PTIR spectra of the particles coating A) kitchen and stir fry glass surfaces and various model systems for comparison: B) nonanoic acid (NA) and sodium nonanoate (NaNA) C) oleic acid (OA) and sodium oleate (NaOA) and D) oleic acid oxidized under dry and humid conditions

Comparison of functional composition of particles deposited on the stir fry and kitchen exposed glass is shown in Figure 7.3. AFM-IR was used to compare various fatty acids proxies based on oleic acid, sourced from cooking oils and various vegetable and animal products, and one of the most abundant emissions found during cooking events. Oleic acid (OA) is an unsaturated C16 fatty acid, with a low volatility, and expect to interact and remain on surfaces. The double bond makes it susceptible to reactivity leading to formation of secondary products with indoor oxidants, such as ozone [243, 244, 245, 246] which can be produced indoors or infiltrate from outdoor air mixing.[235] Nonanoic acid (NA) is one of the major oleic acid ozonolysis products, similar in structure just shorter C9 monocarboxylic acid. In addition, spectra of sodium salts of both oleic (sodium oleate, NaOA) and nonanoic acid (sodium nonanoate, NaNA) are included, as altered speciation of chain fatty acids has been shown to alter water solubility[247] and is expected to be more pronounced in medium to short chain fatty acids. Spectrally, the particles from the stir fry event correspond with NaNA, with most prevalent vibrational modes around 1570, 1560

and 1460, 1450 cm^{-1} corresponding to $\nu_{as}(\text{COO}^-)$ and $\nu_s(\text{COO}^-)$ respectively. Aging and ozonolysis of particles and films covering a glass after three weeks of exposure throughout the HOMEChem campaign found that C=C bonds were still present and susceptible to further oxidation,[248] and these moieties are expected around 1650 cm^{-1} and subsequently would spectrally overlap with the carboxylate modes observed.

In the kitchen deposited particles, modes are present around 1740, 1580, and 1450 cm^{-1} , corresponding to $\nu(\text{C}=\text{O})$, $\nu_{as}(\text{COO}^-)$ and $\nu_s(\text{COO}^-)$ respectively. The presence of these modes suggests a mixture of deprotonated carboxylic acids in addition to protonated carboxylic acids or molecules containing other carbonyl moieties. The spectral features match with mixtures of the sodium carboxylate salts and various OA/NA systems shown, however FTIR spectra alone are insufficient for making this comparison difficult, as many of the products formed from ozonolysis or uptake of additional fatty acids/carbonyl containing compounds such as aldehydes overlap in this region. Adding additional complexities, for the long-term exposed kitchen samples, we do not expect chemical composition to fully match due to other emission sources beyond cooking, as well as uptake of passive emissions such as degassed low volatility organic compounds (i.e. phthalates), which contain C=C and carbonyl moieties that overlap in the same spectral regions. A list of the compounds detected from surface extracts via GM-MS is provided in Table S7.1. Most of the compounds detected were carbonyl containing organic compounds, along with a few other indoor relevant compounds such as siloxanes and phthalates. However, many of the major spectral features are captured with a few model molecular systems. Of particular interest, the shorter-term stir fry samples are predominantly characterized by deprotonated carboxylate species, of higher water solubility. Formation of medium chain fatty acids such as nonanoic acid can be attributed to ozonolysis of oleic acid reacted prior to deposition. NA can be attributed to formation from ozonolysis of oleic acid reacted prior to deposition, however, the source of the deprotonated carboxylate species is currently unexplained.

7.4.3 Hygroscopicity of Model Systems

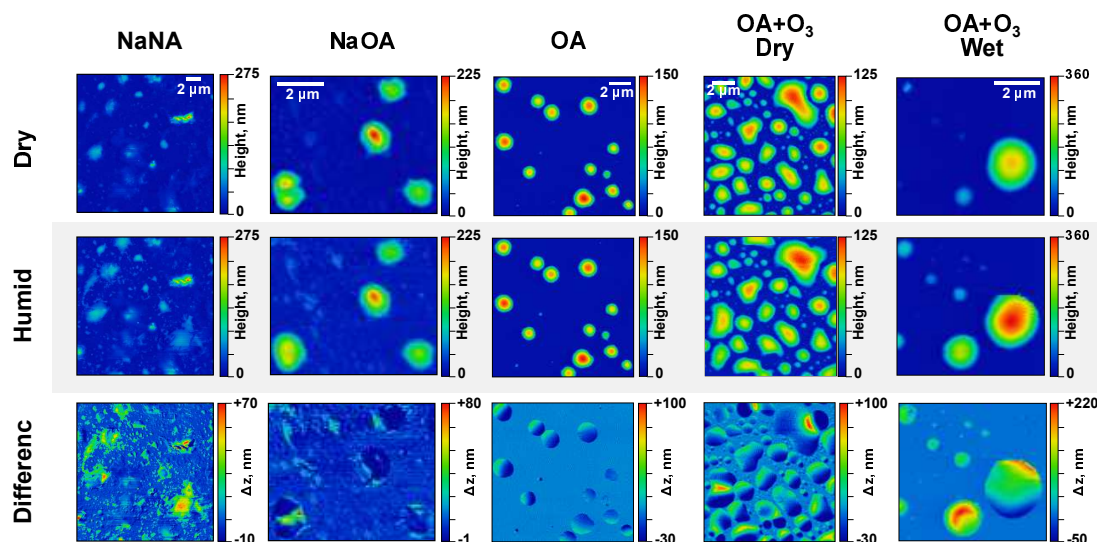


Figure 7.4: AFM height images of model system particles on window glass from left to right: sodium nonanoate (NaNA), sodium oleate (NaOA), oleic acid (OA), oleic acid oxidized under dry conditions (OA + O₃ dry), and oleic acid oxidized under humid conditions (OA + O₃ wet). Images were collected at dry (5% RH, upper) and humid (80% RH, middle) conditions, and difference images (bottom) between the two reveal regions of particles that grew from water uptake.

A comparison of the hygroscopic growth of model systems with AFM is shown in Figure 7.4 with representative images shown for each system. For oleic acid, there no noticeable change in particle morphology or size, beyond thermal drift slightly shifting the location of the particle, which is expected for a hydrophobic system. Oleic acid oxidized under dry conditions are irregularly shaped with some hygroscopic growth at edges between particle, creating liquid capillary bridge between particles. However, beyond these capillary bridges, minimal water uptake is observed. This is consistent with past studies involving oleic acid oxidized under dry conditions, wherein primary ozonolysis products do not significantly enhance hygroscopicity. Under extended exposure to ozone, oleic acid undergoes further fragmentation, forming more water-soluble secondary products that improve hygroscopicity^{64,65}, however, the low hygroscopicity of particles in this

study suggest these more hygroscopic products have not formed. To examine reversibility of liquid bridges between particles in regions densely coated with particles. 3D AFM height images shown in Figure S7.2, where particles were dried out. Transitioning from wet to dry, water capillary between the neighboring particles disappears and distinct particles remain. At the humidity levels examined, liquid water capillaries between densely coated hydrophobic particles on glass do not result in particle coalescence, but rather particles remain separated distinct particles on surface upon drying.

Oleic acid oxidized under wet conditions are noticeably more hygroscopic, growing with elevated RH. The presence of water in this reaction alters the reaction mechanism, providing an alternative pathway wherein the Criegee intermediate can react with water to form hydroxyhydroperoxides and subsequently decompose into carboxylic acids or aldehydes. For the sodium oleate salt, particles are deposited with a more irregular shaped morphology. Upon exposure to high RH levels, there is not much growth, with marginal uptake at the edges. Decreasing chain length, the sodium salt of nonanoic acid is much more hygroscopic, where deposited thin irregular-shaped particles readily uptake water.

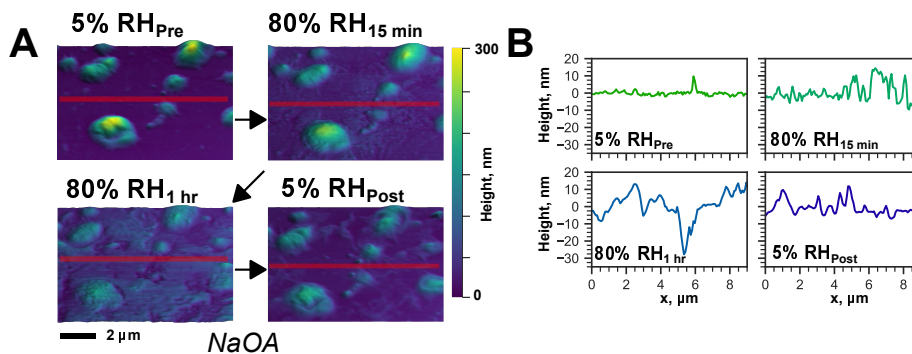


Figure 7.5: A) 3D AFM height images of sodium oleate particles on kitchen glass before, during, and after exposure to elevated RH levels, with corresponding height profiles at the indicated lines in panel B). Slight changes in morphology are present after 15 minutes of exposure, followed by the formation of water films on the glass surface after 1 hour. After extended exposure, sodium oleate particles are more spread across the glass surface.

While sodium oleate particles did not readily uptake water, sodium oleate coated

glass behaved differently from oleic acid or its ozone reacted products. Extended exposure of the NaOA system resulted in a thin water film coating the surface, as shown in Figure 7.5, which was not present in the oleic acid or oxidized oleic acid coated glass surfaces. 3D AFM height images shown in panel A) with corresponding height profiles at the marked lines in panel B) for exposure of NaOA coated glass. Transitioning from dry to humid conditions at 15 min and 1 hour, water uptake is apparent at 15 min, with slight particle growth. However, extended exposure at 80% RH results in the glass surface being covered with a film of water. Upon dehumidifying, particle morphologies and surface coverage changes, spreading out particles partially into coating the surface with a approximately 10 nm thick structure. For more water-soluble systems, this restructuring by water films can spread particles across surfaces, providing a possible mechanism for formation of thin films of water-soluble organics from particle deposition.

7.4.4 Comparison of Hygroscopic Growth on Glass Surfaces: Kitchen Exposed Samples and Model Systems

A statistical summary of the hygroscopic response for each of the different glass surfaces including kitchen exposed surfaces and model system exposures is shown in Figure 7.6, with scattered boxplots with listed mean and standard deviations for growth factors and hygroscopicity parameter kappa. Numerical values for growth factors and kappa values are provided in Table 7.1, with particles separated into 500 nm size bins. Oleic acid and its dry ozonolysis products as expected do not take up much water with kappa values of 0.02 ± 0.07 and 0.05 ± 0.18 respectively. Wet ozonolysis enhances hygroscopicity due to fragmentation into lower chain more hygroscopic carboxylic acids, resulting in an increase in the AFM measured kappa value to 0.17 ± 0.26 , overlapping reasonably with the kitchen deposited particles which had a kappa of 0.19 ± 0.22 . Relative to oleic acid, there is no noticeable change in hygroscopicity for its sodium salt, which had a low kappa value of 0.01

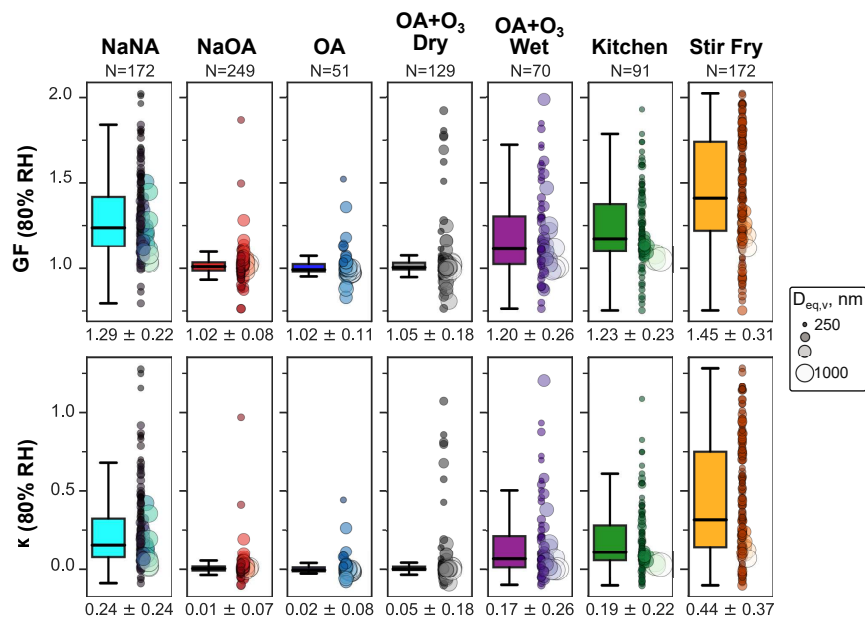


Figure 7.6: Scatter box plots of the hygroscopic growth factors (upper) and corresponding κ values (lower) for single particles from AFM measurements. Scatter points are roughly scaled according to particle diameters and box plot lines are set to the 5th and 95th percentiles. The total number of particles analyzed per system is provided at the top of the plots, with average \pm standard deviation listed below. Systems shown from left to right are: sodium nonanoate (NaNA), sodium oleate (NaOA), oleic acid (OA), oleic acid oxidized under dry conditions (OA + O₃ dry), oleic acid oxidized under humid conditions (OA + O₃ wet), 3-month exposure in a residential kitchen, and one day of stir fry cooking.

± 0.07 . While salts enhance solubility, this behavior is consistent with previous studies of NaOA, which observed that growth factors of aerosolized particles were not observed to be above unity until 85 -90% RH. Sodium nonanoate however is more hygroscopic. Even though nonanoic acid has not been found to enhance hygroscopicity, in the sodium salt, we observe enhanced growth from water uptake, with a kappa value of 0.24 ± 0.24 . This matches reasonably well with the stir fry deposited particles on glass which were the most hygroscopic system with a kappa value of 0.44 ± 0.37 . To the authors knowledge, studies targeting the hygroscopic growth of isolated sodium nonanoate or nonanoic acid particles are not available. However, the deprotonation medium chain length fatty acids is expected to readily enhance solubility. Spectral features indicate that these sodium

Table 7.1: Numerical values for the AFM measured hygroscopic growth factors and κ values in roughly 500 nm size bins, with values listed as average (standard deviation). Size bins with no particles detected are indicated with a dash (-).

$D_{eq,V}$, nm	GF			κ		
	< 500	500-1000	>1000	< 500	500-1000	>1000
NaNA	1.30(0.23)	1.20(0.15)	-	0.25(0.25)	0.14(0.13)	-
NaOA	1.02(0.08)	1.02(0.02)	-	0.01(0.07)	0.01(0.01)	-
OA	1.06(0.07)	1.00(0.08)	0.98(0.01)	0.04(0.04)	0.01(0.03)	-
						0.01(0.01)
OA O ₃ Dry	1.10(0.26)	1.01(0.06)	1.01(0.02)	0.10(0.26)	0.01(0.03)	0.01(0.01)
OA O ₃ Wet	1.22(0.28)	1.15(0.15)	1.03(0.08)	0.20(0.28)	0.10(0.12)	0.02(0.04)
Kitchen	1.24(0.24)	1.11(0.03)	1.07(0.02)	0.20(0.23)	0.07(0.02)	0.04(0.01)
Stir Fry	1.46(0.31)	1.16(0.05)	-	0.44(0.37)	0.10(0.04)	-

nonanoate particles are deprotonated on the surface and there is no evidence for COOH, i.e. protonated moieties present. In contrast, in the sodium oleate particles, we observe a distinct 1750 cm^{-1} mode, which is likely due to ambient oxidation of the C=C bond in NaOA, resulting in the formation of carbonyl group moieties.

In all the glass surface coatings examined, we observe higher hygroscopic growth in the smaller sized particles, but in these same size bins, the lowest growth factors are also observed. The larger variances in these smaller sized particles are likely attributed to higher sensitivity of these smaller volume particles to any uptake and chemical heterogeneity within the sample. Correspondingly, growth factors under unity (corresponding $\kappa < 0$), are likely due to evaporation of material throughout the analyses. Deposited particles are thin and flat, as indicated by the low aspect ratios (Figure 7.7), but direct comparisons between model systems and authentic glass coatings cannot be made due to the differences in sample preparation. With increasing particle size, AFM measured hygroscopicity tended to decrease, with growth factors closer to 1. However, in comparison to studies that aerosolized particles, the AFM measured hygroscopicity was typically higher than those measured in the airborne fraction.[240, 244] There is likely an interplay between surface

effects, speciation, and oxidation in altering the hygroscopicity of the deposited or adsorbed materials.

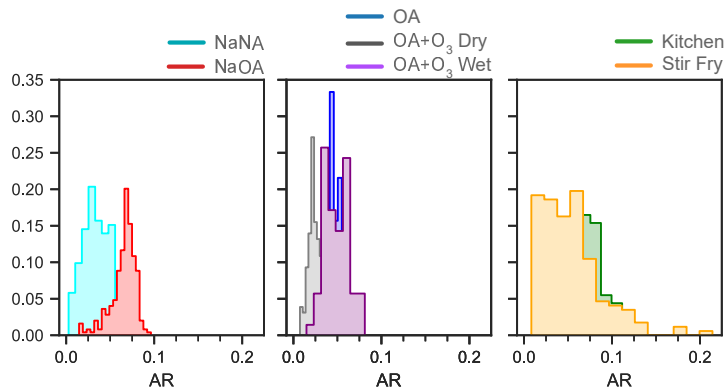


Figure 7.7: Relative abundance histograms of the aspect ratios (AR) for the particles deposited on each of the coated window glass samples. Smaller aspect ratios (closer to zero) correspond with a higher degree of spreading and flatter particles.

7.4.5 Hygroscopic Behavior of Indoor Organic Films

Experimental and numerical models have demonstrated that organic-rich thin films readily coat glass surfaces in indoor spaces, forming and get thicker over long timescales.[8, 64, 56] For kitchen glass, previous studies have found that thin films are prevalent, and largely coat surfaces. The hygroscopic response of films on window glass are shown in Figure 7.8. With increasing relative humidity, the two representative images shown reveal differing responses, water absorption throughout the film (Area-1, panel A) and droplets forming on the surface (Area-2, panel B). Height profiles are shown in the bottom panel, however, due to the lack of a substrate presence in film locations, there is no relative zero height from the underlying glass to accurately assess changes in film thickness upon homogeneous water uptake. Subsequently, water uptake is not readily quantifiable from AFM measurements. However, the qualitative hygroscopic behavior of indoor organic films is consistent with past experimental results. Schwartz-Narbonne and Donaldson demonstrated that organic films formed in kitchen environments on gold-plated quartz

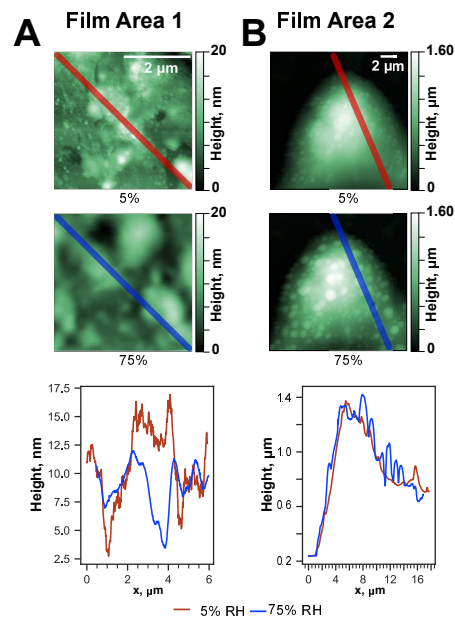


Figure 7.8: AFM height images of the A) middle of a film and B) edge of a film at dry (upper) and humid (middle) conditions respectively, with height profiles (lower) collected along the marked lines. The middle of the film (Area 1) demonstrates more uniform water uptake throughout the imaged region, whereas the edge (Area 2) demonstrates a region where droplets collected on the surface of the film.

crystals readily uptake water at similar humidity levels, as detected by QCM.[188] While the surface materials differ, and gold-plated surfaces are not necessarily common in most indoor settings, these results agree that indoor surfaces coated with organic rich films and particles readily uptake water at elevated humidity levels. However, it is difficult to determine the spatial variation of water uptake with QCM as shown here using the nanoscopic probe of the AFM tip.

7.4.6 Implications for Water Content of Indoor Surfaces

The measurements shown here for organic films and particles on glass surfaces formed from exposure to cooking activities provides new insights into the impact of relative humidity on the interaction of these films and particles. These nanoscopic measurements shown here indicate that the condensed water on the surface is not evenly distributed

throughout the surface and is instead concentrated at particles and the film. As these particles and films take up water at elevated RH, expect a transition to lower viscosity phase states, altering gas-surface processes including mass transport and diffusion-rates. There is large variability in hygroscopic growth of submicron sized particles for both kitchen and cooking exposed surfaces and the model systems. The presence of particles is much more prevalent on the short-term window glass exposed to stir fry cooking. Even within a single system, there is evidence of size dependent variability. Smaller particles had a greater water content either due to composition or their interactions with the substrate, due to the flat nature of the particles and presence of a hydrophilic substrate such as window glass. While the larger sized particles were relatively less hygroscopic, they still grew enough with elevated RH to where they were much more influential in altering the surface volumes of condensed water (Figure S7.3) even with their lower abundance by number.

Past studies have shown that these submicron sized particles were covering glass surfaces from cooking events, and that under shorter time scales, these deposited particles on glass surface primarily contribute to modifying surface water content. As surfaces are exposed indoors for longer, additional particles deposit and gases adsorb leading to formation and growth of indoor films, which have been previously observed on glass surfaces from the kitchen for multiple months.[178, 56] Particles deposited on the kitchen glass was seen to take up water at elevated RH levels indicating these organic rich films and particles still are a source of condensed water indoors, but to a lesser extent than the short-term particles from stir fry cooking. This change in hygroscopic behavior suggests uptake or accumulation of less hygroscopic material over time. Even on these longer-term exposed glass samples, films were not uniform with respect to the coverage of organics and surfaces are heterogeneous.

One advantage of AFM-IR technique is preservation of the structure and integrity of

the surface, allowing for analyses without the need to extract material off the surface. This enables studies that retain the heterogeneity of these surfaces and any surface influences on composition and speciation. In this study, through nanoscale PTIR spectra, we find that the speciation of medium chain fatty acids alters the hygroscopic behavior of deposited material on glass surfaces. Deprotonated carboxylic groups comprise the predominant spectral features, especially in particles from a single day of stir fry cooking and nonanoate, the deprotonated form. Deprotonation of carboxylic acids enhances solubility, and this influence from speciation becomes more pronounced with decreasing chain length. Medium chain fatty acids such as nonanoic acid can be sourced from ozonolysis or fragmentation of unsaturated fatty acids. However, the role of surface acidity and speciation of particles and films have not been thoroughly explored in respect to indoor surfaces.

7.5 Acknowledgements

Chapter 7 in part is currently prepared for submission for publication of the material. **Victor W. Or**, Michael R. Alves; Michael Wade, Sarah Schwab, Richard L. Corsi, Vicki H. Grassian. The dissertation author is the primary investigator and author of this material This material is based upon work supported by the Alfred P. Sloan Foundation under grants G-2020-12675 (VHG). The dissertation author was the primary investigator of all microscopy measurements and data analysis. We acknowledge Michael Wade from Professor Richard Corsi's group for preparing and collecting field samples and transporting them to UC San Diego. The author would also like to thank Michael Alves from Professor Vicki Grassian's group and Michael Wade from Professor Richard Corsi's group for providing GC-MS analyses and results.

7.6 Supporting Information

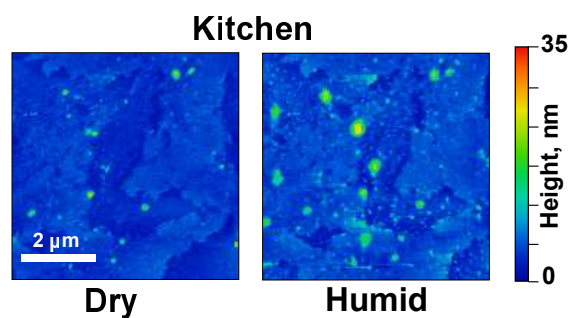


Figure S7.1: AFM height images of a thin film region of the kitchen window glass under dry and humid conditions

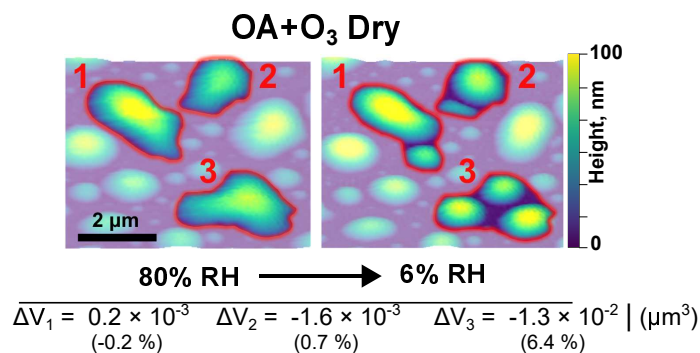


Figure S7.2: 3D AFM height images at 80% (left) and 6% (right) RH of oleic acid particles reacted with ozone under dry conditions. Three representative particles with liquid bridges are outlined in red, with the substrate and other particles set at a higher transparency for visualization. Changes in volume upon drying are given below the image.

Table S7.1: Most abundant compounds (25) as detected by GC-MS from material extracted from window glass exposed to the kitchen for 3 months. Compounds are listed in order of relative abundance, with retention times (RT) included.

	RT, min	Compound	Area, a.u. ($\times 10^8$)	% Area
1	25.60	tri-laurin	7.34	11.37
2	15.32	n-hexadecanoic acid	1.55	2.40
3	14.36	2-cis-3-octadecenyloxyethanol	1.55	2.40
4	8.13	nonanal	1.36	2.11
5	12.37	dodecanoic acid	1.15	1.79
6	18.75	diisooctyl phthalate	1.09	1.69
7	23.84	3-(octanoyloxy)propane-1,2-diyl bis(decanoate)	0.87	1.36
8	19.80	terephthalic acid, bis(2-ethylhexyl) ester	0.67	1.04
9	16.48	trans-13-octadecenoic acid	0.62	0.97
10	22.54	glycerol tricaprylate	0.60	0.94
11	9.71	nonanoic acid	0.50	0.77
12	13.85	1,3-di-iso-propylnapthalene	0.47	0.74
13	21.78	1,2-dilaurin	0.34	0.53
14	8.72	octanoic acid	0.26	0.42
15	19.49	octocrylene	0.26	0.41
16	10.64	decanoic acid	0.20	0.32
17	17.43	glycidyl palmitate	0.19	0.31
18	20.13	didecan-2-yl-phthalate	0.18	0.29
19	11.13	dodecanal	0.16	0.26
20	20.07	squalene	0.14	0.22
21	20.75	lauric acid, hexadecyl ester	0.14	0.22
22	11.25	tetradecamethyl-cycloheptasiloxane	0.14	0.21
23	11.77	oleic acid (Z)	0.11	0.18
24	13.90	myristic acid	0.10	0.17
25	12.56	hexadecamethyl-cyclooctasiloxane	0.03	0.06

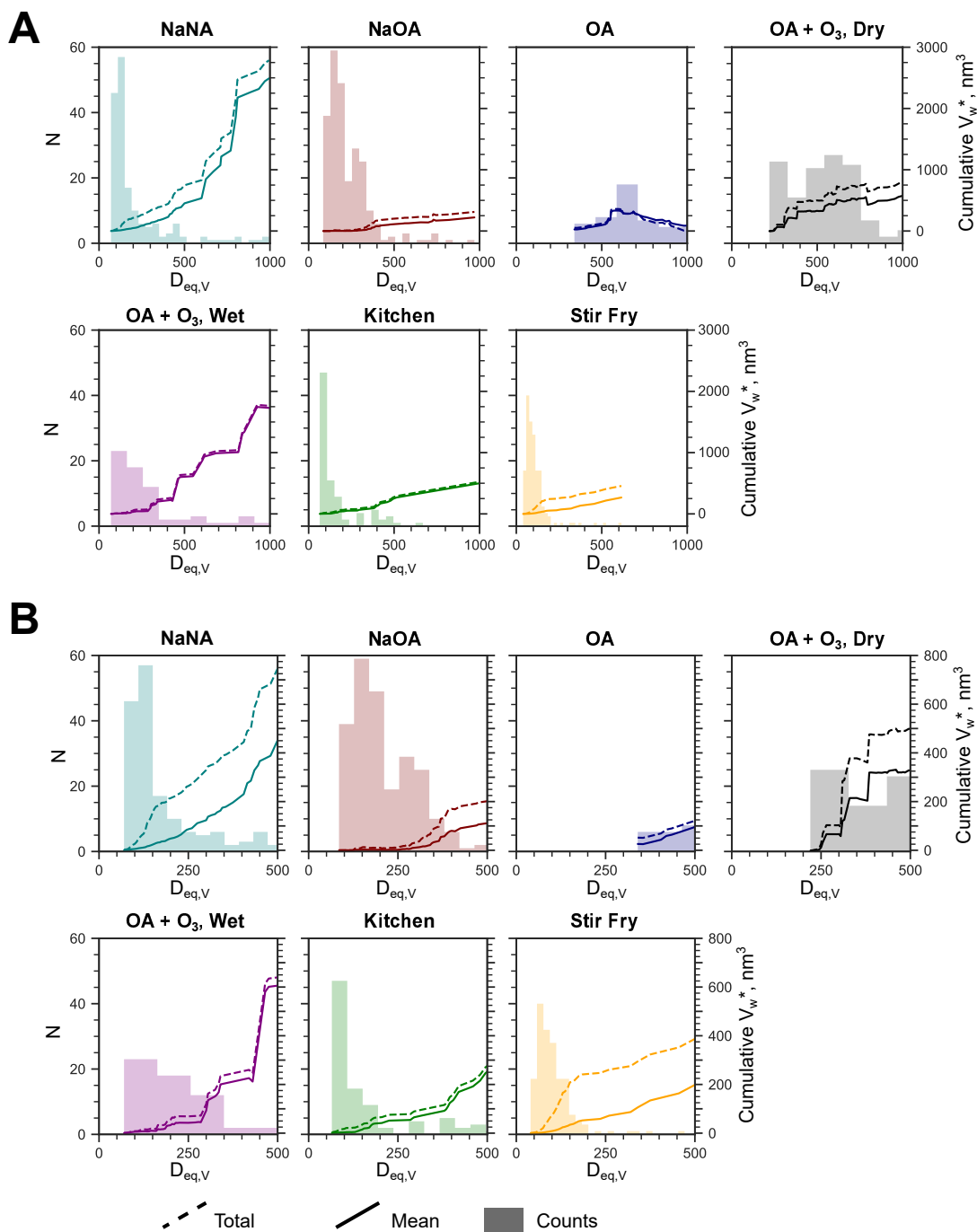


Figure S7.3: Size distributions (shaded bars) of deposited particles ($D_{eq,V} \leq 1\mu m$) for each of the glass surfaces with corresponding cumulative mean (filled) and total (dashed) contributions to changes in volume ($V_w^* = V_{80\%RH} - V_{5\%RH}$) at elevated RH. B) Zoomed in plot focusing on particles under 500 nm.

Chapter 8

Conclusions and Future Perspectives

The overall goal of this dissertation was to study the surface properties and composition of relevant environmental surfaces using nanoscale resolution spectromicroscopic techniques. Chapter 3 details the development of the technique for studying substrate deposited aerosol particles is demonstrated using model systems of various systems comprised of organic-inorganic atmospherically relevant mimics. These studies demonstrated atomic force microscopy-infrared spectroscopy (AFM-IR) can be utilized to study the composition of substrate deposited aerosol particles on relevant size regimes, down to tens of nanometers. Moreover, we demonstrate that the high resolution spectroscopic information from using the tip as a near-field detector can be used to examine chemical heterogeneities of nanoscale phase separations under ambient conditions. The technique is then applied towards the analyses of authentic sea spray aerosols in Chapter 4, examining the composition of various morphologies collected throughout a microbial bloom, where AFM-IR spectra provides chemical context for the range of morphologies observed.

There are many interesting questions and opportunities for the application of AFM-IR in analyses of substrate deposited aerosol particles. Although we have demonstrated the application of the technique for field and model aerosols, there has not been rigorous

application of the technique for probing some of the phase separations of various mixed organic-inorganic or organic-organic model systems. Examining the composition and water uptake at the phase separation could provide insight into the chemical interplay between the phase separated species. Coupling humidity dependence into these measurements can be utilized to better understand the influence of the phase separation on climate relevant properties such as hygroscopicity and ice nucleation.

Much of the work presented in this thesis was conducted using an optical parametric oscillator (OPO) laser, which is significantly slower and overall had a lower sensitivity relative to higher repetition lasers such as a quantum cascade laser (QCL). Use of higher throughput tunable IR lasers would allow for more robust statistical information by reducing experiment time and improve the quality of spectra, enabling studies with larger more accurate datasets. These larger scale measurements would be more useful for high complexity systems such as those collected during field or mesocosm campaigns, and, if sufficient in size, can potentially be used in developing sophisticated image characterization techniques such as sparse representation classification or training classification models with machine learning.

This dissertation highlights some of the key information that AFM and AFM-IR can provide for the growing field of indoor surface chemistry. On impermeable surfaces, many of the changes due physical and chemical processes involving the surface spatially fall between the nanometer to micrometer size regimes. We demonstrate that the accumulation of material onto glass surfaces is not as uniform as previously hypothesized and proposed. Chapter 5 demonstrates that glass surface evolution is largely driven by the indoor environment and its located in that space as well as the corresponding emission sources. The majority of material coating the surface is in the form of distinct particles, which is enhanced in locations with low ventilation, such as a garage. Film formation is not uniform, but predominantly observed in the glass sample placed in a kitchen for multiple

months. These films are largely comprised of carbonyl containing moieties, as detected by AFM-IR. However, as detailed in Chapter 6, samples collected during the HOMEChem campaign reveal that after a single day cooking or cleaning events these initial surfaces are largely coated by submicron sized particles. Spectra from these particles show the presence of deprotonated carboxylate groups, but no vibrational modes associated with protonated carboxylic acids or carbonyls are observed. In Chapter 6, these coatings on window glass were examined as a function of relative humidity, wherein particle growth using AFM was used to measure the hygroscopicity of indoor surfaces. We demonstrate that much of the behavior of these field exposed glass samples can be encapsulated in a few model system mimics, namely sodium nonanoate for the single day cooking and oleic acid reacted with ozone under humid conditions for the month-long kitchen glass. The differences in physiochemical properties and composition between these timescales highlights the dynamic and complex nature of surfaces as simple as window glass.

There are still many questions regarding the temporal evolution of glass surfaces. We have demonstrated that there is an interplay between particle deposition and film formation. However, there is still a dearth of knowledge in the exact mechanism of how these coatings on impermeable surfaces evolve from particles to organic films. Field studies can be aided by size-resolved measurements of particle composition, to provide insight into any size-dependent trends in chemical composition, and consequently how those are reflected in surface deposited materials or films. Laboratory chamber studies exposing particle-coated window glass to various indoor emissions, ranging from particulate matter to various organic gaseous compounds. These laboratory conditions can be used to expedite the accumulation process, and monitoring surface material accumulation can potentially elucidate the different contributions various transfer mechanisms have on thin film formation.

This study also focused primarily on ozone as an aging oxidant. However, the indoor

space has a multitude of other reactive gases, including HOCl, various ClO_x species, and HONO, as well as attenuated sunlight. Thus there remain many questions on how different indoor relevant oxidative and photooxidative conditions drive the formation of new species on indoor surfaces.

Additionally, window glass is just one of many indoor surfaces that can be probed. Other relevant surfaces include but are not limited to paint, gypsum, and flooring. These surfaces have their own set of complexities when it comes to locations, physiochemical properties and potential perturbations. Some of these surfaces may be too rough for measurements using AFM, requiring the development and integration of other analytical techniques to properly probe.

This study primarily focused on the evolution of window glass in the context of material accumulation. However, arguably more interesting and impacting is understanding the release of material back from the surface. Quantifying the amount of surface material lost and either the composition of the material remaining on the surface or the material evaporated into the airborne fraction are necessary for understanding if any surface reactions or chemical transformations are detrimental to indoor air quality.

In conclusion, the findings and future work presented throughout this dissertation provide insight into the nanoscale complexities and properties of indoor and atmospherically relevant environmental surfaces. The broader reaching overall goals of these two projects were to 1) understand how morphological and chemical properties of aerosol particles influence climate relevant properties for more accurate model predictions and 2) develop a molecular level understanding of the chemistry occurring on indoor surfaces to better predict the role surfaces play in regulating indoor air quality.

Bibliography

- [1] Xiaofei Wang, Camille M. Sultana, Jonathan Trueblood, Thomas C.J. Hill, Francesca Malfatti, Christopher Lee, Olga Laskina, Kathryn A. Moore, Charlotte M. Beall, Christina S. McCluskey, Gavin C. Cornwell, Yanyan Zhou, Joshua L. Cox, Matthew A. Pendergraft, Mitchell V. Santander, Timothy H. Bertram, Christopher D. Cappa, Farooq Azam, Paul J. DeMott, Vicki H. Grassian, and Kimberly A. Prather. Microbial control of sea spray aerosol composition: A tale of two blooms. *ACS Central Science*, 1(3):124–131, 2015.
- [2] Yangdongling Liu, Ariana Gray Bé, Victor W. Or, Michael R. Alves, Vicki H. Grassian, and Franz M. Geiger. Challenges and Opportunities in Molecular-Level Indoor Surface Chemistry and Physics. *Cell Reports Physical Science*, 1(11):100256, 11 2020.
- [3] Timothy H. Bertram, Richard E. Cochran, Vicki H. Grassian, and Elizabeth A. Stone. Sea spray aerosol chemical composition: Elemental and molecular mimics for laboratory studies of heterogeneous and multiphase reactions. *Chemical Society Reviews*, 47(7):2374–2400, 2018.
- [4] M. Kruza, A. C. Lewis, G. C. Morrison, and N. Carslaw. Impact of surface ozone interactions on indoor air chemistry: A modeling study. *Indoor Air*, 27(5):1001–1011, 2017.
- [5] M. Sleiman, L. A. Gundel, J. F. Pankow, P. Jacob, B. C. Singer, and H. Destailats. Formation of carcinogens indoors by surface-mediated reactions of nicotine with nitrous acid, leading to potential thirdhand smoke hazards. *Proceedings of the National Academy of Sciences*, 107(15):6576–6581, 2010.
- [6] Gayan Rubasinghege and Vicki H. Grassian. Surface-catalyzed chlorine and nitrogen activation: Mechanisms for the heterogeneous formation of ClNO, NO, NO₂, HONO, and N₂O from HNO₃ and HCl on aluminum oxide particle surfaces. *Journal of Physical Chemistry A*, 116(21):5180–5192, 5 2012.
- [7] Devarakonda S.N. Prasad, Rani Ashu, and Krishna S. Gupta. Surface-Catalyzed Autoxidation of Sulfur(IV) in Aqueous Silica and Copper(II) Oxide Suspensions. *Environmental Science and Technology*, 26(7):1361–1368, 1992.

- [8] C. J. Weschler and W. W. Nazaroff. Growth of organic films on indoor surfaces. *Indoor Air*, 27(6):1101–1112, 2017.
- [9] Chen Wang, Douglas B. Collins, Caleb Arata, Allen H. Goldstein, James M. Mattila, Delphine K. Farmer, Laura Ampollini, Peter F. DeCarlo, Atila Novoselac, Marina E. Vance, William W. Nazaroff, and Jonathan P.D. Abbatt. Surface reservoirs dominate dynamic gas-surface partitioning of many indoor air constituents. *Science Advances*, 6(8), 2020.
- [10] Eva R. Garland, Elias P. Rosen, and Tomas Baer. The role of morphology on aerosol particle reactivity. In Raghava R. Valsara Kalliat T., Kommalapati, editor, *ACS Symposium Series*, volume 1005, pages 13–29. American Chemical Society, 1 2009.
- [11] S. Semal, T. D. Blake, V. Geskin, M. J. De Ruijter, G. Castelein, and J. De Coninck. Influence of surface roughness on wetting dynamics. *Langmuir*, 15(25):8765–8770, 12 1999.
- [12] Michael R. Alves, Yuan Fang, Kristin J. Wall, Veronica Vaida, and Vicki H. Grassian. Chemistry and Photochemistry of Pyruvic Acid Adsorbed on Oxide Surfaces. *Journal of Physical Chemistry A*, 123(35):7661–7671, 9 2019.
- [13] Zhenqian Chen, Juan Shi, Xiaozhong Shen, Qiang Ma, and Bo Xu. Study on formaldehyde emissions from porous building material under non-isothermal conditions. *Applied Thermal Engineering*, 101:165–172, 2016.
- [14] Lucas B. Algrim, Demetrios Pagonis, Joost A. de Gouw, Jose L. Jimenez, and Paul J. Ziemann. Measurements and modeling of absorptive partitioning of volatile organic compounds to painted surfaces. *Indoor Air*, 30(4):745–756, 7 2020.
- [15] Intergovernmental Panel on Climate Change, editor. *Climate Change 2013 - The Physical Science Basis*. Cambridge University Press, Cambridge, 2014.
- [16] V. Faye McNeill. Atmospheric Aerosols: Clouds, Chemistry, and Climate. *Annual Review of Chemical and Biomolecular Engineering*, 8(1):427–444, 6 2017.
- [17] Ulrich Pöschl. Atmospheric aerosols: Composition, transformation, climate and health effects. *Angewandte Chemie - International Edition*, 44(46):7520–7540, 11 2005.
- [18] C Sabine, G Bala, L Bopp, V Brovkin, J Canadell, A Chhabra, R DeFries, J Galloway, M Heimann, C Jones, C Le Quéré, RB Myneni, S Piao, P Thornton, D Qin, G-k Plattner, M Tignor, SK Allen, J Boschung, A Nauels, Y Xia, V Bex, PM Midgley, Philippe Ciais, Christopher Sabine, and Govindasamy Bala. Contribution of Working Group I to the Fifth Assessment Report of the Intergovernmental Panel on Climate Change Coordinating Lead Authors: Lead Authors. *Josep Canadell (Australia), Abha Chhabra*, 2013.

- [19] Armando D. Estillore, Holly S. Morris, Victor W. Or, Hansol D. Lee, Michael R. Alves, Meagan A. Marciano, Olga Laskina, Zhen Qin, Alexei V. Tivanski, and Vicki H. Grassian. Linking hygroscopicity and the surface microstructure of model inorganic salts, simple and complex carbohydrates, and authentic sea spray aerosol particles. *Phys. Chem. Chem. Phys.*, 19(31):21101–21111, 8 2017.
- [20] Muhammad Bilal Altaf, Dabrina D. Dutcher, Timothy M. Raymond, and Miriam Arak Freedman. Effect of Particle Morphology on Cloud Condensation Nuclei Activity. *ACS Earth and Space Chemistry*, 2(6):634–639, 2018.
- [21] Daniel P. Veghte, Danielle Rae Bittner, and Miriam Arak Freedman. Cryo-transmission electron microscopy imaging of the morphology of submicrometer aerosol containing organic acids and ammonium sulfate. *Analytical Chemistry*, 86(5):2436–2442, 3 2014.
- [22] Hansol D. Lee, Kamal K. Ray, and Alexei V. Tivanski. Solid, Semisolid, and Liquid Phase States of Individual Submicrometer Particles Directly Probed Using Atomic Force Microscopy. *Analytical Chemistry*, 89(23):12720–12726, 2017.
- [23] P. J. DeMott, A. J. Prenni, X. Liu, S. M. Kreidenweis, M. D. Petters, C. H. Twohy, M. S. Richardson, T. Eidhammer, and D. C. Rogers. Predicting global atmospheric ice nuclei distributions and their impacts on climate. *Proceedings of the National Academy of Sciences*, 107(25):11217–11222, 2010.
- [24] Paul J. DeMott, Thomas C.J. Hill, Christina S. McCluskey, Kimberly A. Prather, Douglas B. Collins, Ryan C. Sullivan, Matthew J. Ruppel, Ryan H. Mason, Victoria E. Irish, Taehyoung Lee, Chung Yeon Hwang, Tae Siek Rhee, Jefferson R. Snider, Gavin R. McMeeking, Suresh Dhaniyala, Ernie R. Lewis, Jeremy J.B. Wentzell, Jonathan Abbatt, Christopher Lee, Camille M. Sultana, Andrew P. Ault, Jessica L. Axson, Myrelis Diaz Martinez, Ingrid Venero, Gilmarie Santos-Figueroa, M. Dale Stokes, Grant B. Deane, Olga L. Mayol-Bracero, Vicki H. Grassian, Timothy H. Bertram, Allan K. Bertram, Bruce F. Moffett, and Gary D. Franc. Sea spray aerosol as a unique source of ice nucleating particles. *Proceedings of the National Academy of Sciences of the United States of America*, 113(21):5797–5803, 5 2016.
- [25] Charles J. Weschler and Nicola Carslaw. Indoor Chemistry. *Environmental Science and Technology*, 52(5):2419–2428, 2018.
- [26] C. J. Weschler. Chemistry in indoor environments: 20 Years of research. *Indoor Air*, 21(3):205–218, 2011.
- [27] W. W. Nazaroff and A. H. Goldstein. Indoor chemistry: Research opportunities and challenges. *Indoor Air*, 25(4):357–361, 2015.
- [28] J. D. Sinclair, L. A. Psota-Kelty, C. J. Weschler, and H. C. Shields. Measurement and modeling of airborne concentrations and indoor surface accumulation rates of

- ionic substances at Neenah, Wisconsin. *Atmospheric Environment Part A, General Topics*, 24(3):627–638, 1990.
- [29] Glenn C. Morrison, Ping Zhao, and Lenin Kasthuri. The spatial distribution of pollutant transport to and from indoor surfaces. *Atmospheric Environment*, 40(20):3677–3685, 2006.
- [30] M. O. Andreae. The dark side of aerosols. *Nature*, 409(6821):671–672, 2 2001.
- [31] Konstantin Chingin, Runhan Yan, Dacai Zhong, and Huanwen Chen. Enrichment of Surface-Active Compounds in Bursting Bubble Aerosols. *ACS Omega*, 3(8):8709–8717, 2018.
- [32] L. M. Russell, L. N. Hawkins, A. A. Frossard, P. K. Quinn, and T. S. Bates. Carbohydrate-like composition of submicron atmospheric particles and their production from ocean bubble bursting. *Proceedings of the National Academy of Sciences*, 107(15):6652–6657, 4 2010.
- [33] Xiaofei Wang, Grant B. Deane, Kathryn A. Moore, Olivia S. Ryder, M. Dale Stokes, Charlotte M. Beall, Douglas B. Collins, Mitchell V. Santander, Susannah M. Burrows, Camille M. Sultana, and Kimberly A. Prather. The role of jet and film drops in controlling the mixing state of submicron sea spray aerosol particles. *Proceedings of the National Academy of Sciences of the United States of America*, 114(27):6978–6983, 7 2017.
- [34] Ernie R. Lewis and Stephen E. Schwartz. Sea salt aerosol production: Mechanisms, methods, measurements and models—A critical review. *Geophysical Monograph Series*, 152:1–408, 2004.
- [35] Hansol D. Lee, Holly S. Morris, Olga Laskina, Camille M. Sultana, Christopher Lee, Thilina Jayarathne, Joshua L. Cox, Xiaofei Wang, Elias S. Hasenecz, Paul J. Demott, Timothy H. Bertram, Christopher D. Cappa, Elizabeth A. Stone, Kimberly A. Prather, Vicki H. Grassian, and Alexei V. Tivanski. Organic Enrichment, Physical Phase State, and Surface Tension Depression of Nascent Core-Shell Sea Spray Aerosols during Two Phytoplankton Blooms. *ACS Earth and Space Chemistry*, 4(4):650–660, 4 2020.
- [36] Douglas B. Collins, Timothy H. Bertram, Camille M. Sultana, Christopher Lee, Jessica L. Axson, and Kimberly A. Prather. Phytoplankton blooms weakly influence the cloud forming ability of sea spray aerosol. *Geophysical Research Letters*, 43(18):9975–9983, 9 2016.
- [37] Hansol D. Lee, Samantha Wigley, Christopher Lee, Victor W. Or, Elias S. Hasenecz, Elizabeth A. Stone, Vicki H. Grassian, Kimberly A. Prather, and Alexei V. Tivanski. Physicochemical Mixing State of Sea Spray Aerosols: Morphologies Exhibit Size Dependence. *ACS Earth and Space Chemistry*, 4(9):1604–1611, 9 2020.

- [38] N. Riemer, A. P. Ault, M. West, R. L. Craig, and J. H. Curtis. Aerosol Mixing State: Measurements, Modeling, and Impacts. *Reviews of Geophysics*, 57(2):187–249, 6 2019.
- [39] Swarup China, Claudio Mazzoleni, Kyle Gorkowski, Allison C. Aiken, and Manvendra K. Dubey. Morphology and mixing state of individual freshly emitted wildfire carbonaceous particles. *Nature Communications*, 4:ncomms3122, 7 2013.
- [40] A. K. Bertram, S. T. Martin, S. J. Hanna, M. L. Smith, A. Bodsworth, Q. Chen, M. Kuwata, A. Liu, Y. You, and S. R. Zorn. Predicting the relative humidities of liquid-liquid phase separation, efflorescence, and deliquescence of mixed particles of ammonium sulfate, organic material, and water using the organic-to-sulfate mass ratio of the particle and the oxygen-to-carbon ele. *Atmospheric Chemistry and Physics*, 11(21):10995–11006, 2011.
- [41] Eugene F. Mikhailov, Mira L. Pöhlker, Kathrin Reinmuth-Selzle, Sergey S. Vlasenko, Ovid O. Krüger, Janine Fröhlich-Nowoisky, Christopher Pöhlker, Olga A. Ivanova, Alexey A. Kiselev, Leslie A. Kremper, and Ulrich Pöschl. Water uptake of subpollen aerosol particles: Hygroscopic growth, cloud condensation nuclei activation, and liquid-liquid phase separation. *Atmospheric Chemistry and Physics*, 21(9):6999–7022, 5 2021.
- [42] M. D. Petters and S. M. Kreidenweis. A single parameter representation of hygroscopic growth and cloud condensation nucleus activity. *Atmospheric Chemistry and Physics*, 7(8):1961–1971, 2007.
- [43] Nicholas E Rothfuss and Markus D Petters. Characterization of the temperature and humidity-dependent phase diagram of amorphous nanoscale organic aerosols. *Physical Chemistry Chemical Physics*, 19(9):6532–6545, 2017.
- [44] Hansol D. Lee and Alexei V. Tivanski. Atomic Force Microscopy: An Emerging Tool in Measuring the Phase State and Surface Tension of Individual Aerosol Particles. *Annual Review of Physical Chemistry*, 72:235–252, 2020.
- [45] Holly S. Morris, Armando D. Estillore, Olga Laskina, Vicki H. Grassian, and Alexei V. Tivanski. Quantifying the Hygroscopic Growth of Individual Submicrometer Particles with Atomic Force Microscopy. *Analytical Chemistry*, 88(7):3647–3654, 4 2016.
- [46] Olga Laskina, Holly S. Morris, Joshua R. Grandquist, Zhen Qin, Elizabeth A. Stone, Alexei V. Tivanski, and Vicki H. Grassian. Size Matters in the water uptake and hygroscopic growth of atmospherically relevant multicomponent aerosol particles. *Journal of Physical Chemistry A*, 119(19):4489–4497, 5 2015.
- [47] Steven R. Schill, Douglas B. Collins, Christopher Lee, Holly S. Morris, Gordon A. Novak, Kimberly A. Prather, Patricia K. Quinn, Camille M. Sultana, Alexei V.

- Tivanski, Kathryn Zimmermann, Christopher D. Cappa, and Timothy H. Bertram. The impact of aerosol particle mixing state on the hygroscopicity of sea spray aerosol. *ACS Central Science*, 1(3):132–141, 6 2015.
- [48] Sabin Kasparoglu, Ying Li, Manabu Shiraiwa, and Markus D. Petters. Toward closure between predicted and observed particle viscosity over a wide range of temperatures and relative humidity. *Atmospheric Chemistry and Physics*, 21(2):1127–1141, 1 2021.
- [49] Muhammad Bilal Altaf, Dabrina D. Dutcher, Timothy M. Raymond, and Miriam Arak Freedman. Effect of Particle Morphology on Cloud Condensation Nuclei Activity. *ACS Earth and Space Chemistry*, 2(6):634–639, 2018.
- [50] Elena Gómez Alvarez, Henri Wortham, Rafal Strekowski, Cornelius Zetzsch, and Sasho Gligorovski. Atmospheric photosensitized heterogeneous and multiphase reactions: From outdoors to indoors. *Environmental Science and Technology*, 46(4):1955–1963, 2012.
- [51] J E Shilling, S M King, M Mochida, D R Worsnop, and S T Martin. Mass Spectral Evidence That Small Changes in Composition Caused by Oxidative Aging Processes Alter Aerosol CCN Properties. 2007.
- [52] Bernadette Rosati, Sigurd Christiansen, Anders Dinesen, Pontus Roldin, Andreas Massling, E. Douglas Nilsson, and Merete Bilde. The impact of atmospheric oxidation on hygroscopicity and cloud droplet activation of inorganic sea spray aerosol. *Scientific Reports*, 11(1):1–13, 5 2021.
- [53] Jonathan V. Trueblood, Xiaofei Wang, Victor W. Or, Michael R. Alves, Mitchell V. Santander, Kimberly A. Prather, and Vicki H. Grassian. The Old and the New: Aging of Sea Spray Aerosol and Formation of Secondary Marine Aerosol through OH Oxidation Reactions. *ACS Earth and Space Chemistry*, 3(10):2307–2314, 10 2019.
- [54] Neil E. Klepeis, William C. Nelson, Wayne R. Ott, John P. Robinson, Andy M. Tsang, Paul Switzer, Joseph V. Behar, Stephen C. Hern, and William H. Engelmann. The National Human Activity Pattern Survey (NHAPS): A resource for assessing exposure to environmental pollutants. *Journal of Exposure Analysis and Environmental Epidemiology*, 11(3):231–252, 2001.
- [55] Andrew P. Ault, Vicki H. Grassian, Nicola Carslaw, Douglas B. Collins, Hugo Destailats, D. James Donaldson, Delphine K. Farmer, Jose L. Jimenez, V. Faye McNeill, Glenn C. Morrison, Rachel E. O’Brien, Manabu Shiraiwa, Marina E. Vance, J. R. Wells, and Wei Xiong. Indoor Surface Chemistry: Developing a Molecular Picture of Reactions on Indoor Interfaces. *Chem*, 6(12):3203–3218, 12 2020.

- [56] Qin-Tao Liu, Rachel Chen, Brian E. McCarry, Miriam L. Diamond, and Bagher Bahavar. Characterization of Polar Organic Compounds in the Organic Film on Indoor and Outdoor Glass Windows. *Environmental Science & Technology*, 37(11):2340–2349, 2003.
- [57] Chun Yan Huo, Li Yan Liu, Zi Feng Zhang, Wan Li Ma, Wei Wei Song, Hai Ling Li, Wen Long Li, Kurunthachalam Kannan, Yong Kai Wu, Ya Meng Han, Zhi Xiang Peng, and Yi Fan Li. Phthalate esters in indoor window films in a northeastern Chinese urban center: Film growth and implications for human exposure. *Environmental Science and Technology*, 50(14):7743–7751, 2016.
- [58] Charles J. Weschler and Helen C. Shields. Experiments probing the influence of air exchange rates on secondary organic aerosols derived from indoor chemistry. *Atmospheric Environment*, 37(39-40):5621–5631, 2003.
- [59] Charles J. Weschler. The influence of ventilation on reactions among indoor pollutants: Modeling and experimental observations. *Indoor Air*, 10(2):92–100, 2000.
- [60] C. Liu, Y. Zhang, J. L. Benning, and J. C. Little. The effect of ventilation on indoor exposure to semivolatile organic compounds. *Indoor Air*, 25(3):285–296, 2015.
- [61] Karin Hermansson, Ulf Lindberg, Bertil Hok, and Goran Palmkog. Wetting properties of silicon surfaces. *Transducers '91*, pages 193–196, 1991.
- [62] Shawn F. Kowal, Seth R. Allen, and Tara F. Kahan. Wavelength-Resolved Photon Fluxes of Indoor Light Sources: Implications for HOx Production. *Environmental Science and Technology*, 51(18):10423–10430, 2017.
- [63] Alvin C.K. Lai and William W. Nazaroff. Modeling indoor particle deposition from turbulent flow onto smooth surfaces. *Journal of Aerosol Science*, 31(4):463–476, 2000.
- [64] Buuan Lam, Miriam L. Diamond, André J. Simpson, Paul A. Makar, Jennifer Truong, and Nadia A. Hernandez-Martinez. Chemical composition of surface films on glass windows and implications for atmospheric chemistry. *Atmospheric Environment*, 39(35):6578–6586, 2005.
- [65] Yunliang Zhao, Min Hu, Sjaak Slanina, and Yuanhang Zhang. The molecular distribution of fine particulate organic matter emitted from Western-style fast food cooking. *Atmospheric Environment*, 41(37):8163–8171, 2007.
- [66] James M. Mattila, Pascale S.J. Lakey, Manabu Shiraiwa, Chen Wang, Jonathan P.D. Abbatt, Caleb Arata, Allen H. Goldstein, Laura Ampollini, Erin F. Katz, Peter F. Decarlo, Shan Zhou, Tara F. Kahan, Felipe J. Cardoso-Saldaña, Lea Hildebrandt Ruiz, Andrew Abeleira, Erin K. Boedicker, Marina E. Vance, and Delphine K. Farmer. Multiphase Chemistry Controls Inorganic Chlorinated and Nitrogenated

- Compounds in Indoor Air during Bleach Cleaning. *Environmental Science and Technology*, 54(3):1730–1739, 2020.
- [67] Felix Klein, Urs Baltensperger, André S.H. Prévôt, and Imad El Haddad. Quantification of the impact of cooking processes on indoor concentrations of volatile organic species and primary and secondary organic aerosols. *Indoor Air*, 29(6):926–942, 2019.
- [68] Congrong He, Lidia Morawska, and Len Taplin. Particle emission characteristics of office printers. *Environmental Science and Technology*, 41(17):6039–6045, 2007.
- [69] Sandra V. Pirela, Georgios Pyrgiotakis, Dhimiter Bello, Treye Thomas, Vincent Castanova, and Philip Demokritou. Development and characterization of an exposure platform suitable for physico-chemical, morphological and toxicological characterization of printer-emitted particles (PEPs). *Inhalation Toxicology*, 26(7):400–408, 2014.
- [70] Congrong He, Lidia Morawska, and Len Taplin. Office Particle Emission Characteristics of Office Printers. *Environ. Sci. Technol.*, 41:6039–6045, 2007.
- [71] Chenyang Bi, Yirui Liang, and Ying Xu. Fate and Transport of Phthalates in Indoor Environments and the Influence of Temperature: A Case Study in a Test House. *Environmental Science and Technology*, 49(16):9674–9681, 2015.
- [72] Ying Xu, Elaine A.Cohen Hubal, Per A. Clausen, and John C. Little. Predicting residential exposure to phthalate plasticizer emitted from vinyl flooring: A mechanistic analysis. *Environmental Science and Technology*, 43(7):2374–2380, 4 2009.
- [73] Yirui Liang and Ying Xu. Emission of phthalates and phthalate alternatives from vinyl flooring and crib mattress covers: The influence of temperature. *Environmental Science and Technology*, 48(24):14228–14237, 12 2014.
- [74] Jennifer L. Benning, Zhe Liu, Andrea Tiwari, John C. Little, and Linsey C. Marr. Characterizing gas-particle interactions of phthalate plasticizer emitted from vinyl flooring. *Environmental Science and Technology*, 47(6):2696–2703, 3 2013.
- [75] Erin K. Boedicker, Ethan W. Emerson, Gavin R. McMeeking, Sameer Patel, Marina E. Vance, and Delphine K. Farmer. Fates and spatial variations of accumulation mode particles in a multi-zone indoor environment during the HOMEChem campaign. *Environmental Science: Processes & Impacts*, 23(7):1029–1039, 7 2021.
- [76] Alexandre Dazzi and Craig B. Prater. AFM-IR: Technology and applications in nanoscale infrared spectroscopy and chemical imaging. *Chemical Reviews*, 117(7):5146–5173, 12 2017.

- [77] M. Hallquist, J. C. Wenger, U. Baltensperger, Y. Rudich, D. Simpson, M. Claeys, J. Dommen, N. M. Donahue, C. George, a. H. Goldstein, J. F. Hamilton, H. Herrmann, T. Hoffmann, Y. Iinuma, M. Jang, M. E. Jenkin, J. L. Jimenez, a. Kiendler-Scharr, W. Maenhaut, G. McFiggans, Th. F. Mentel, a. Monod, a. S. H. Prévôt, J. H. Seinfeld, J. D. Surratt, R. Szmigielski, and J. Wildt. The formation, properties and impact of secondary organic aerosol: current and emerging issues. *Atmos. Chem. Phys.*, 9(14):5155–5236, 2009.
- [78] Natalie Mahowald, Daniel S. Ward, Silvia Kloster, Mark G. Flanner, Colette L. Heald, Nicholas G. Heavens, Peter G. Hess, Jean-Francois Lamarque, and Patrick Y. Chuang. Aerosol Impacts on Climate and Biogeochemistry. *Annual Review of Environment and Resources*, 36(1):45–74, 11 2011.
- [79] T S Bates, T L Anderson, T Baynard, T Bond, O Boucher, G Carmichael, A Clarke, C Erlick, and H Guo. and Physics Aerosol direct radiative effects over the northwest Atlantic , northwest Pacific , and North Indian Oceans : estimates based on in-situ chemical and optical measurements and chemical transport modeling. *Atmos. Chem. Phys. Atmospheric Chemistry and Physics*, 6:1657–1732, 2006.
- [80] Natalie Mahowald, Daniel S. Ward, Silvia Kloster, Mark G. Flanner, Colette L. Heald, Nicholas G. Heavens, Peter G. Hess, Jean-Francois Lamarque, and Patrick Y. Chuang. Aerosol Impacts on Climate and Biogeochemistry. *Annual Review of Environment and Resources*, 36(1):45–74, 11 2011.
- [81] André Nel. Air pollution-related illness: Effects of particles. *Science*, 308(5723):804–806, 5 2005.
- [82] Meera Subramanian. Can Delhi save itself from its toxic air? *Nature*, 534(7606):166–169, 6 2016.
- [83] Manabu Shiraiwa, Kayo Ueda, Andrea Pozzer, Gerhard Lammel, Christopher J. Kampf, Akihiro Fushimi, Shinichi Enami, Andrea M. Arangio, Janine Fröhlich-Nowoisky, Yuji Fujitani, Akiko Furuyama, Pascale Sylvie Jeanne Lakey, Jos Lelieveld, Kurt Lucas, Yu Morino, Ulrich Pöschl, Satoshi Takahama, Akinori Takami, Haijie Tong, Bettina Weber, Ayako Yoshino, and Kei Sato. Aerosol health effects from molecular to global scales. *Environmental Science & Technology*, page acs.est.7b04417, 2017.
- [84] Kathrin Reinmuth-Selzle, Christopher J. Kampf, Kurt Lucas, Naama Lang-Yona, Janine Fröhlich-Nowoisky, Manabu Shiraiwa, Pascale S.J. Lakey, Senchao Lai, Fobang Liu, Anna T. Kunert, Kira Ziegler, Fangxia Shen, Rossella Sgarbanti, Bettina Weber, Iris Bellinghausen, Joachim Saloga, Michael G. Weller, Albert Duschl, Detlef Schuppan, and Ulrich Pöschl. Air Pollution and Climate Change Effects on Allergies in the Anthropocene: Abundance, Interaction, and Modification of Allergens and Adjuvants. *Environmental Science and Technology*, 51(8):4119–4141, 4 2017.

- [85] Julia Schmale, Drew Shindell, Erika Von Schneidemesser, Ilan Chabay, and Mark Lawrence. Air pollution: Clean up our skies. *Nature*, 515(7527):335–337, 11 2014.
- [86] Richard E. Cochran, Olga Laskina, Jonathan V. Trueblood, Armando D. Estilloro, Holly S. Morris, Thilina Jayarathne, Camille M. Sultana, Christopher Lee, Peng Lin, Julia Laskin, Alexander Laskin, Jacqueline A. Dowling, Zhen Qin, Christopher D. Cappa, Timothy H. Bertram, Alexei V. Tivanski, Elizabeth A. Stone, Kimberly A. Prather, and Vicki H. Grassian. Molecular Diversity of Sea Spray Aerosol Particles: Impact of Ocean Biology on Particle Composition and Hygroscopicity. *Chem*, 2(5):655–667, 5 2017.
- [87] K. A. Prather, T. H. Bertram, V. H. Grassian, G. B. Deane, M. D. Stokes, P. J. DeMott, L. I. Aluwihare, B. P. Palenik, F. Azam, J. H. Seinfeld, R. C. Moffet, M. J. Molina, C. D. Cappa, F. M. Geiger, G. C. Roberts, L. M. Russell, A. P. Ault, J. Baltrusaitis, D. B. Collins, C. E. Corrigan, L. A. Cuadra-Rodriguez, C. J. Ebben, S. D. Forestieri, T. L. Guasco, S. P. Hersey, M. J. Kim, W. F. Lambert, R. L. Modini, W. Mui, B. E. Pedler, M. J. Ruppel, O. S. Ryder, N. G. Schoepp, R. C. Sullivan, and D. Zhao. Bringing the ocean into the laboratory to probe the chemical complexity of sea spray aerosol. *Proceedings of the National Academy of Sciences*, 110(19):7550–7555, 5 2013.
- [88] Patricia K. Quinn, Douglas B. Collins, Vicki H. Grassian, Kimberly A. Prather, and Timothy S. Bates. Chemistry and Related Properties of Freshly Emitted Sea Spray Aerosol. *Chemical Reviews*, 115(10):4383–4399, 5 2015.
- [89] L. M. Russell, R. Bahadur, and P. J. Ziemann. Identifying organic aerosol sources by comparing functional group composition in chamber and atmospheric particles. *Proceedings of the National Academy of Sciences*, 108(9):3516–3521, 3 2011.
- [90] M. O. Andreae and A. Gelencsér. Black carbon or brown carbon? the nature of light-absorbing carbonaceous aerosols. *Atmospheric Chemistry and Physics*, 6(10):3131–3148, 2006.
- [91] N. O A Kwamena, J. Buajarern, and J. P. Reid. Equilibrium morphology of mixed organic/Inorganic/Aqueous Aerosol droplets: Investigating the effect of relative humidity and surfactants. *Journal of Physical Chemistry A*, 114(18):5787–5795, 5 2010.
- [92] Joshua P. Darr, Shannon Q. Davis, Yohei Kohno, Kevin McKenna, and Paul Morales. Morphological effects on the hygroscopic properties of sodium chloride-sodium sulfate aerosols. *Journal of Aerosol Science*, 77:158–167, 11 2014.
- [93] Mijung Song, Claudia Marcolli, Ulrich K. Krieger, Daniel M. Lienhard, and Thomas Peter. Morphologies of mixed organic/inorganic/aqueous aerosol droplets. *Faraday Discussions*, 165(0):289, 10 2013.

- [94] G. Binnig, C. F. Quate, and Ch Gerber. Atomic force microscope. *Physical Review Letters*, 56(9):930–933, 3 1986.
- [95] Vicki H. Grassian. Particle Chemistry in the Environment: Challenges and Opportunities. *Journal of Physical Chemistry Letters*, 6(19):3880–3881, 10 2015.
- [96] Hansol D. Lee, Armando D. Estilloro, Holly S Morris, Kamal K Ray, Aldair Alejandro, Vicki H. Grassian, and Alexei V Tivanski. Direct Surface Tension Measurements of Individual Submicrometer Particles Using Atomic Force Microscopy. *The Journal of Physical Chemistry A*, 121(43):acs.jpca.7b04041, 11 2017.
- [97] Thorsten Hoffmann, Ru Jin Huang, and Markus Kalberer. Atmospheric analytical chemistry. *Analytical Chemistry*, 83(12):4649–4664, 6 2011.
- [98] U. Dusek, G. P. Frank, L. Hildebrandt, J. Curtius, J. Schneider, S. Walter, D. Chand, F. Drewnick, S. Hings, D. Jung, S. Borrmann, and M. O. Andreae. Size matters more than chemistry for cloud-nucleating ability of aerosol particles. *Science*, 312(5778):1375–1378, 6 2006.
- [99] Ilona Riipinen, Taina Yli-Juuti, Jeffrey R. Pierce, Tuukka Petäjä, Douglas R. Worsnop, Markku Kulmala, and Neil M. Donahue. The contribution of organics to atmospheric nanoparticle growth. *Nature Geoscience*, 5(7):453–458, 6 2012.
- [100] Alexandre Dazzi, Craig B. Prater, Qichi Hu, D. Bruce Chase, John F. Rabolt, and Curtis Marcott. AFM-IR: Combining atomic force microscopy and infrared spectroscopy for nanoscale chemical characterization. *Applied Spectroscopy*, 66(12):1365–1384, 12 2012.
- [101] Andrea Centrone. Infrared Imaging and Spectroscopy Beyond the Diffraction Limit. *Annual Review of Analytical Chemistry*, 8(1):101–126, 7 2015.
- [102] Amy L. Bondy, Rachel M. Kirpes, Rachel L. Merzel, Kerri A. Pratt, Mark M. Banaszak Holl, and Andrew P. Ault. Atomic Force Microscopy-Infrared Spectroscopy of Individual Atmospheric Aerosol Particles: Subdiffraction Limit Vibrational Spectroscopy and Morphological Analysis. *Analytical Chemistry*, 89(17):8594–8598, 9 2017.
- [103] G. C. Roberts, D. A. Day, L. M. Russell, E. J. Dunlea, J. L. Jimenez, J. M. Tomlinson, D. R. Collins, Y. Shinozuka, and A. D. Clarke. Characterization of particle cloud droplet activity and composition in the free troposphere and the boundary layer during INTEX-B. *Atmospheric Chemistry and Physics*, 10(14):6627–6644, 2010.
- [104] K. J. Baustian, M. E. Wise, and M. A. Tolbert. Depositional ice nucleation on solid ammonium sulfate and glutaric acid particles. *Atmospheric Chemistry and Physics*, 10(5):2307–2317, 2010.

- [105] Holly S. Morris, Vicki H. Grassian, and Alexei V. Tivanski. Humidity-dependent surface tension measurements of individual inorganic and organic submicrometre liquid particles. *Chem. Sci.*, 6(5):3242–3247, 4 2015.
- [106] Paula K. Hudson, Elizabeth R. Gibson, Mark A. Young, Paul D. Kleiber, and Vicki H. Grassian. A newly designed and constructed instrument for coupled infrared extinction and size distribution measurements of aerosols. *Aerosol Science and Technology*, 41(7):701–710, 6 2007.
- [107] Elizabeth R. Gibson, Paula K. Hudson, and Vicki H. Grassian. Physicochemical properties of nitrate aerosols: Implications for the atmosphere. *Journal of Physical Chemistry A*, 110(42):11785–11799, 2006.
- [108] David D. Weis and George E. Ewing. Infrared spectroscopic signatures of $(\text{NH}_4)_2\text{SO}_4$ aerosols. *Journal of Geophysical Research Atmospheres*, 101(13):18709–18720, 8 1996.
- [109] A. Dazzi, F. Glotin, and R. Carminati. Theory of infrared nanospectroscopy by photothermal induced resonance. *Journal of Applied Physics*, 107(12), 2010.
- [110] Basudev Lahiri, Glenn Holland, and Andrea Centrone. Chemical imaging beyond the diffraction limit: Experimental validation of the PTIR technique. *Small*, 9(3):439–445, 2 2013.
- [111] M. E. Earle, R. G. Pancescu, B. Cosic, A. Y. Zasetky, and J. J. Sloan. Temperature-dependent complex indices of refraction for crystalline $(\text{NH}_4)_2\text{SO}_4$. *Journal of Physical Chemistry A*, 110(48):13022–13028, 2006.
- [112] Medhat Ibrahim, Moussa Alaam, Hanan El-Haes, Abraham F. Jalbout, and Aneel De Leon. Analysis of the structure and vibrational spectra of glucose and fructose. *Ecletica Quimica*, 31(3):15–21, 2006.
- [113] Feng Lu, Mingzhou Jin, and Mikhail A. Belkin. Tip-enhanced infrared nanospectroscopy via molecular expansion force detection. *Nature Photonics*, 8(4):307–312, 2014.
- [114] Ignatius N. Tang and Harry R. Munkelwitz. Composition and temperature dependence of the deliquescence properties of hygroscopic aerosols. *Atmospheric Environment Part A, General Topics*, 27(4):467–473, 3 1993.
- [115] I. W. Boyd and J. I. B. Wilson. A study of thin silicon dioxide films using infrared absorption techniques. *Journal of Applied Physics*, 53(6):4166–4172, 6 1982.
- [116] Roger Newman. Polarized infrared spectrum of sodium nitrite. *The Journal of Chemical Physics*, 20(3):444–446, 3 1952.

- [117] Jean Noël Druon, Pierre Hélaouët, Grégory Beaugrand, Jean Marc Fromentin, Andreas Palialexis, and Nicolas Hoepffner. Satellite-based indicator of zooplankton distribution for global monitoring. *Scientific Reports*, 9(1):1–13, 3 2019.
- [118] Sergio R. Signorini, Bryan A. Franz, and Charles R. McClain. Chlorophyll variability in the oligotrophic gyres: Mechanisms, seasonality and trends. *Frontiers in Marine Science*, 2(FEB):1, 2015.
- [119] J. T. Hardy. The sea surface microlayer: Biology, chemistry and anthropogenic enrichment. *Progress in Oceanography*, 11(4):307–328, 1 1982.
- [120] Terje Berntsen, Ivar S.A. Isaksen, Wei Chyung Wang, and Xin Zhong Liang. Impacts of increased anthropogenic emissions in Asia on tropospheric ozone and climate: A global 3-D model study. *Tellus, Series B: Chemical and Physical Meteorology*, 48(1):13–32, 1996.
- [121] Shannon Mala Bard. Global transport of anthropogenic contaminants and the consequences for the Arctic marine ecosystem. *Marine Pollution Bulletin*, 38(5):356–379, 5 1999.
- [122] Yanxu Zhang, Daniel J. Jacob, Hannah M. Horowitz, Long Chen, Helen M. Amos, David P. Krabbenhoft, Franz Slemr, Vincent L. St. Louis, and Elsie M. Sunderland. Observed decrease in atmospheric mercury explained by global decline in anthropogenic emissions. *Proceedings of the National Academy of Sciences of the United States of America*, 113(3):526–531, 1 2016.
- [123] Kathryn J. Mayer, Xiaofei Wang, Mitchell V. Santander, Brock A. Mitts, Jonathan S. Sauer, Camille M. Sultana, Christopher D. Cappa, and Kimberly A. Prather. Secondary Marine Aerosol Plays a Dominant Role over Primary Sea Spray Aerosol in Cloud Formation. *ACS Central Science*, 6(12):2259–2266, 12 2020.
- [124] Natalie Mahowald. Aerosol indirect effect on biogeochemical cycles and climate. *Science*, 334(6057):794–796, 11 2011.
- [125] A. K. Bertram, S. T. Martin, S. J. Hanna, M. L. Smith, A. Bodsworth, Q. Chen, M. Kuwata, A. Liu, Y. You, and S. R. Zorn. Predicting the relative humidities of liquid-liquid phase separation, efflorescence, and deliquescence of mixed particles of ammonium sulfate, organic material, and water using the organic-to-sulfate mass ratio of the particle and the oxygen-to-carbon ele. *Atmospheric Chemistry and Physics*, 11(21):10995–11006, 2011.
- [126] Man Nin Chan, Alex K.Y. Lee, and Chak K. Chan. Responses of ammonium sulfate particles coated with glutaric acid to cyclic changes in relative humidity: Hygroscopicity and Raman characterization. *Environmental Science and Technology*, 40(22):6983–6989, 2006.

- [127] Ignatius N. Tang and Harry R. Munkelwitz. Composition and temperature dependence of the deliquescence properties of hygroscopic aerosols. *Atmospheric Environment Part A, General Topics*, 27(4):467–473, 3 1993.
- [128] M. D. Petters and S. M. Kreidenweis. A single parameter representation of hygroscopic growth and cloud condensation nucleus activity - Part 2: Including solubility. *Atmospheric Chemistry and Physics*, 8(20):6273–6279, 2008.
- [129] Jon S. Sauer, Kathryn J. Mayer, Christopher Lee, Michael R. Alves, Sarah Amiri, Cristina Bahaveolos, Emily B. Barnes, Daniel R. Crocker, Julie Dinasquet, Lauren A. Garofalo, Chathuri P. Kaluarachchi, Duyen Dang, Delaney Kilgour, Liora Mael, Brock A. Mitts, Daniel R. Moon, Clare K. Morris, Alexia N. Moore, Chi-Min Ni, Matthew A. Pendergraft, Daniel Petras, Rebecca Simpson, Stephanie Smith, Paul R. Tumminello, Joseph L. Walker, Paul J. DeMott, Delphine K. Farmer, Allen H. Goldstein, Vicki H. Grassian, Jules S. Jaffe, Francesca Malfatti, Todd R. Martz, Jonathan Slade, Alexei V. Tivanski, Timothy H. Bertram, Christopher D. Cappa, and Kimberly A. Prather. The Sea Spray Chemistry and Particle Evolution Study (SeaSCAPE): Overview and Experimental Methods. 6 2021.
- [130] Hansol D. Lee, Samantha Wigley, Christopher Lee, Victor W. Or, Elias S. Hasenecz, Elizabeth A. Stone, Vicki H. Grassian, Kimberly A. Prather, and Alexei V. Tivanski. Physicochemical Mixing State of Sea Spray Aerosols: Morphologies Exhibit Size Dependence. *ACS Earth and Space Chemistry*, 4(9):1604–1611, 2020.
- [131] Kazuo Nakamoto. Infrared and Raman Spectra of Inorganic and Coordination Compounds: Part A: Theory and Applications in Inorganic Chemistry: Sixth Edition. *Infrared and Raman Spectra of Inorganic and Coordination Compounds: Part A: Theory and Applications in Inorganic Chemistry: Sixth Edition*, pages 1–419, 4 2008.
- [132] Christopher D. Zangmeister and Jeanne E. Pemberton. Raman spectroscopy of the reaction of sodium chloride with nitric acid Sodium nitrate growth and effect of water exposure. *Journal of Physical Chemistry A*, 105(15):3788–3795, 4 2001.
- [133] Sanjai J. Parikh and Jon Chorover. Infrared spectroscopy studies of cation effects on lipopolysaccharides in aqueous solution. *Colloids and Surfaces B: Biointerfaces*, 55(2):241–250, 4 2007.
- [134] Tuncer Çaykara, Serkan Demirci, Mehmet S. Eroğlu, and Olgun Güven. Poly(ethylene oxide) and its blends with sodium alginate. *Polymer*, 46(24):10750–10757, 11 2005.
- [135] Ewelina Wiercigroch, Ewelina Szafraniec, Krzysztof Czamara, Marta Z. Pacia, Katarzyna Majzner, Kamila Kochan, Agnieszka Kaczor, Malgorzata Baranska, and Kamilla Malek. Raman and infrared spectroscopy of carbohydrates: A review. *Spectrochimica Acta - Part A: Molecular and Biomolecular Spectroscopy*, 185:317–335, 10 2017.

- [136] Sergios K. Papageorgiou, Evangelos P. Kouvelos, Evangelos P. Favvas, Andreas A. Sapalidis, George E. Romanos, and Fotios K. Katsaros. Metal-carboxylate interactions in metal-alginate complexes studied with FTIR spectroscopy. *Carbohydrate Research*, 345(4):469–473, 2 2010.
- [137] Elias S. Hasenecz, Thilina Jayarathne, Matthew A. Pendergraft, Mitchell V. Santander, Kathryn J. Mayer, Jon Sauer, Christopher Lee, Wyeth S. Gibson, Samantha M. Kruse, Francesca Malfatti, Kimberly A. Prather, and Elizabeth A. Stone. Marine Bacteria Affect Saccharide Enrichment in Sea Spray Aerosol during a Phytoplankton Bloom. *ACS Earth and Space Chemistry*, 4(9):1638–1649, 9 2020.
- [138] Thilina Jayarathne, Camille M. Sultana, Christopher Lee, Francesca Malfatti, Joshua L. Cox, Matthew A. Pendergraft, Kathryn A. Moore, Farooq Azam, Alexei V. Tivanski, Christopher D. Cappa, Timothy H. Bertram, Vicki H. Grassian, Kimberly A. Prather, and Elizabeth A. Stone. Enrichment of Saccharides and Divalent Cations in Sea Spray Aerosol during Two Phytoplankton Blooms. *Environmental Science and Technology*, 50(21):11511–11520, 2016.
- [139] Elias S. Hasenecz, Chathuri P. Kaluarachchi, Hansol D. Lee, Alexei V. Tivanski, and Elizabeth A. Stone. Saccharide Transfer to Sea Spray Aerosol Enhanced by Surface Activity, Calcium, and Protein Interactions. *ACS Earth and Space Chemistry*, 3(11):2539–2548, 11 2019.
- [140] Masato Yamamoto, Yoko Sakurai, Yoshinobu Hosoi, Hisao Ishii, Kotaro Kajikawa, Yukio Ouchi, and Kazuhiko Seki. Structures of a long-chain n-alkane, n-C₄₄H₉₀, on a Au(111) surface: An infrared reflection absorption spectroscopic study. *Journal of Physical Chemistry B*, 104(31):7363–7369, 8 2000.
- [141] M. Abb, T. Heinrich, E. Sorkau, and W. Lorenz. Phthalates in house dust. *Environment International*, 35(6):965–970, 2009.
- [142] Ming-Taun Leu, Raimo S Timonen, Leon F Keyser, and Yuk L Yung. Heterogeneous Reactions of HN₃(g) + NaCl(s) → HCl(g) + NaN₃(s) and N₂O₃(g) + NaCl(s) → Cl₂NO₂(g) + NaN₃(s). *J. Phys. Chem.*, 99:13203–13212, 1995.
- [143] Tara J. Fortin, John E. Shilling, and Margaret a. Tolbert. Infrared spectroscopic study of the low-temperature phase behavior of ammonium sulfate. *Journal of Geophysical Research*, 107(D10):4088, 2002.
- [144] Colin D. O’Dowd, Maria Cristina Facchini, Fabrizia Cavalli, Darius Ceburnis, Mihaela Mircea, Stefano Decesari, Sandro Fuzzi, Young Jun Yoon, and Jean-Philippe Putaud. Biogenically driven organic contribution to marine aerosol. *Nature* 2004 431:7009, 431(7009):676–680, 10 2004.
- [145] Bernadette Rosati, Sigurd Christiansen, Robin Wollesen de Jonge, Pontus Roldin, Mads Mørk Jensen, Kai Wang, Shamjad P. Moosakutty, Ditte Thomsen, Camilla

- Salomonsen, Noora Hyttinen, Jonas Elm, Anders Feilberg, Marianne Glasius, and Merete Bilde. New Particle Formation and Growth from Dimethyl Sulfide Oxidation by Hydroxyl Radicals. *ACS Earth and Space Chemistry*, 5(4):801–811, 4 2021.
- [146] Liisa Pirjola, Colin D. O’Dowd, Ian M. Brooks, and Markku Kulmala. Can new particle formation occur in the clean marine boundary layer? *Journal of Geophysical Research: Atmospheres*, 105(D21):26531–26546, 11 2000.
- [147] Charles J. Weschler. The influence of ventilation on reactions among indoor pollutants: Modeling and experimental observations. *Indoor Air*, 10(2):92–100, 2000.
- [148] Junfeng Zhang and Paul J. Lioy. Ozone in Residential Air: Concentrations, I/O Ratios, Indoor Chemistry, and Exposures. *Indoor Air*, 4(2):95–105, 1994.
- [149] Charles J. Weschler, Alfred T. Hodgson, and John D. Wooley. Indoor Chemistry: Ozone, Volatile Organic Compounds, and Carpets. *Environmental Science and Technology*, 26(12):2371–2377, 1992.
- [150] S. C. Lee, Sanches Lam, and Ho Kin Fai. Characterization of VOCs, ozone, and PM10 emissions from office equipment in an environmental chamber. *Building and Environment*, 36(7):837–842, 2001.
- [151] Heidi Ormstad. Suspended particulate matter in indoor air: Adjuvants and allergen carriers. *Toxicology*, 152(1-3):53–68, 2000.
- [152] H Fromme, D Twardella, S Dietrich, D Heitmann, R Schierl, B Liebl, and H Ruden. Particulate matter in the indoor air of classrooms - exploratory results from Munich and surrounding area. *Atmospheric Environment*, 41(4):854–866, 2007.
- [153] Rajasekhar Balasubramanian and Sheng Lee Sheng. Characteristics of indoor aerosols in residential homes in urban locations: A case study in Singapore. *Journal of the Air and Waste Management Association*, 57(8):981–990, 2007.
- [154] W. W. Nazaroff and A. H. Goldstein. Indoor chemistry: Research opportunities and challenges. *Indoor Air*, 25(4):357–361, 2015.
- [155] Y. Zhang, J. Xiong, J. Mo, M. Gong, and J. Cao. Understanding and controlling airborne organic compounds in the indoor environment: Mass transfer analysis and applications. *Indoor Air*, 26(1):39–60, 2016.
- [156] Glenn Morrison. Interfacial chemistry in indoor environments. *Environmental Science and Technology*, 42(10):3495–3499, 2008.
- [157] E. Uhde and T. Salthammer. Impact of reaction products from building materials and furnishings on indoor air quality-A review of recent advances in indoor chemistry. *Atmospheric Environment*, 41(15):3111–3128, 2007.

- [158] Karimatu L. Abdullahi, Juana Maria Delgado-Saborit, and Roy M. Harrison. Emissions and indoor concentrations of particulate matter and its specific chemical components from cooking: A review, 2013.
- [159] Hugo Destailats, Melissa M. Lunden, Brett C. Singer, Beverly K. Coleman, Alfred T. Hodgson, Charles J. Weschler, and William W. Nazaroff. Indoor secondary pollutants from household product emissions in the presence of ozone: A bench-scale chamber study. *Environmental Science and Technology*, 40(14):4421–4428, 2006.
- [160] Eileen Abt, Helen H. Suh, Paul Catalano, and Petros Koutrakis. Relative contribution of outdoor and indoor particle sources to indoor concentrations. *Environmental Science and Technology*, 34(17):3579–3587, 2000.
- [161] Gordana Vuković, Mira Aničić Urošević, Ivana Razumenić, Maja Kuzmanoski, Miodrag Pergal, Sandra Škrivanj, and Aleksandar Popović. Air quality in urban parking garages (PM10, major and trace elements, PAHs): Instrumental measurements vs. active moss biomonitoring. *Atmospheric Environment*, 85:31–40, 2013.
- [162] Stuart Batterman, Chunrong Jia, and Gina Hatzivasilis. Migration of volatile organic compounds from attached garages to residences: A major exposure source. *Environmental Research*, 104(2):224–240, 2007.
- [163] Robin E. Dodson, Jonathan I. Levy, John D. Spengler, James P. Shine, and Deborah H. Bennett. Influence of basements, garages, and common hallways on indoor residential volatile organic compound concentrations. *Atmospheric Environment*, 42(7):1569–1581, 2008.
- [164] Rajiv Kohli and Kashmiri L. Mittal. *Developments in Surface Contamination and Cleaning*, volume 6. 2013.
- [165] Craig M. Butt, Miriam L. Diamond, Jennifer Truong, Michael G. Ikonomou, and Arnout F.H. Ter Schure. Spatial Distribution of Polybrominated Diphenyl Ethers in Southern Ontario As Measured in Indoor and Outdoor Window Organic Films. *Environmental Science and Technology*, 38(3):724–731, 2004.
- [166] Miriam L. Diamond, Sarah E. Gingrich, Kirsten Fertuck, Brian E. McCarry, Gary A. Stern, Brian Billeck, Bert Grift, Deborah Brooker, and Thomas D. Yager. Evidence for organic film on an impervious urban surface: Characterization and potential teratogenic effects. *Environmental Science and Technology*, 34(14):2900–2908, 2000.
- [167] C. J. Cros, G. C. Morrison, J. A. Siegel, and R. L. Corsi. Long-term performance of passive materials for removal of ozone from indoor air. *Indoor Air*, 22(1):43–53, 2012.
- [168] Charles J. Weschler and Helen C. Shields. Production of the hydroxyl radical in indoor air. *Environmental Science and Technology*, 30(11):3250–3258, 1996.

- [169] Shouming Zhou, Matthew W. Forbes, Yasmine Katrib, and Jonathan P.D. Abbatt. Rapid Oxidation of Skin Oil by Ozone. *Environmental Science and Technology Letters*, 3(4):170–174, 2016.
- [170] S. M. Duncan, K. G. Sexton, and B. J. Turpin. Oxygenated VOCs, aqueous chemistry, and potential impacts on residential indoor air composition. *Indoor Air*, 28(1):198–212, 2018.
- [171] Miguel Cristobal, David San-Martin, Carlos Capdevila, José Antonio Jiménez, and Srdjan Milenkovic. Rapid fabrication and characterization of AISI 304 stainless steels modified with Cu additions by additive alloy melting (ADAM). *Journal of Materials Research and Technology*, 2018.
- [172] E. S. Gadelmawla, M. M. Koura, T. M.A. Maksoud, I. M. Elewa, and H. H. Soliman. Roughness parameters. *Journal of Materials Processing Technology*, 123(1):133–145, 2002.
- [173] Dongjuan Dai, Aaron J. Prussin, Linsey C. Marr, Peter J. Vikesland, Marc A. Edwards, and Amy Pruden. Factors Shaping the Human Exposome in the Built Environment: Opportunities for Engineering Control, 2017.
- [174] Sasho Gligorovski and Jonathan P D Abbatt. An indoor chemical cocktail. *Science (New York, N.Y.)*, 359(6376):632–633, 2018.
- [175] Charles J. Weschler and William W. Nazaroff. Dermal uptake of organic vapors commonly found in indoor air. *Environmental Science and Technology*, 48(2):1230–1237, 2014.
- [176] J. P.S. Wong, N. Carslaw, R. Zhao, S. Zhou, and J. P.D. Abbatt. Observations and impacts of bleach washing on indoor chlorine chemistry. *Indoor Air*, 27(6):1082–1090, 2017.
- [177] G. Bekö, G. Morrison, C. J. Weschler, H. M. Koch, C. Pälmeke, T. Salthammer, T. Schripp, A. Eftekhari, J. Toftum, and G. Clausen. Dermal uptake of nicotine from air and clothing: Experimental verification. *Indoor Air*, 28(2):247–257, 2018.
- [178] Victor W. Or, Michael R. Alves, Michael Wade, Sarah Schwab, Richard L. Corsi, and Vicki H. Grassian. Crystal Clear? Microspectroscopic Imaging and Physicochemical Characterization of Indoor Depositions on Window Glass. *Environmental Science and Technology Letters*, 5(8):514–519, 2018.
- [179] R. Alwarda, S. Zhou, and J. P.D. Abbatt. Heterogeneous oxidation of indoor surfaces by gas-phase hydroxyl radicals. *Indoor Air*, 28(5):655–664, 2018.
- [180] Douglas B. Collins, Rachel F. Hems, Shouming Zhou, Chen Wang, Eloi Grignon, Masih Alavy, Jeffrey A. Siegel, and Jonathan P.D. Abbatt. Evidence for Gas-Surface

- Equilibrium Control of Indoor Nitrous Acid. *Environmental Science and Technology*, 52(21):12419–12427, 2018.
- [181] Maxence Mendez, Nadège Blond, Patrice Blondeau, Coralie Schoemaeker, and Didier A. Hauglustaine. Assessment of the impact of oxidation processes on indoor air pollution using the new time-resolved INCA-Indoor model. *Atmospheric Environment*, 122:521–530, 2015.
- [182] Tengyu Liu, Zhaoyi Wang, Dan Dan Huang, Xinming Wang, and Chak K. Chan. Significant Production of Secondary Organic Aerosol from Emissions of Heated Cooking Oils. *Environmental Science and Technology Letters*, 5(1):32–37, 2018.
- [183] Xianming Zhang, Miriam L. Diamond, Matthew Robson, and Stuart Harrad. Sources, emissions, and fate of polybrominated diphenyl ethers and polychlorinated biphenyls indoors in Toronto, Canada. *Environmental Science and Technology*, 45(8):3268–3274, 2011.
- [184] Yuan Fang, Saleh Riahi, Andrew T. McDonald, Mona Shrestha, Douglas J. Tobias, and Vicki H. Grassian. What Is the Driving Force behind the Adsorption of Hydrophobic Molecules on Hydrophilic Surfaces? *Journal of Physical Chemistry Letters*, 10(3):468–473, 2019.
- [185] Yuan Fang, Dominika Lesnicki, Kristin J. Wall, Marie Pierre Gageot, Marialore Sulpizi, Veronica Vaida, and Vicki H. Grassian. Heterogeneous Interactions between Gas-Phase Pyruvic Acid and Hydroxylated Silica Surfaces: A Combined Experimental and Theoretical Study. *Journal of Physical Chemistry A*, 123(5):983–991, 2019.
- [186] Yuan Fang, Pascale S.J. Lakey, Saleh Riahi, Andrew T. McDonald, Mona Shrestha, Douglas J. Tobias, Manabu Shiraiwa, and Vicki H. Grassian. A molecular picture of surface interactions of organic compounds on prevalent indoor surfaces: Limonene adsorption on SiO₂. *Chemical Science*, 10(10):2906–2914, 2019.
- [187] Hui Ming Hung and Chen Wei Tang. Effects of temperature and physical state on heterogeneous oxidation of oleic acid droplets with ozone. *Journal of Physical Chemistry A*, 114(50):13104–13112, 2010.
- [188] Heather Schwartz-Narbonne and D. James Donaldson. Water uptake by indoor surface films. *Scientific reports*, 9(1):11089, 7 2019.
- [189] Zilin Zhou, Shouming Zhou, and Jonathan P.D. Abbatt. Kinetics and Condensed-Phase Products in Multiphase Ozonolysis of an Unsaturated Triglyceride. *Environmental Science and Technology*, 53(21):12467–12475, 2019.
- [190] D. K. Farmer, M. E. Vance, J. P.D. Abbatt, A. Abeleira, M. R. Alves, C. Arata, E. Boedicker, S. Bourne, F. Cardoso-Saldaña, R. Corsi, P. F. Decarlo, A. H. Goldstein, V. H. Grassian, L. Hildebrandt Ruiz, J. L. Jimenez, T. F. Kahan, E. F. Katz,

- J. M. Mattila, W. W. Nazaroff, A. Novoselac, R. E. O'Brien, V. W. Or, S. Patel, S. Sankhyan, P. S. Stevens, Y. Tian, M. Wade, C. Wang, S. Zhou, and Y. Zhou. Overview of HOMEChem: House Observations of Microbial and Environmental Chemistry. *Environmental Science: Processes and Impacts*, 21(8):1280–1300, 2019.
- [191] Sameer Patel, Sumit Sankhyan, Erin K. Boedicker, Peter F. Decarlo, Delphine K. Farmer, Allen H. Goldstein, Erin F. Katz, William W. Nazaroff, Yilin Tian, Joonas Vanhanen, and Marina E. Vance. Indoor Particulate Matter during HOMEChem: Concentrations, Size Distributions, and Exposures. *Environmental Science and Technology*, 54(12):7107–7116, 5 2020.
- [192] Olga Laskina, Holly S. Morris, Joshua R. Grandquist, Armando D. Estillore, Elizabeth A. Stone, Vicki H. Grassian, and Alexei V. Tivanski. Substrate-Deposited Sea Spray Aerosol Particles: Influence of Analytical Method, Substrate, and Storage Conditions on Particle Size, Phase, and Morphology. *Environmental Science and Technology*, 49(22):13447–13453, 11 2015.
- [193] Eva R. Garland, Elias P. Rosen, Laura I. Clarke, and Tomas Baer. Structure of submonolayer oleic acid coverages on inorganic aerosol particles: Evidence of island formation. *Physical Chemistry Chemical Physics*, 10(21):3156–3161, 2008.
- [194] W. C. Hinds. *Properties, Behavior, and Measurement of Airborne Particles*, volume 14. Wiley-Interscience, 2 edition, 1999.
- [195] Milton. Kerker. *Aerosols and Atmospheric chemistry : the kendall award symposium honoring*. Elsevier Science, 1 edition, 1972.
- [196] Tareq Hussein, Aleš Hruška, Pavla Dohányosová, Lucie Džumbová, Jiří Hemerka, Markku Kulmala, and Jiří Smolík. Deposition rates on smooth surfaces and coagulation of aerosol particles inside a test chamber. *Atmospheric Environment*, 43(4):905–914, 2009.
- [197] Kasper Kristensen, David M. Lunderberg, Yingjun Liu, Pawel K. Misztal, Yilin Tian, Caleb Arata, William W. Nazaroff, and Allen H. Goldstein. Sources and dynamics of semivolatile organic compounds in a single-family residence in northern California. *Indoor Air*, 29(4):645–655, 2019.
- [198] J. D. Sinclair, L. A. Psota-Kelty, and C. J. Weschler. Indoor/outdoor ratios and indoor surface accumulations of ionic substances at Newark, New Jersey. *Atmospheric Environment (1967)*, 22(3):461–469, 1988.
- [199] William W. Nazaroff, Mary P. Ligocki, Timothy Ma, and Glen R. Cass. Particle deposition in museums: Comparison of modeling and measurement results. *Aerosol Science and Technology*, 13(3):332–348, 1990.

- [200] Bin Zhao, Chun Chen, and Zhongchao Tan. Modeling of ultrafine particle dispersion in indoor environments with an improved drift flux model. *Journal of Aerosol Science*, 40(1):29–43, 2009.
- [201] N. P. Gao and J. L. Niu. Modeling particle dispersion and deposition in indoor environments. *Atmospheric Environment*, 41(18):3862–3876, 2007.
- [202] Donghyun Rim, Jung Il Choi, and Lance A. Wallace. Size-Resolved Source Emission Rates of Indoor Ultrafine Particles Considering Coagulation. *Environmental Science and Technology*, 50(18):10031–10038, 2016.
- [203] Tengyu Liu, Zijun Li, Mannin Chan, and Chak K. Chan. Formation of secondary organic aerosols from gas-phase emissions of heated cooking oils. *Atmospheric Chemistry and Physics*, 17(12):7333–7344, 2017.
- [204] Jonathan P. Reid, Allan K. Bertram, David O. Topping, Alexander Laskin, Scot T. Martin, Markus D. Petters, Francis D. Pope, and Grazia Rovelli. The viscosity of atmospherically relevant organic particles. *Nature Communications*, 9(956):1–14, 12 2018.
- [205] Kamal K. Ray, Hansol D. Lee, Miguel A. Gutierrez, Franklin J. Chang, and Alexei V. Tivanski. Correlating 3D Morphology, Phase State, and Viscoelastic Properties of Individual Substrate-Deposited Particles. *Analytical Chemistry*, 91(12):7621–7630, 2019.
- [206] Mikinori Kuwata and Scot T. Martin. Phase of atmospheric secondary organic material affects its reactivity. *Proceedings of the National Academy of Sciences of the United States of America*, 109(43):17354–17359, 2012.
- [207] Ying Li and Manabu Shiraiwa. Timescales of secondary organic aerosols to reach equilibrium at various temperatures and relative humidities. *Atmospheric Chemistry and Physics*, 19(9):5959–5971, 2019.
- [208] Young Chul Song, Allen E. Haddrell, Bryan R. Bzdek, Jonathan P. Reid, Thomas Bannan, David O. Topping, Carl Percival, and Chen Cai. Measurements and Predictions of Binary Component Aerosol Particle Viscosity. *Journal of Physical Chemistry A*, 120(41):8123–8137, 2016.
- [209] Jonathan H. Slade, Andrew P. Ault, Alexander T. Bui, Jenna C. Ditto, Ziyang Lei, Amy L. Bondy, Nicole E. Olson, Ryan D. Cook, Sarah J. Desrochers, Rebecca M. Harvey, Matthew H. Erickson, Henry W. Wallace, Sergio L. Alvarez, James H. Flynn, Brandon E. Boor, Giuseppe A. Petrucci, Drew R. Gentner, Robert J. Griffin, and Paul B. Shepson. Bouncer Particles at Night: Biogenic Secondary Organic Aerosol Chemistry and Sulfate Drive Diel Variations in the Aerosol Phase in a Mixed Forest. *Environmental Science and Technology*, 53(9):4977–4987, 2019.

- [210] Hansol D. Lee, Armando D. Estilloro, Holly S Morris, Kamal K Ray, Aldair Alejandro, Vicki H. Grassian, and Alexei V Tivanski. Direct Surface Tension Measurements of Individual Submicrometer Particles Using Atomic Force Microscopy. *The Journal of Physical Chemistry A*, 121(43):acs.jpca.7b04041, 11 2017.
- [211] Joseph D. Berry, Michael J. Neeson, Raymond R. Dagastine, Derek Y.C. Chan, and Rico F. Tabor. Measurement of surface and interfacial tension using pendant drop tensiometry, 2015.
- [212] Allison Schwier, Dhruv Mitroo, and V. Faye McNeill. Surface tension depression by low-solubility organic material in aqueous aerosol mimics. *Atmospheric Environment*, 54:490–495, 2012.
- [213] Victor W. Or, Armando D. Estilloro, Alexei V. Tivanski, and Vicki H. Grassian. Lab on a tip: Atomic force microscopy-photothermal infrared spectroscopy of atmospherically relevant organic/inorganic aerosol particles in the nanometer to micrometer size range. *Analyst*, 143(12):2765–2774, 6 2018.
- [214] Laetitia Dalstein, Elizaveta Potapova, and Eric Tyrode. The elusive silica/water interface: Isolated silanols under water as revealed by vibrational sum frequency spectroscopy. *Physical Chemistry Chemical Physics*, 19(16):10343–10349, 2017.
- [215] Marialore Sulpizi, Marie Pierre Gageot, and Michiel Sprik. The silica-water interface: How the silanols determine the surface acidity and modulate the water properties. *Journal of Chemical Theory and Computation*, 8(3):1037–1047, 2012.
- [216] D. H. Lee and R. A. Condrate. FTIR spectral characterization of thin film coatings of oleic acid on glasses: I. Coatings on glasses from ethyl alcohol. *Journal of Materials Science*, 34(1):139–146, 1999.
- [217] Suman Ghorai, Bingbing Wang, Alexei Tivanski, and Alexander Laskin. Hygroscopic properties of internally mixed particles composed of NaCl and water-soluble organic acids. *Environmental Science and Technology*, 48(4):2234–2241, 2014.
- [218] Christos Kaltsonoudis, Evangelia Kostenidou, Evangelos Louvaris, Magda Psichoudaki, Epameinondas Tsiligiannis, Kalliopi Florou, Aikaterini Liangou, and Spyros N. Pandis. Characterization of fresh and aged organic aerosol emissions from meat charbroiling. *Atmospheric Chemistry and Physics*, 17(11):7143–7155, 2017.
- [219] L. Y. He, Y. Lin, X. F. Huang, S. Guo, L. Xue, Q. Su, M. Hu, S. J. Luan, and Y. H. Zhang. Characterization of high-resolution aerosol mass spectra of primary organic aerosol emissions from Chinese cooking and biomass burning. *Atmospheric Chemistry and Physics*, 10(23):11535–11543, 2010.
- [220] Marie Deborde and Urs von Gunten. Reactions of chlorine with inorganic and organic compounds during water treatment-Kinetics and mechanisms: A critical review, 2008.

- [221] Somayeh Youssefi and Michael S. Waring. Predicting the evolution of secondary organic aerosol (SOA) size distributions due to limonene ozonolysis in indoor environments. *Building and Environment*, 108:252–262, 2016.
- [222] Beverly K. Coleman, Melissa M. Lunden, Hugo Destailats, and William W. Nazaroff. Secondary organic aerosol from ozone-initiated reactions with terpene-rich household products. *Atmospheric Environment*, 42(35):8234–8245, 2008.
- [223] Anita Lee, Allen H. Goldstein, Melita D. Keywood, Song Gao, Varuntida Varutbangkul, Roya Bahreini, Nga L. Ng, Richard C. Flagan, and John H. Seinfeld. Gas-phase products and secondary aerosol yields from the ozonolysis of ten different terpenes. *Journal of Geophysical Research Atmospheres*, 111(7), 2006.
- [224] Carolin Rösch, Dirk K. Wissenbach, Ulrich Franck, Manfred Wendisch, and Uwe Schlink. Degradation of indoor limonene by outdoor ozone: A cascade of secondary organic aerosols. *Environmental Pollution*, 226:463–472, 2017.
- [225] Clifford S. Mitchell, Junfeng Zhang, Torben Sigsgaard, Matti Jantunen, Paul J. Lioy, Robert Samson, and Meryl H. Karol. Current state of the science: Health effects and indoor environmental quality. *Environmental Health Perspectives*, 115(6):958–964, 6 2007.
- [226] C. J. Weschler. Roles of the human occupant in indoor chemistry. *Indoor Air*, 26(1):6–24, 2016.
- [227] Tengyu Liu, Qianyun Liu, Zijun Li, Lei Huo, Man Nin Chan, Xue Li, Zhen Zhou, and Chak K. Chan. Emission of volatile organic compounds and production of secondary organic aerosol from stir-frying spices. *Science of the Total Environment*, 599-600:1614–1621, 12 2017.
- [228] Mehzabeen Mannan and Sami G. Al-Ghamdi. Indoor air quality in buildings: A comprehensive review on the factors influencing air pollution in residential and commercial structure. *International Journal of Environmental Research and Public Health*, 18(6):1–24, 2021.
- [229] Zhe Liu, Wei Ye, and John C. Little. Predicting emissions of volatile and semivolatile organic compounds from building materials: A review. *Building and Environment*, 64:7–25, 2013.
- [230] Chen Wang, Douglas B. Collins, Rachel F. Hems, Nadine Borduas, María Antiñolo, and Jonathan P.D. Abbatt. Exploring Conditions for Ultrafine Particle Formation from Oxidation of Cigarette Smoke in Indoor Environments. *Environmental Science and Technology*, 52(8):4623–4631, 2018.
- [231] A. C. Rai, B. Guo, C. H. Lin, J. Zhang, J. Pei, and Q. Chen. Ozone reaction with clothing and its initiated VOC emissions in an environmental chamber. *Indoor Air*, 24(1):49–58, 2014.

- [232] X. Q. Pei, M. Song, M. Guo, F. F. Mo, and X. Y. Shen. Concentration and risk assessment of phthalates present in indoor air from newly decorated apartments. *Atmospheric Environment*, 68:17–23, 2013.
- [233] Jingjing Pei, Yihui Yin, Jianping Cao, Yahong Sun, Junjie Liu, and Yiping Zhang. Time dependence of characteristic parameter for semi-volatile organic compounds (SVOCs) emitted from indoor materials. *Building and Environment*, 125:339–347, 2017.
- [234] Alodie Blondel and Hervé Plaisance. Screening of formaldehyde indoor sources and quantification of their emission using a passive sampler. *Building and Environment*, 46(6):1284–1291, 2011.
- [235] Charles J. Weschler. Ozone in indoor environments: Concentration and chemistry. *Indoor Air*, 10(4):269–288, 12 2000.
- [236] Archit Manuja, Jenna Ritchie, Khantil Buch, Yaoxing Wu, Clara M.A. Eichler, John C. Little, and Linsey C. Marr. Total surface area in indoor environments. *Environmental Science: Processes and Impacts*, 21(8):1384–1392, 8 2019.
- [237] Victor W. Or, Michael Wade, Sameer Patel, Michael R. Alves, Deborah Kim, Sarah Schwab, Hannah Przelomski, Rachel O’Brien, Donghyun Rim, Richard L. Corsi, Marina E. Vance, Delphine K. Farmer, and Vicki H. Grassian. Glass surface evolution following gas adsorption and particle deposition from indoor cooking events as probed by microspectroscopic analysis. *Environmental Science: Processes and Impacts*, 22(8):1698–1709, 2020.
- [238] E. Uhde and T. Salthammer. Impact of reaction products from building materials and furnishings on indoor air quality-A review of recent advances in indoor chemistry. *Atmospheric Environment*, 41(15):3111–3128, 2007.
- [239] David B. Asay and Seong H. Kim. Evolution of the adsorbed water layer structure on silicon oxide at room temperature. *Journal of Physical Chemistry B*, 109(35):16760–16763, 2005.
- [240] Yanwei Li, Antonios Tasoglou, Aikaterini Liangou, Kerrigan P. Cain, Leif Jahn, Peishi Gu, Evangelia Kostenidou, and Spyros N. Pandis. Cloud condensation nuclei activity and hygroscopicity of fresh and aged cooking organic aerosol. *Atmospheric Environment*, 176:103–109, 3 2018.
- [241] Bryan E. Cummings, Ying Li, Peter F. Decarlo, Manabu Shiraiwa, and Michael S. Waring. Indoor aerosol water content and phase state in U.S. residences: Impacts of relative humidity, aerosol mass and composition, and mechanical system operation. *Environmental Science: Processes and Impacts*, 22(10):2031–2057, 10 2020.

- [242] Victor W. Or, Michael Wade, Sameer Patel, Michael R. Alves, Deborah Kim, Sarah Schwab, Hannah Przelomski, Rachel O'Brien, Donghyun Rim, Richard L. Corsi, Marina Eller Vance, Delphine K. Farmer, and Vicki H. Grassian. Glass surface evolution following gas adsorption and particle deposition from indoor cooking events as probed by microspectroscopic analysis. *Environmental Science: Processes & Impacts*, 22(8):1698–1709, 2020.
- [243] Jason W.L. Lee, Vanesa Carrascón, Peter J. Gallimore, Stephen J. Fuller, Alex Björkegren, David R. Spring, Francis D. Pope, and Markus Kalberer. The effect of humidity on the ozonolysis of unsaturated compounds in aerosol particles. *Physical Chemistry Chemical Physics*, 14(22):8023–8031, 6 2012.
- [244] O. Vesna, M. Sax, M. Kalberer, A. Gaschen, and M. Ammann. Product study of oleic acid ozonolysis as function of humidity. *Atmospheric Environment*, 43(24):3662–3669, 8 2009.
- [245] Hui-Ming Hung, Yasmine Katrib, and Scot T Martin. Products and Mechanisms of the Reaction of Oleic Acid with Ozone and Nitrate Radical. 2005.
- [246] J Zahardis and G A Petrucci. The oleic acid-ozone heterogeneous reaction system: products, kinetics, secondary chemistry, and atmospheric implications of a model system-a review. *Atmos. Chem. Phys*, 7:1237–1274, 2007.
- [247] Man Luo, Nicholas A. Wauer, Kyle J. Angle, Abigail C. Dommer, Meishi Song, Christopher M. Nowak, Rommie E. Amaro, and Vicki H. Grassian. Insights into the behavior of nonanoic acid and its conjugate base at the air/water interface through a combined experimental and theoretical approach. *Chemical Science*, 11(39):10647–10656, 10 2020.
- [248] Rachel E. O'Brien, Ying Li, Kristian J. Kiland, Erin F. Katz, Victor W. Or, Emily Legaard, Emma Q. Walhout, Corey Thrasher, Vicki H. Grassian, Peter F. Decarlo, Allan K. Bertram, and Manabu Shiraiwa. Emerging investigator series: Chemical and physical properties of organic mixtures on indoor surfaces during HOMEChem. *Environmental Science: Processes and Impacts*, 23(4):559–568, 4 2021.